Thermoelectric effects in quantum systems

Thermoelectric effects in quantum systems

Dissertation

for the purpose of obtaining the degree of doctor
at Delft University of Technology
by the authority of the Rector Magnificus,
Prof.Dr.Ir T.H.J.J. van der Hagen,
chair of the Board for Doctorates
to be defended publicly on
Friday 28 February 2025 at 12:30 o'clock

by

Serhii VOLOSHENIUK

This dissertation has been approved by the promotors.

Composition of the doctoral committee:

Rector Magnificus,	chairperson
Prof. Dr. Ir. H. S. J. van der Zant,	Delft University of Technology, *promotor*
Prof. Dr. P. Gehring,	Universite Catholique de Louvain, *promotor*

Independent members:

Dr. M. Blaauboer	Delft University of Technology
Prof. Dr. Y. M. Blanter	Delft University of Technology
Dr. B. Gotsmann	IBM Research Europe-Zurich, Switzerland
Dr. E. Greplova	Delft University of Technology
Dr. C. B. Winkelmann	Universite Grenoble Alpes, France

Reserve members:

Prof. Dr. Y. V. Nazarov	Delft University of Technology

Keywords: Molecular electronics, quantum transport, thermoelectric effects, thermopower, energy conversion, particle-exchange heat engine, Yu-Shiba-Rusinov bound states, double lock-in method, 2D magnetism, CrSBr, entropy

Printed by: Gildeprint, Enschede

Cover art by: Alessandra Canetta

ISBN 978-94-6384-733-9

An electronic copy of this dissertation is available at
https://repository.tudelft.nl/.
The associated experimental data for this dissertation are available at
https://data.4tu.nl/datasets/cdb42d77-6e0b-4132-8f26-2b560673b745.

In honor of Oleksandr Goshylyk (109, "Cursed Molfar"), a true friend and a true son of his country.

CONTENTS

SUMMARY

This thesis focuses on thermoelectric properties of nano-scale devices based on quantum effects. These properties involve interesting fundamental physical phenomena and can also be used for practical applications, e.g., in optimising the heat waste problem in electronics.

- **Chapter 1** provides a general introduction to the topic and an outline of the thesis.
- **Chapter 2** contains a concise description of the theoretical concepts relevant to the study.
- **Chapter 3** describes the implementation of superconductor-normal metal-superconductor thermometry in electromigrated break junction architecture. In this chapter, we show how to create a thermopower device and how to perform thermometry measurements correctly.
- **Chapter 4** is dedicated to the detailed description of the double lock-in method that allows to simultaneously measure differential conductance and thermocurrent. We focus on the different aspects behind the technique including performing the experiments, processing the data and interpreting the results.
- **Chapter 5** describes the experimental investigation of the thermopower response of a di-radical all-organic molecule in a proximity-induced superconducting junction. We demonstrate how the system can be switched from the Kondo state to the Yu-SHiba-Rusinov regime, which is accompanied by a five-fold increase in the power factor.
- **Chapter 6** contains the description of the first single-molecule particle exchange heat engine and the process of fine-tuning it to find the optimal load value for maximum power output.
- **Chapter 7** describes the thermocurrent response of a CrSBr flake upon changes in the magnetic field and temperature. We demonstrate that spin-entropy plays a role and that the Seebeck coefficient is enhanced close to the phase transition point. We also show that at low temperatures the power factor of the device can be changed by 600% upon applying a magnetic field.

- **Chapter 8** concludes this thesis with a discussion of the results presented in the previous chapters, ideas on potential future follow-up experiments and on practical implications of the findings presented.

SAMENVATTING

Dit proefschrift richt zich op thermo-elektrische effecten van apparaten op de nanoschaal die gebaseerd zijn op kwantumeffecten. Deze eigenschappen omvatten interessante fundamentele fysische fenomenen en kunnen ook gebruikt worden voor praktische toepassingen, zoals bijvoorbeeld het optimaliseren het warmteverspillingsprobleem in elektronica.

- **Hoofdstuk 1** geeft een algemene inleiding over het onderwerp en een overzicht van het proefschrift.
- **Hoofdstuk 2** bevat een beknopte omschrijving van de theoretische concepten die relevant zijn voor dit werk.
- **Hoofdstuk 3** beschrijft de implementatie van supergeleider-normaal metaal-supergeleider thermometrie in een geëlektromigreerde breekjunctie architectuur. In dit hoofdstuk laten we zien hoe een thermovermogen apparaat gemaakt wordt en hoe thermometrie metingen juist worden uitgevoerd.
- **Hoofdstuk 4** is gewijd aan de gedetailleerde beschrijving van de dubbele lock-in methode die het toelaat om tegelijkertijd de differentiële geleiding en de thermostroom te meten. We richten ons op de verschillende aspecten achter de techniek, waaronder het uitvoeren van de experimenten, het verwerken van de data en het interpreteren van de resultaten.
- **Hoofdstuk 5** beschrijft het experimentele onderzoek naar de thermovermogensrespons van een diradicaal, organisch molecuul in een nabijheid-geïnduceerde supergeleidende junctie. We laten zien hoe het systeem geschakeld kan worden van een Kondo toestand naar het Yu-Shiba-Rusinov regime, die gepaard gaat met een vijfvoudige toename van de vermogensfactor.
- **Hoofdstuk 6** bevat de beschrijving van de allereerste enkel-moleculaire warmtewisselingsmotor en het proces van het afstellen daarvan om zo de optimale belastingwaarde voor maximaal vermogen te vinden.
- **Hoofdstuk 7** beschrijft de thermostroom respons van een CrSBr vlok bij veranderingen in het magneetveld en de temperatuur. We demonstreren dat spin-entropie een rol speelt en dat de Seebeck

coëfficient versterkt wordt dicht bij het faseovergangspunt. We laten ook zien dat bij lage temperaturen de vermogensfactor van het apparaat veranderd kan worden met 600% door het aanleggen van een magnetisch veld.

- **Hoofdstuk 8** concludeert dit proefschrift met een discussie van alle gepresenteerde resultaten, ideeën voor mogelijke vervolgexperimenten en de praktische implicaties van de gepresenteerde bevindingen.

1

INTRODUCTION

"*I am among those who think that science has great beauty.*"

Marie Curie

1

An endless pursuit of progress creates an impressive synergy between modern physics and technology. Both compete, challenge and push each other forward. Breakthroughs in physics serve as a base for technological revolutions, while new concepts of technology open fresh avenues for physical research and development. By formulating the theory of electromagnetism [1] in the second part of the XIX century, Maxwell stimulated the work [2] of Hertz, who experimentally confirmed the existence of electromagnetic waves. This immediately rose a question about possible applications, and Guglielmo Macroni's patent swiftly appeared [3]. Strikingly, further development of the radio technology stimulated the emergence of new fields in astrophysics, and these days humankind have the ability to touch the deepest questions of Universe, collect the microwave background radiation and evaluate the Big Bang Theory [4]. There are a lot of similar stories: the laser invention enabled a wide variety of experiments in quantum mechanics; the development of X-ray technology has driven advancements in both medical imaging and crystallography, etc. They can be more or less interesting depending on one's preferences and background. Some connections are non-trivial to grasp, especially if you are not an expert in the field. For example, the Global Position System (GPS) that we commonly use for cycling in Delft relies [5] on Einstein's theory of relativity. And some of these stories captured the interest of the author and pushed him to do a PhD and write this thesis.

One of the more fascinating examples of unison between physics and technology started with the invention of the transistor [6] by John Bardeen, Walter Brattain, and William Shockley. This event marked the beginning of modern computer technology and dramatically stimulated physics to create smaller, faster, more reliable, and more energy-efficient computer components. The scientific community tried various platforms and approaches to boost the computational power and make computers smaller. That lead to the formulation of Moore's Law [7], which predicts the exponential growth in the number of transistors on a microchip, and states that the amount of transistors in the circuit doubles each few years. Indeed, this prediction was accurate so far, and, as a result, in less then one century technology went from the thermionic triode, the vacuum tube with tremendous size, to micro metal-oxide-semiconductor (MOS) transistors, which everyone has in their personal computers today. However, from the beginning it was clear that technology would reach the limit of single atom or a group of atoms. So even in the beginning, there were proposals [8] to use single molecules as building blocks for computers. This gave a rise to the field of molecular electronics and initiated fundamental studies of single molecules. Modern development of semiconducting industry with components of already below [9] 5 nm questions the ability of molecules for being the main ingredient in electronics, but does not erase the

possibility.

1.1. MOLECULAR ELECTRONICS

As mentioned before, the idea of utilizing a single molecule as an electronic component is an old one. It was first formalized by von Hippel [8] in 1956 and existed for some time without substantial response from the scientific community. The situation changed with the proposal by Aviram and Ratner [10] in 1974. They presented the concept of a rectifier based on a single molecule, consisting of donor and acceptor systems separated by a tunneling bridge. This work stimulated multiple research studies, primarily focusing on developing techniques for applying contacts to single molecules and possible applications. Different logic gates were proposed [11] and the different groups worked on their realization.

The history of molecular electronics is fascinating, but we will not address it here. For a detailed overview of the history of molecular electronics, we recommend checking the review by Ratner et al. [12] or an extended study by Vhoi *et al.* [13]. The next significant milestone occurred in the 1990-s, when scientists finally managed to contact molecules with different platforms. At that time, multiple studies appeared, both offering practical applications and deepening the fundamental understanding of the physics of nano-scale objects. It was experimentally shown that molecules can act as diodes [14]; many studies (see [15] for a comprehensive review) demonstrated high rectification ratios both in single molecules and molecular mono-layers. Also, molecular junctions were shown to exhibit memory effects which allowed them to be used for information storage and processing [16–18]. An interesting realization of logic operation in molecular devices was shown with the realization of a Single Electron Logic Calculator [19]. Molecules also were shown to be utilized for mechanical sensors [20]. Another interesting aspect of molecules is that they could be harvested for thermoelectric purposes [21, 22]. We will discuss it in more detail in Sec.1.3 as this topic forms the foundation of this thesis.

1.2. WAYS TO PROBE THE MOLECULE

The reasonable question that could be asked is how all these charge transport measurements on single molecules can be performed. It is not trivial to contact and measure an object which is of only a few nm in size. The answer is hidden behind the enormous efforts of physicists and engineers. At the moment, there are three widely used architectures [23–25] that allow to fulfil this task, each with its own advantages and disadvantages. The choice of the framework is dictated by the specifics of the research inquiry that is raised

during molecular investigation. Also, a framework [26] that utilizes micro-electromechanical system (MEMS) technology [27] already exists and has the potential to become the mainstream one, though it still needs further development. We discuss it further in the "Concluding remarks" chapter 8 of this thesis.

One of the ways to measure the charge transport characteristics through a molecule is using a scanning tunneling microscope (STM). The idea behind it is to employ the atomically sharp tip of the STM to probe the tunneling current from the conducting surface to the tip through molecule. The main advantage of this method is the ability to move the tip in space and probe the molecule at different positions. Also, the operator has a direct vision of what is being measured, and the image of the molecule can be captured during the transport measurements. However, it has some drawbacks. First, typically there is a high asymmetry between molecular coupling to the tip and substrate (this coupling is usually large, leading to poor energy resolution). Second, with this method it is not possible to apply a gate voltage in order to tune the energetic levels of the molecule independently from the chemical potential of the leads. With the addition of an extra insulating layer between the conducting substrate and molecule (see e.g. [28–30]) the coupling to the substrate can be made weaker so that the energy resolution improves. Furthermore, some approaches to tackle the second issue have been proposed [31, 32], however they are not commonly used in literature. Importantly, the STM method is not scalable, so it is mainly suitable for research purposes. Yet, it is useful for this as after the first measurements on a C_{60} molecule [23] a lot of interesting research was performed with this technique [33]: molecule-substrate interactions [34], molecular vibrations [35–37], investigation of Yu Shiba Rusinov (YSR) states [38], thermopower measurements on molecules [39] and many other topics. The molecule that we use in Chapter 6 was measured with the STM technique [40] and as we will demonstrate later the data in [40] is in good agreement with the content of this thesis.

Another widely used and powerful platform is the mechanically controlled break junction (MCBJ) [24]. In this method, a weak link, typically a thin gold wire, is gradually broken by mechanical strain applied through a piezoelectric element or motor, creating two contacts to the molecule. Usually, the current is constantly monitored under constant bias as the gold is first stretched to the single atom contact with conductance, $G = 7.75 * 10^{-5}$ S, and then further displaced ("breaking trace") until the measured signal reaches the noise level. Subsequently, the applied strain is gradually removed, and the weak link can restore its initial state ("making trace"). The process can be repeated many times and in some of the traces there molecules are trapped between the contacts. This method allows to collect large amounts of data and

provides basic transport information about the molecule both at room temperature [41] and at low temperatures [42, 43]. It serves not only as a good platform to investigate how the anchoring groups influence [44, 45] transport through the molecules, but also to reveal various physical phenomena such as large negative differential conductance [46], Kondo physics [47], interference phenomena [48, 49], etc. The main advantages of this method are the high mechanical stability, the high control of the gap size to sub-angstrom precision, and the ability to collect large amounts of data for statistical purposes. At the same time, it does not provide information about the exact configuration of the molecule inside the junction and, only a limited number of studies have successfully implemented a gate in this setting [50–52].

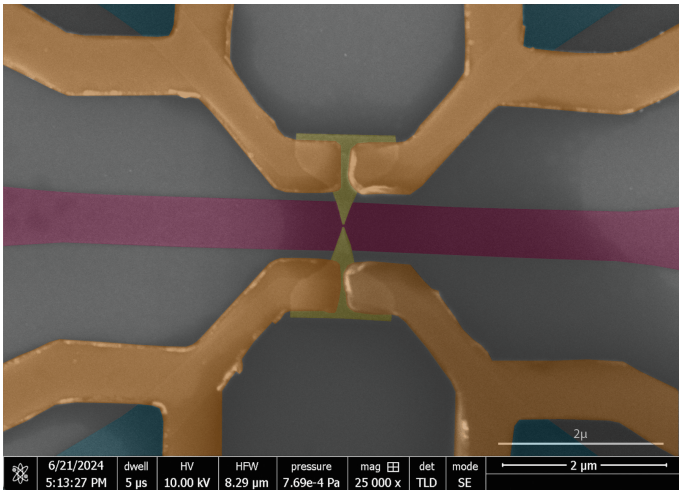

Figure 1.1: False colored scanning electron microscopy picture of a typical thermopower device used to perform thermoelectric measurements on single molecules. Parts of the devices are highlighted with color: blue (heater), purple (gate), yellow (golden bridge), orange (suerconducting contacts).

Finally, there is another architecture that we use in this thesis. This technique is known as the electromigrated break junction (EMBJ) [25], illustrated in figure 1.1. We will discuss it in detail later on, and here we focus only on the weak link (shown in yellow in figure 1.1), further referred to as the golden bridge, and a local gate (shown in purple in figure 1.1). By applying a voltage across the golden bridge, it is possible to generate a current density high enough to push atoms of gold from their positions to form a nanometer-sized gap. The process can be implemented in a controllable way [53] to avoid formation of gold quantum dots. In this dissertation, we migrate

devices up to 4-6 kΩ and leave them for self-migration [54]. This allows us to obtain gaps of less than 2 nm, capable of trapping a single molecule. The local gate allows precise tuning of molecular energy levels, enabling charge/discharge control of the molecule and switching between resonance and off-resonance transport. This is the key advantage of this technique compared to STM or MCBJ. However, this method also has disadvantages. First of all, it requires more lithographic steps and has a low yield. Also, using this method, the molecule is studied in one particular configuration, which can be difficult to reproduce. In our studies, the typical yield to obtain molecular EMBJ devices is 20% and the amount of bonded devices per chip was limited to two due to the additional contacts required for thermoelectric measurements, shown in blue on figure 1.1. These extra contacts act as local heaters and allow to perform thermoelectric measurements on single molecules.

1.3. THERMOELECTRICITY IN MOLECULAR DEVICES

The integration of heaters into the EMBJ platform unlocks a huge area of research opportunities in the field of molecular thermoelectricity. While it is primarily stimulated by waste heat harvesting applications, it also provides a unique opportunity to probe fundamental questions related to heat and energy flow in nanoscale devices and presents a good platform to check classical theories, such as the Wiedemann Frantz Law, at the nano scale. Additionally, the thermopower signal can be a tool to provide information which is challenging to obtain with conventional transport measurements [55, 56], in a non-invasive manner. Yet key milestones [57] remain unmet, keeping this area both timely and active. This thesis makes a contribution to the ongoing work. Below is a short introduction to the topic.

Thermoelectricity research originates from the research conducted in the end of the XVIII century and the beginning of the XIX century with the pioneering works [58, 59] of Aepinus, Volta, Galvani, Seebeck (for historical inspiration refer to [60]). These early researchers focused their attention on the interplay between heat and charge flow, laying the foundation for several key thermoelectric effects. Among these, the most well known are the Seebeck effect [59], Peltier effect [61], Thomson effect [62] and the Nernst effect [63]. The Seebeck effect is of particular interest for this thesis. It refers to the build-up of a thermovoltage due to a temperature gradient across the material. The potential to use it for power generation was recognised right after the effect was described and has been a focal point in the development of thermoelectric technologies ever since. Scientists consistently explored various materials to achieve higher Seebeck coefficients. Over time, it was discovered that optimizing heat-to-energy conversion efficiency

requires more than just a high Seebeck coefficient, as electrical and thermal conductance are also crucial for it. During investigation of different semiconductors, Ioffe introduced [64] the ZT figure of merit, $ZT = \frac{S^2 G_e T}{G_{th}}$, where S is a Seebeck coefficient, G_e, and G_{th} are electrical and thermal conductance, respectively. This ZT coefficient is directly connected to the energy conversion efficiency of the device harvesting heat into useful power, with efficiency reaching the Carnot limit as $ZT \to \infty$. This discovery provided the scientific community with a direction to search for materials with high Seebeck coefficient, high electric conductance and low G_{th}. Unfortunately, these values are interconnected and, typically, an increase in S leads to a decrease in G_e, and vice versa. Among different materials, semiconductors are the most prominent candidates, but their ZT values typically range [65] from 1 to 3, with the current record [66] of 5.4 for n-type pristine few-layer black phosphorus. To substantially enhance energy conversion efficiency, achieving ZT values of an order of magnitude higher is required, but this seems unattainable with existing semiconductor technology.

Meanwhile, molecular devices introduce an alternative platform that has a potential to reach high ZT values [67, 68] paving the way for better waste heat control. The high charging energy of molecules allows to treat them as a single-level system [69] in first approximation. The level plays a role of energy filter that is typically narrow compared to the thermal energy $k_B T$ (where k_B is the Boltzmann constant and T is temperature), which helps to minimise entropy generation during particle transfer [70], desirable for high efficiency. At the same time, it is possible to manipulate/construct the energy levels in a way that boosts their Seebeck coefficient [71] and suppresses the phonon contribution to the thermal conductance [72]. A lot of theoretical [73–75] and experimental work [76–78] has been performed on this topic, mainly utilizing quantum interference of electron waves travelling through the molecule. However, despite impressive theoretical predictions, results are still not satisfying. Current ZT values [76] for C_{60} are still not high enough to outperform semiconductors. The development of a molecular device with high heat-to-energy conversion efficiency is still an ongoing effort. Achieving this breakthrough would unlock a wide range of applications, including charging of wearable electronics, enhanced thermal management systems within microchips, and beyond.

Additionally, thermoelectric studies of molecular devices not only have potential for practical applications, but also serve as a non-invasive source of extra information about the system under the investigation. For example, by measuring the thermovoltage it is possible to determine the location of the Fermi level [79] with respect to the highest occupied and lowest unoccupied molecular orbitals. The change of the thermocurrent sign is a benchmark [55] for the extraction of the Kondo temperature, the position of which is difficult to determine from transport

measurements. Also, thermocurrent can reveal information [56] about the transitions between different states in the molecule. We will discuss this in more detail and demonstrate the thermopower measurement effectiveness using our experimental data in Chapter 4.

1.4. THESIS OUTLINE

This dissertation is dedicated to the investigation of thermoelectric properties of nano-scale devices, and in particular molecular devices, and to the exploration of their potential applications. We first start with the preparation for the measurements. This includes developing the necessary sub-kelvin thermometry to accurately determine the temperature difference across the device, enabling precise estimation of physical values. Additionally, we ensure that the method used for the measurements is reliable and correctly configured. After achieving this, we investigate two molecules: a diradical nitronyl nitroxide compound (NNDR) and an all-organic diradical molecule (Sme-2Os), inside EMBJ devices with local heaters. The first molecule was cooled to 100 mK. The interaction between the spin of the molecule and the Cooper pairs on the proximity-induced superconducting leads gave rise to Yu-Shiba-Rusinov bound states. These bound states and their thermopower response can be employed as energy filters that boost the thermal efficiency of the device. The second molecule was investigated at 1.7 K. We first investigated its magnetic fingerprints (Kondo effect and inelastic spin flip excitation) and then used it for thermal energy utilization. By connecting a load resistor to it in series and applying a temperature gradient across the junction, we realised the first molecular heat engine. Then, we investigated the maximum power output and engineering efficiency of the system as a function of the load resistance and extracted its optimal value. Finally, we conclude the thesis with the exploration of the thermoelectric response of a 2D magnet. This experiment is an outlier of the molecular story, however, it uses the method developed during the preparation stage and provides an alternative platform for heat-to-energy harvesting purposes. In this study, we show that spin entropy plays a significant role in heat-to-charge conversion and found that there is a significant enhancement of thermoelectric power factor around Néel point.

Each chapter after the first two entitled "Introduction" and Theory" is self-contained and can be read independently. All the necessary information can be found in supplementary information and references. Still, these narratives are coherent and can be combined into one "Thermoelectric effects in quantum systems" story with the outline described below.

In **Chapter 2** we give the theoretical background providing the reader with the main concepts of the features detected in molecular

measurements in three-terminal devices at low temperatures. We quickly go through Coulomb blockade theory, Kondo physics, elastic/inelastic cotunneling, spin-spin interactions, while avoiding complicated calculations. Then, we briefly describe the Onsager theory and physical quantities related to thermopower, concluding the chapter with a discussion of the heat engine theory. Also, a small part of the chapter is devoted to superconductivity and the theory of Josephson junctions, as well as to the effects that can be observed in this context, in particular, Yu-Shiba-Rusinov bound states.

Next, in **Chapter 3** we implement the superconductor-normal metal-superconductor thermometry in the EMBJ architecture. The chapter contains information on how to fabricate a thermopower device and how to extract the temperature difference across the molecular junction during the experiment.

Chapter 4 describes another necessary component to perform successful thermoelectric experiments. Here, we focus on the double lock-in method used to measure differential conductance and thermocurrent simultaneously. We discuss the details for setting up the measurement, explain how the raw data should be postprocessed to arrive to the physical values, and provide information on the different regimes for which the method should and should not be applied, as well as hints on data interpretation. This chapter should be seen as a guide for thermoelectric measurements.

In **Chapter 5**, we investigate the thermopower response of a diradical, all-organic molecule in a proximity-induced superconducting junction. We tune the system from the Kondo state to the YSR regime and demonstrate a five-fold increase in the power factor.

The first application of the molecular device as a particle exchange heat engine is described in **Chapter 6**. We first demonstrate thermopower results that reveal magnetic fingerprints of the diradical molecule. Then, we realise a molecular heat engine and experimentally find the load value for which the engine produces the maximum power output.

Further on, in **Chapter 7** we investigate how differential conductance and thermocurrent through a CrSBr flake change once we sweep the magnetic field and temperature, i.e., change the magnetic order. Our study reveals how different types of entropy are effecting the Seebeck coefficient, and we particularly highlight the role of spin entropy.

Finally, we finish this thesis with the "Concluding remarks" in **Chapter 8**, where we discuss the possible follow-up research studies.

REFERENCES

[1] J. C. Maxwell. “Relativity in the Global Positioning System”. *Phil. Trans. R. Soc. Lond.* 155 (Jan. 1865).

[2] H. Hertz. “On the Finite Velocity of Propagation of Electromagnetic Actions”. *Wiedemanns Annalen* 34 (1888), pp. 551–569.

[3] G. Marconi. “Improvements in transmitting electrical impulses and signals, and in apparatus therefor”. Patent 12039. 1896.

[4] J.-P. Uzan. “The Big-Bang Theory: Construction, Evolution and Status”. *The Universe: Poincaré Seminar 2015*. Springer International Publishing, 2021.

[5] N. Ashby. “Relativity in the Global Positioning System”. *Living Rev. Relativ.* 6.1 (Jan. 2003).

[6] M. Riordan, L. Hoddeson, and C. Herring. “The invention of the transistor”. *Rev. Mod. Phys.* 71 (2 Mar. 1999), S336–S345.

[7] G. E. Moore. “Cramming more components onto integrated circuits, Reprinted from Electronics, volume 38, number 8, April 19, 1965, pp.114 ff.” *IEEE Solid-State Circuits Society Newsletter* 11.3 (2006), pp. 33–35.

[8] A. von Hippel. “Molecular Engineering”. *Science* 123.3191 (1956), pp. 315–317.

[9] S.-Y. Wu, C. Chang, M. Chiang, C. Lin, J. Liaw, J. Cheng, J. Yeh, H. Chen, S. Chang, K. Lai, M. Liang, K. Pan, J. Chen, V. Chang, T. Luo, X. Wang, Y. Mor, C. Lin, S. Wang, M. Hsieh, C. Chen, B. Wu, C. Lin, C. Liang, C. Tsao, C. Li, C. Chen, C. Hsieh, H. Liu, P. Chen, C. Chen, R. Chen, Y. Yeo, C. Chui, W. Chang, T. Lee, K. Huang, H. Lin, K. Chen, M. Tsai, K. Chen, X. Chen, Y. Cheng, C. Wang, W. Shue, Y. Ku, S. M. Jang, M. Cao, L. Lu, and T. Chang. “A 3nm CMOS FinFlex Platform Technology with Enhanced Power Efficiency and Performance for Mobile SoC and High Performance Computing Applications”. *2022 International Electron Devices Meeting (IEDM)*. 2022, pp. 27.5.1–27.5.4.

[10] A. Aviram and M. A. Ratner. “Molecular rectifiers”. *Chemical Physics Letters* 29.2 (1974), pp. 277–283. issn: 0009-2614.

[11] A. Aviram. “Molecules for memory, logic, and amplification”. *Journal of the American Chemical Society* 110.17 (Aug. 1988), pp. 5687–5692.

[12] M. Ratner. “A brief history of molecular electronics”. *Nature Nanotechnology* 8.6 (June 2013), pp. 378–381.

[13] H. Choi and C. C. Mody. “The Long History of Molecular Electronics: Microelectronics Origins of Nanotechnology”. *Social Studies of Science* 39.1 (2009), pp. 11–50.

[14] M. Elbing, R. Ochs, M. Koentopp, M. Fischer, C. von Hänisch, F. Weigend, F. Evers, H. B. Weber, and M. Mayor. “A single-molecule diode”. *Proceedings of the National Academy of Sciences* 102.25 (2005), pp. 8815–8820.

[15] R. Gupta, J. A. Fereiro, A. Bayat, A. Pritam, M. Zharnikov, and P. C. Mondal. “Nanoscale molecular rectifiers”. *Nature Reviews Chemistry* 7.2 (Feb. 2023), pp. 106–122.

[16] L. Bogani and W. Wernsdorfer. “Molecular spintronics using single-molecule magnets”. *Nature Materials* 7.3 (Mar. 2008), pp. 179–186.

[17] Y. Han, C. Nickle, Z. Zhang, H. P. A. G. Astier, T. J. Duffin, D. Qi, Z. Wang, E. del Barco, D. Thompson, and C. A. Nijhuis. “Electric-field-driven dual-functional molecular switches in tunnel junctions”. *Nature Materials* 19.8 (Aug. 2020), pp. 843–848.

[18] M. Irie, T. Fukaminato, T. Sasaki, N. Tamai, and T. Kawai. “A digital fluorescent molecular photoswitch”. *Nature* 420.6917 (Dec. 2002), pp. 759–760.

[19] R. Liu, Y. Han, F. Sun, G. Khatri, J. Kwon, C. Nickle, L. Wang, C.-K. Wang, D. Thompson, Z.-L. Li, C. A. Nijhuis, and E. del Barco. “Stable Universal 1- and 2-Input Single-Molecule Logic Gates”. *Advanced Materials* 34.26 (2022), p. 2202135.

[20] M. Urdampilleta, C. Ayela, P.-H. Ducrot, D. Rosario-Amorin, A. Mondal, M. Rouzières, P. Dechambenoit, C. Mathonière, F. Mathieu, I. Dufour, and R. Clérac. “Molecule-based microelectromechanical sensors”. *Scientific Reports* 8.1 (May 2018), p. 8016.

[21] M. Naher, D. C. Milan, O. A. Al-Owaedi, I. J. Planje, S. Bock, J. Hurtado-Gallego, P. Bastante, Z. M. Abd Dawood, L. Rincón-García, G. Rubio-Bollinger, S. J. Higgins, N. Agraït, C. J. Lambert, R. J. Nichols, and P. J. Low. “Molecular Structure–(Thermo)electric Property Relationships in Single-Molecule Junctions and Comparisons with Single- and Multiple-Parameter Models”. *Journal of the American Chemical Society* 143.10 (Mar. 2021), pp. 3817–3829.

[22] P. Gehring, J. K. Sowa, C. Hsu, J. de Bruijckere, M. van der Star, J. J. Le Roy, L. Bogani, E. M. Gauger, and H. S. J. van der Zant. “Complete mapping of the thermoelectric properties of a single molecule”. *Nature Nanotechnology* 16.4 (Apr. 2021), pp. 426–430.

[23] C. Joachim, J. K. Gimzewski, R. R. Schlittler, and C. Chavy. “Electronic Transparence of a Single C_{60} Molecule”. *Phys. Rev. Lett.* 74 (11 Mar. 1995), pp. 2102–2105.

[24] M. A. Reed, C. Zhou, C. J. Muller, T. P. Burgin, and J. M. Tour. “Conductance of a Molecular Junction”. *Science* 278.5336 (1997), pp. 252–254.

[25] H. Park, A. K. L. Lim, A. P. Alivisatos, J. Park, and P. L. McEuen. “Fabrication of metallic electrodes with nanometer separation by electromigration”. *Applied Physics Letters* 75.2 (July 1999), pp. 301–303.

[26] H. Jeong, H. B. Li, L. Domulevicz, and J. Hihath. “An On-Chip Break Junction System for Combined Single-Molecule Conductance and Raman Spectroscopies”. *Advanced Functional Materials* 30.28 (2020), p. 2000615.

[27] M. K. Mishra, V. Dubey, P. M. Mishra, and I. Khan. “MEMS Technology: A Review”. *Journal of Engineering Research and Reports* (2019).

[28] J. Repp, G. Meyer, S. M. Stojković, A. Gourdon, and C. Joachim. “Molecules on Insulating Films: Scanning-Tunneling Microscopy Imaging of Individual Molecular Orbitals”. *Phys. Rev. Lett.* 94 (2 Jan. 2005), p. 026803.

[29] K. Kaiser, L.-A. Lieske, J. Repp, and L. Gross. “Charge-state lifetimes of single molecules on few monolayers of NaCl”. *Nature Communications* 14.1 (Aug. 2023).

[30] R. Hoffmann-Vogel. “Imaging prototypical aromatic molecules on insulating surfaces: a review”. *Reports on Progress in Physics* 81.1 (Dec. 2017), p. 016501.

[31] E. S. Soldatov, V. V. Khanin, A. S. Trifonov, S. P. Gubin, V. V. Kolesov, D. E. Presnov, S. A. Iakovenko, G. B. Khomutov, and A. N. Korotkov. “Room temperature molecular single-electron transistor”. *Physics-Uspekhi* 41.2 (Feb. 1998), p. 202.

[32] Y. Li, M. Buerkle, G. Li, A. Rostamian, H. Wang, Z. Wang, D. R. Bowler, T. Miyazaki, L. Xiang, Y. Asai, G. Zhou, and N. Tao. “Gate controlling of quantum interference and direct observation of anti-resonances in single molecule charge transport”. *Nature Materials* 18.4 (Apr. 2019), pp. 357–363.

[33] I. F. Torrente, K. J. Franke, and J. I. Pascual. “Spectroscopy of C60 single molecules: the role of screening on energy level alignment”. *Journal of Physics: Condensed Matter* 20.18 (Apr. 2008), p. 184001.

[34] M. Schunack, L. Petersen, A. Kühnle, E. Lægsgaard, I. Stensgaard, I. Johannsen, and F. Besenbacher. “Anchoring of Organic Molecules to a Metal Surface: HtBDC on Cu(110)”. *Phys. Rev. Lett.* 86 (3 Jan. 2001), pp. 456–459.

[35] B. C. Stipe, M. A. Rezaei, and W. Ho. “Single-Molecule Vibrational Spectroscopy and Microscopy”. *Science* 280.5370 (1998), pp. 1732–1735.

[36] X. H. Qiu, G. V. Nazin, and W. Ho. “Vibronic States in Single Molecule Electron Transport”. *Phys. Rev. Lett.* 92 (20 May 2004), p. 206102.

[37] L. J. Lauhon and W. Ho. “Single-molecule vibrational spectroscopy and microscopy: CO on Cu(001) and Cu(110)”. *Phys. Rev. B* 60 (12 Sept. 1999), R8525–R8528.

[38] K. J. Franke, G. Schulze, and J. I. Pascual. “Competition of Superconducting Phenomena and Kondo Screening at the Nanoscale”. *Science* 332.6032 (2011), pp. 940–944.

[39] C. Evangeli, K. Gillemot, E. Leary, M. T. González, G. Rubio-Bollinger, C. J. Lambert, and N. Agraït. “Engineering the Thermopower of C60 Molecular Junctions”. *Nano Letters* 13.5 (May 2013), pp. 2141–2145.

[40] A. Vegliante, S. Fernandez, R. Ortiz, M. Vilas-Varela, T. Baum, N. Friedrich, F. Romero-Lara, A. Aguirre, K. Vaxevani, D. Wang, C. Garcia, H. S. J. van der Zant, T. Frederiksen, D. Peña, and J. I. Pascual. “Tuning the Spin Interaction in Non-planar Organic Diradicals Through Mechanical Manipulation”. *arXiv* (2024). arXiv: 2402.08641.

[41] R. Frisenda, M. L. Perrin, H. Valkenier, J. C. Hummelen, and H. S. J. van der Zant. “Statistical analysis of single-molecule breaking traces”. *Physica status solidi (b)* 250.11 (2013), pp. 2431–2436.

[42] R. Frisenda, M. L. Perrin, and H. S. J. van der Zant. “Probing the local environment of a single OPE3 molecule using inelastic tunneling electron spectroscopy”. *Beilstein Journal of Nanotechnology* 6 (2015), pp. 2477–2484.

[43] C. A. Martin, R. H. M. Smit, R. v. Egmond, H. S. J. van der Zant, and J. M. van Ruitenbeek. “A versatile low-temperature setup for the electrical characterization of single-molecule junctions”. *Review of Scientific Instruments* 82.5 (May 2011), p. 053907.

[44] L. A. Zotti, T. Kirchner, J.-C. Cuevas, F. Pauly, T. Huhn, E. Scheer, and A. Erbe. “Revealing the Role of Anchoring Groups in the Electrical Conduction Through Single-Molecule Junctions”. *Science* 6.14 (2010), pp. 1529–1535.

[45] R. Frisenda, S. Tarkuç, E. Galán, M. L. Perrin, R. Eelkema, F. C. Grozema, and H. S. J. van der Zant. “Electrical properties and mechanical stability of anchoring groups for single-molecule electronics”. *Beilstein Journal of Nanotechnology* 6 (2015), pp. 1558–1567.

[46] M. L. Perrin, R. Frisenda, M. Koole, J. S. Seldenthuis, J. A. C. Gil, H. Valkenier, J. C. Hummelen, N. Renaud, F. C. Grozema, J. M. Thijssen, D. Dulić, and H. S. J. van der Zant. “Large negative differential conductance in single-molecule break junctions”. *Nature Nanotechnology* 9.10 (Oct. 2014), pp. 830–834.

[47] J. J. Parks, A. R. Champagne, T. A. Costi, W. W. Shum, A. N. Pasupathy, E. Neuscamman, S. Flores-Torres, P. S. Cornaglia, A. A. Aligia, C. A. Balseiro, G. K.-L. Chan, H. D. Abruña, and D. C. Ralph. “Mechanical Control of Spin States in Spin-1 Molecules and the Underscreened Kondo Effect”. *Science* 328.5984 (2010), pp. 1370–1373.

[48] K. Reznikova, C. Hsu, W. M. Schosser, A. Gallego, K. Beltako, F. Pauly, H. S. J. van der Zant, and M. Mayor. “Substitution Pattern Controlled Quantum Interference in [2.2]Paracyclophane-Based Single-Molecule Junctions”. *Journal of the American Chemical Society* 143.34 (Sept. 2021), pp. 13944–13951.

[49] H. Vazquez, R. Skouta, S. Schneebeli, M. Kamenetska, R. Breslow, L. Venkataraman, and M. S. Hybertsen. “Probing the conductance superposition law in single-molecule circuits with parallel paths”. *Nature Nanotechnology* 7.10 (Oct. 2012), pp. 663–667.

[50] A. R. Champagne, A. N. Pasupathy, and D. C. Ralph. “Mechanically Adjustable and Electrically Gated Single-Molecule Transistors”. *Nano Letters* 5.2 (Feb. 2005), pp. 305–308.

[51] C. A. Martin, J. M. van Ruitenbeek, and H. S. J. van der Zant. “Sandwich-type gated mechanical break junctions”. *Nanotechnology* 21.26 (June 2010), p. 265201.

[52] D. Xiang, H. Jeong, D. Kim, T. Lee, Y. Cheng, Q. Wang, and D. Mayer. “Three-Terminal Single-Molecule Junctions Formed by Mechanically Controllable Break Junctions with Side Gating”. *Nano Letters* 13.6 (June 2013), pp. 2809–2813.

[53] J. M. Campbell and R. G. Knobel. “Feedback-controlled electromigration for the fabrication of point contacts”. *Applied Physics Letters* 102.2 (Jan. 2013), p. 023105.

[54] K. O’Neill, E. A. Osorio, and H. S. J. van der Zant. “Self-breaking in planar few-atom Au constrictions for nanometer-spaced electrodes”. *Applied Physics Letters* 90.13 (Mar. 2007), p. 133109.

[55] C. Hsu, T. A. Costi, D. Vogel, C. Wegeberg, M. Mayor, H. S. J. van der Zant, and P. Gehring. “Magnetic-Field Universality of the Kondo Effect Revealed by Thermocurrent Spectroscopy”. *Phys. Rev. Lett.* 128 (14 Apr. 2022), p. 147701.

[56] E. Pyurbeeva, C. Hsu, D. Vogel, C. Wegeberg, M. Mayor, H. van der Zant, J. A. Mol, and P. Gehring. “Controlling the Entropy of a Single-Molecule Junction”. *Nano Letters* 21.22 (Nov. 2021), pp. 9715–9719.

[57] A. Gemma and B. Gotsmann. *Will molecules ever sit at the thermoelectric table?* 2021. arXiv: 2108.13705.

[58] M. Korzhuyev and I. Katin. “On the sequence of discovery of the basic thermoelectric effects”. *Journal of Thermoelectricity* 3 (2011), pp. 79–96.

[59] T. J. Seebeck. “Ueber die magnetische Polarisation der Metalle und Erze durch Temperaturdifferenz”. *Annalen der Physik* 82.3 (1826), pp. 253–286.

[60] C. Goupil, H. Ouerdane, K. Zabrocki, W. Seifert, N. F. Hinsche, and E. Müller. *Thermodynamics and Thermoelectricity*. 2016.

[61] J. C. A. Peltier. *Nouvelles expériences sur la caloricité des courans électriques*. 1834.

[62] W. Thomson. “I. Account of researches in thermo-electricity”. *Proceedings of the Royal Society of London* 7 (1856), pp. 49–58.

[63] W. Nernst. “Ueber die electromotorischen Kräfte, welche durch den Magnetismus in von einem Wärmestrome durchflossenen Metallplatten geweckt werden”. *Annalen der Physik* 267.8 (1887), pp. 760–789.

[64] A. F. Ioffe, L. S. Stil’bans, E. K. Iordanishvili, T. S. Stavitskaya, A. Gelbtuch, and G. Vineyard. “Semiconductor Thermoelements and Thermoelectric Cooling”. *Physics Today* 12.5 (May 1959), pp. 42–42.

[65] Y. Sun, Y. Liu, R. Li, Y. Li, and S. Bai. “Strategies to Improve the Thermoelectric Figure of Merit in Thermoelectric Functional Materials”. *Frontiers in Chemistry* 10 (May 2022).

[66] J. Zhang, H. J. Liu, L. Cheng, J. Wei, J. H. Liang, D. D. Fan, P. H. Jiang, L. Sun, and J. Shi. “High thermoelectric performance can be achieved in black phosphorus”. *J. Mater. Chem. C* 4 (5 2016), pp. 991–998.

[67] P. Murphy, S. Mukerjee, and J. Moore. “Optimal thermoelectric figure of merit of a molecular junction”. *Phys. Rev. B* 78 (16 Oct. 2008), p. 161406.

[68] C. M. Finch, V. M. García-Suárez, and C. J. Lambert. “Giant thermopower and figure of merit in single-molecule devices”. *Phys. Rev. B* 79 (3 Jan. 2009), p. 033405.

[69] J. M. Thijssen and H. S. J. Van der Zant. “Charge transport and single-electron effects in nanoscale systems”. *physica status solidi (b)* 245.8 (2008), pp. 1455–1470.

[70] G. D. Mahan and J. O. Sofo. “The best thermoelectric”. *Proceedings of the National Academy of Sciences* 93.15 (1996), pp. 7436–7439.

[71] X. Wang, T. L. R. Bennett, A. Ismael, L. A. Wilkinson, J. Hamill, A. J. P. White, I. M. Grace, O. V. Kolosov, T. Albrecht, B. J. Robinson, N. J. Long, L. F. Cohen, and C. J. Lambert. “Scale-Up of Room-Temperature Constructive Quantum Interference from Single Molecules to Self-Assembled Molecular-Electronic Films”. *Journal of the American Chemical Society* 142.19 (May 2020), pp. 8555–8560.

[72] Q. Li, M. Strange, I. Duchemin, D. Donadio, and G. C. Solomon. “A Strategy to Suppress Phonon Transport in Molecular Junctions Using π-Stacked Systems”. *The Journal of Physical Chemistry C* 121.13 (Apr. 2017), pp. 7175–7182.

[73] J. Vacek, J. V. Chocholoušová, I. G. Stará, I. Starý, and Y. Dubi. “Mechanical tuning of conductance and thermopower in helicene molecular junctions”. *Nanoscale* 7 (19 2015), pp. 8793–8802.

[74] C. J. Lambert. “Basic concepts of quantum interference and electron transport in single-molecule electronics”. *Chem. Soc. Rev.* 44 (4 2015), pp. 875–888.

[75] O. Karlström, H. Linke, G. Karlström, and A. Wacker. “Increasing thermoelectric performance using coherent transport”. *Phys. Rev. B* 84 (11 Sept. 2011), p. 113415.

[76] Y. Kim, W. Jeong, K. Kim, W. Lee, and P. Reddy. “Electrostatic control of thermoelectricity in molecular junctions”. *Nature Nanotechnology* 9.11 (Nov. 2014), pp. 881–885.

[77] L. Rincón-García, A. K. Ismael, C. Evangeli, I. Grace, G. Rubio-Bollinger, K. Porfyrakis, N. Agraït, and C. J. Lambert. “Molecular design and control of fullerene-based bi-thermoelectric materials”. *Nature Materials* 15.3 (Mar. 2016), pp. 289–293.

[78] T. Morikawa, A. Arima, M. Tsutsui, and M. Taniguchi. “Thermoelectric voltage measurements of atomic and molecular wires using microheater-embedded mechanically-controllable break junctions”. *Nanoscale* 6 (14 2014), pp. 8235–8241.

[79] M. Paulsson and S. Datta. “Thermoelectric effect in molecular electronics”. *Phys. Rev. B* 67 (24 June 2003), p. 241403.

2

THEORY

"*You know, I couldn't do it. I couldn't reduce it to the freshman level. That means we really don't understand it.*"

Six Easy Pieces: Essentials of Physics By Its Most Brilliant Teacher by Richard Feynman

In this chapter, we focus our attention on the basic concepts behind charge and heat transport through molecular devices. We will do so in an explanatory way avoiding heavy calculations.

2

Conducting a successful experimental work requires not only a well-prepared sample and a functioning measurement set-up but also investigation of the theory behind the topic of exploration. Of course, that does not indicate that the experimentalist will fully understand all the data points he sees in the equipment, but rather the theory would guide the design of the experiment and would help to understand main trends and highlight the anomalies, that do not match with the theory and should then become the main focus of the investigation.

The goal of this chapter is to provide the reader with a layman-friendly introduction to the theory behind thermoelectric transport in single-molecular junctions. Here, the attention will be focused on explaining the main features of the differential conductance vs. bias and gate voltage (stability diagrams) captured during the measurements (i.e., Coulomb blockade regions, Kondo resonance peaks, co-tunneling regions, etc.). We will discuss the role of a thermal gradient across the junction in electron transport and explain the Onsager relations and their relevance to the thermoelectric effects we observe in this thesis. We will also briefly discuss superconductivity, particularly the superconducting current in long superconductor-normal metal-superconductor junctions that are used for thermometry, and discuss Yu-Shiba-Rusinov bound states. For a more detailed explanation of electron transport in nano-scale objects, we refer the reader to excellent books [1, 2] and papers that cover the theory behind transport in molecular junctions [3, 4]. A comprehensive description of thermoelectric effects is given in [5], and reviewed in [6]. Also, some of the theory required for understanding this thesis is presented in the appendix of chapter 5 (see Zero bandwidth approximation of Anderson model used for fitting the Yu-Shiba-Rusinov peaks) and in Chapter 7 we refer to the supplementary information (SI) of [7], where colleagues performed first-principles simulations to support our findings.

2.1. SIZE

Each experiment starts with setting up the measurements by checking the equipment for malfunctioning and potential offsets. We do it mainly by inspecting the current-voltage characteristics measured on a sample simulator box. A sample simulator is a branch of the resistors with different nominal values. Transport of electrons in this system is very well understood and follows Ohm's law. Meanwhile, the subject of our study is very small, usually not exceeding a few nanometers in size. It is natural to expect that physical behavior changes once the dimensions are reduced. But how? What role does the size play? To answer this question, we should define a few characteristic length scales that govern the physical behaviour of the sample and give a physical meaning to "bigger" and "smaller". Among these measures are: the mean free path

l, which is the average length a charge carrier travels without change of its direction or energy; the phase-coherence length l_ϕ, which is the length over which the charge carrier keeps its coherence; and the Fermi wavelength, λ_F, associated with energy of the carriers participating in transport. To give a feeling of the range of these values we provide numbers for bulk gold at low temperatures: l is usually in the range of 10 nanometers, while l_ϕ is of the order of micrometers and λ_F is around 5 Angstroms. If we now compare the sizes, l_α, of the resistors in the sample simulator, we see that they are much larger than the ones mentioned above. Thus, we expect transport in these resistors to obey the classical descriptions, and follow the Drude formula. As the size decreases and l_α becomes smaller than one of the characteristic lengths mentioned above, quantum effects begin to play a role in the physical behaviour of the sample. One of the examples is the presence of conductance quantization [8] effect (which arises when $l_\alpha < l$). In this regime, the conductance can be expressed as:

$$G = \frac{2e^2}{h} \sum_n t_n, \tag{2.1}$$

where e is the electron charge, h is Planck constant, t_n is the tunneling probability ranging from 0 to 1, and the summing is over all channels that are involved in transport.

As mentioned previously, a single molecule can be as small as 1 nm, and this size is of the order of the Fermi wavelength of the conduction electrons in gold. Therefore, we need to take quantum effects into account to accurately describe the observed phenomena in molecular junctions. Electrons inside the molecule experience spatial confinement. Similarly to the quantum mechanics particle-in-a-box problem [9] we can write down the energy for each level as follows:

$$E_{n_x n_y n_z} = \frac{\pi^2 \hbar^2}{2m} \left(\frac{n_x^2}{a_x^2} + \frac{n_y^2}{a_y^2} + \frac{n_z^2}{a_z^2}\right), \tag{2.2}$$

where n_x, n_y, n_z are quantum numbers, a_x, a_y, a_z are lateral dimensions, and m is the mass of the electron. Assuming all lateral dimensions of the molecule to be approximately 1 nm, the energy level separation is estimated to be of the order of $\Delta \sim 0.4$ eV. However, in individual molecules, this value often varies due to electron-nucleus interactions, which lead to the formation of molecular orbitals.

At the same time, there is another type of energy that needs to be paid to add an electron to a molecule. This energy cost arises due to Coulomb interactions, typically quite strong in small molecules. The classical expression for the charging energy is:

$$E_C = \frac{e^2}{2C} = \frac{e^2}{8\pi\epsilon_0 r}, \tag{2.3}$$

where C is the capacitance of the molecule. Here, we approximate the molecule as a sphere with radius r, of 0.5 nm, and apply the formula for the capacitance of an isolated sphere, with dielectric constant ϵ_0. This allows to estimate the charging energy, $E_C \sim 1.4$ eV. This energy is much larger than the thermal fluctuation energy ($k_B T \approx 25$ meV at $T = 300$ K, here k_B is the Boltzmann constant). Therefore, at room temperature, molecules have a stable number of electrons. To add an extra electron to the molecule one should pay the addition energy, E_{add}, consisting of twice the charging energy and possibly including a contribution from the energy level spacing.

2.2. CONTACTS TO THE MOLECULE, COUPLING

Up to this point, we have considered the molecule without accounting for the environment surrounding it. It is important to highlight that introducing the measurement contacts to the system influences the energy spectrum of the molecule, as the electrons inside the molecule interact with the environment.

For a further description of transport in this system, we treat the golden contacts as ideal metal electron reservoirs in which electrons are in equilibrium and have a defined temperature, T, and electrochemical potential, μ. The amount of the electrons in the contacts can change as they are connected to a voltage source. At a given temperature, we can expect to find electrons in particular energy states according to the Fermi-Dirac distribution:

$$f(E, \mu) = \frac{1}{exp((E-\mu)/k_B T) + 1}. \tag{2.4}$$

At zero temperature, this distribution is a step function and all states below the chemical potential are filled; all states above are empty. With increasing temperature, we change the energy of the electrons in such a way that some states with energy less than the chemical potential become empty, and some higher energy states become filled.

When a molecule connects to the contacts, electrons may move from the contacts to the molecule and back. The rate at which they do, is connected to the strength of the interaction between electrons inside the molecule and those in the contacts, which is also known as the electrode coupling. This coupling is denoted as $\Gamma = \Gamma_S + \Gamma_D$, where $\Gamma_{S,D}$ is the electrode coupling to the source or drain contact, respectively. The characteristic time it takes an electron to tunnel to the source or drain can be written as

$$\tau_{S,D} = \frac{\hbar}{\Gamma_{S,D}}. \tag{2.5}$$

The physics of the device is governed by the difference between this tunneling time and the time scale for interactions within the molecule,

such as the electron-electron, electron-phonon interactions, or other internal relaxation processes. Thus, by comparing the coupling with other energetic scales we can conclude which physical phenomena can be observed in the system. For example, if the coupling is high ($\Gamma >> E_C, \Delta, k_B T$), electrons move frequently between the contacts and the molecule, so their phase does not change. This scenario is often referred to as the strong coupling regime.

In contrast, if the coupling is low ($\Gamma << E_C, \Delta, k_B T$), the electrons stay at the molecule for a long time and do not move often. This leads to dephasing of the electrons moving through the molecule. This situation can be referred to as the weak coupling regime. Coulomb blockade and incoherent transport through a sequence of single electron tunneling processes are characteristic phenomena to be observed in this regime. There is also an intermediate coupling regime when the coupling is comparable to the other energetic characteristics. Below, we will focus mainly on the weak coupling regime.

2.3. TRANSPORT THROUGH THE MOLECULE: SINGLE-LEVEL MODEL, COULOMB BLOCKADE

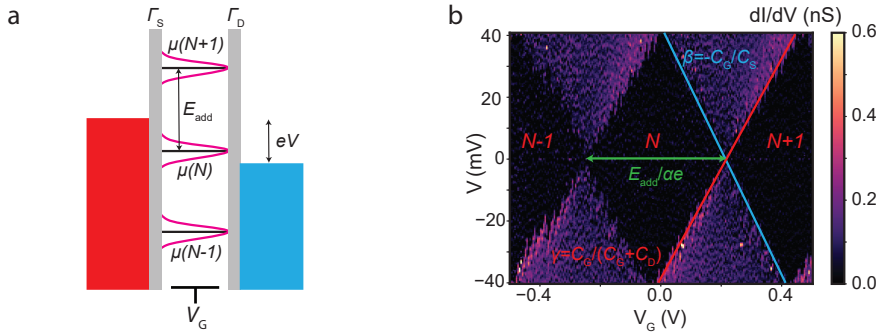

Figure 2.1: Single-electron tunneling (SET) transport in the weak coupling regime. a. Schematic description of transport happening in molecular three-terminal device. The left (red) and right (blue) leads represented by electron reservoirs filled up to the Fermi energy. Here, for simplicity $T_S = T_D = 0$ K. The molecular levels are shown with a black horizontal lines, they are broaden by Lorentzians as depicted with the pink color. b. Coulomb blockade stability diagram measured on a Ferritin nanoparticle (this experiment is not presented in the thesis).

Now we will explain the transport through three-terminal molecular

junctions. For that purpose, we use the chemical potential diagram depicted in figure 2.1a. Here, the source and drain are illustrated as Fermi functions, and the energy states of the molecule are represented as the discrete levels. Each level is labeled with a number, N, corresponding to the amount of electrons inside the molecule. Coupling to the source, Γ_S, and drain, Γ_D , is shown with the grey barriers. Applying a bias voltage moves the electrochemical potentials in such a way that $\mu_S - \mu_D = eV$ with V being the bias voltage (aka "bias window"). At the same time the gate electrode is capacitively coupled to the energy levels of the molecule and can move them in energy, as increasing the gate voltage (V_G) shifts the levels down in energy. Current flows through the system once a molecular energy level, is inside the bias window and is blocked otherwise. This process leads to Coulomb blockade [1] illustrated in figure 2.1b. Here, we plot the differential conductance (dI/dV) as a function of bias and gate voltages, often referred to as stability diagrams. In the figure, fully blockaded regions, Coulomb diamonds, appear separated by regions where a sequential electron tunneling (SET) can take place. The distance between the two Coulomb diamonds provides information about the addition energy, $E_{add} = \alpha e \Delta V_G$, where α is the gate coupling parameter. Usually, the amount of electrons on the molecule is not known and the additional energy is very high, so in the experiment only one level is accessed with the gate voltage, and in a stability diagram one would see parts of the Coulomb diamonds and their edges, see also figure 2.2a.

To get a more quantitative picture, one can follow the derivation of Coulomb blockade theory in the constant interaction model [4]. This model assumes that the spacing between molecular levels does not depend on the amount of the electrons in the molecule and that the coupling to the contacts is not sensitive to N. For derivation purposes, the schematic in figure 2.1a should be changed. Contacts should be seen as reservoirs with electrons that have a certain energy and tunneling barriers should be changed to effective RC circuits where R is inversely proportional to the coupling parameter and C is connected to the ability of the molecule to store the charge. The molecule itself should be seen as an island that can store an integer amount of electrons. Then, the total electrostatic energy for N electrons on the island can be summarized as

$$U(N) = E_C N^2 - eN\frac{V_S C_S + V_D C_D + V_G C_G}{C} + \sum_{n=1}^{N} E_n, \tag{2.6}$$

where C is the total capacitance of the molecule that consists of the sum of capacitances to the source, drain, and gate, $C_{S,D,G}$, and E_n corresponds to the single-particle energy of occupied molecular levels.

By defining the chemical potential of the molecule as

$$\mu(N) = U(N) - U(N-1), \tag{2.7}$$

one can get to expressions for the slopes of the Coulomb edges in the stability diagram by equating this chemical potential to the electrochemical potential of the contacts:

$$V_D = \frac{1}{C_G + C_D}(C_G V_G - \frac{(2N-1)e}{2} - \frac{E_N C}{e}), \tag{2.8}$$

$$V_D = -\frac{1}{C_S}(C_G V_G + \frac{(2N-1)e}{2} + \frac{E_N C}{e}). \tag{2.9}$$

This allows to extract the following values from the recorded experimental stability diagram: $\gamma = \frac{C_G}{C_G+C_D}$, $\beta = -\frac{C_G}{C_S}$, and the gate coupling $\alpha = \frac{C_G}{C}$ (with $\frac{1}{\alpha} = \frac{1}{\gamma} + \frac{1}{|\beta|}$).

Now, let us estimate the absolute value of the current that we measure in this stability diagram. For this, we refer to figure 2.1a, and introduce transmission function $T(E)$, depicted in the picture with the red line. The conductance of the system can be written with the Landauer-Butticker formalism [10] and write down:

$$I(V) = \frac{2e}{h}\int_{-\infty}^{\infty} dE T(E)(f_S - f_D), \tag{2.10}$$

where integration is through all energies. The exact form of $T(E)$ is not known and should be determined from a quantum calculation. However, we can apply a single-level approximation introducing the transmission function as a Lorentzian. We can then write down the expression for current as [3]:

$$I(V) = 4\frac{G_0}{e}\frac{\Gamma_S\Gamma_D}{\Gamma_S+\Gamma_D}\left(\arctan(\frac{\epsilon_0 + (1-\alpha_1)eV}{\Gamma_S+\Gamma_D}) - \arctan(\frac{\epsilon_0 - \alpha_1 eV}{\Gamma_S+\Gamma_D})\right), \tag{2.11}$$

where α_1 is the asymmetry coefficient, $\alpha_1 = \frac{C_S}{C_S+C_D}$. Employing this formula allows to estimate the ratios $\frac{\Gamma_S}{\Gamma_D}, \frac{C_S}{C_D}$ by fitting the formula 2.11 to the data.

2.4. OTHER FEATURES IN THE STABILITY DIAGRAM: EXCITATIONS AND HIGHER-ORDER PROCESSES

In figure 2.2a, we provide a schematic of the differential conductance map, commonly observed during measurements. The map highlights the most frequently observed features; for a more comprehensive

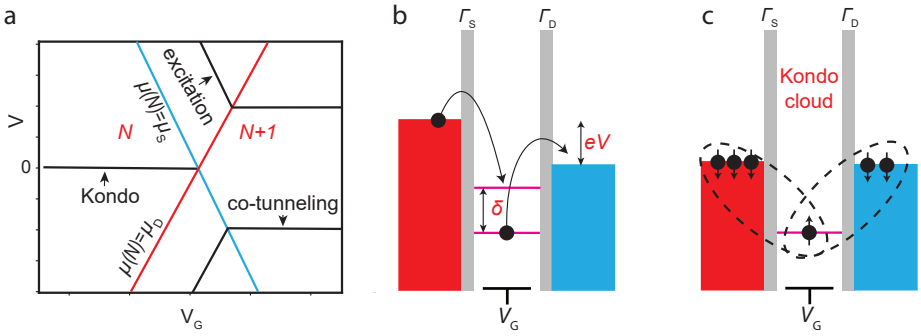

Figure 2.2: Transport features in a stability diagram. a. Schematic stability diagram with excitation levels, Kondo resonance and co-tunneling features. b. Sketch explaining inelastic co-tunneling. An electron tunnels from the molecular level to the Fermi level of the drain lead, while another electron tunnels from the source lead to the excited state of the molecule. The effect is observed once $\delta \geq eV$ c. Sketch explaining Kondo. A spin on the molecule forms a singlet state with conduction electrons in the leads. During a co-tunneling event, this spin is effectively flipped, resulting in the Kondo effect.

discussion, we refer the reader to the "Molecular Electronics An Introduction to Theory and Experiment" book [11]. The key features include lines parallel to the Coulomb blockade edges, attributed to molecular excitations, a zero-bias peak associated with Kondo correlations in the system, and horizontal lines, which can be explained by a co-tunneling mechanism.

2.4.1. EXCITATIONS

When both the excited state and ground state of the molecule lie within the bias window, an increase in current is observed due to the availability of an additional conduction channel for electrons. The signatures of these excitations appear as lines running parallel to the edges of the Coulomb diamonds, occurring in pairs and symmetric with respect to the V_G axis (for a symmetric coupling with $\Gamma_S = \Gamma_D$). These lines terminate when they intersect one of the Coulomb diamond edges. The point of intersection in the stability diagram (V, V_G) provides valuable information about the energy separation between the ground and excited states, given by $\delta = eV$. If $\frac{\Gamma_S}{\Gamma_D} \approx 1$, the intensity of the excitations will be similar for both positive and negative bias. It is also possible for one of the lines not to be visible in the stability diagram,

indicating highly asymmetric coupling.

As the coupling to the molecule increases from the weak to the intermediate regime, higher-order processes begin to contribute to the transport. In this regime, although the Coulomb blockade remains present, additional lines, unrelated to sequential tunneling, emerge within the blockaded regions, signaling the onset of these higher-order effects. We will discuss them in the next two subsections.

2.4.2. ELASTIC AND INELASTIC CO-TUNNELING

Co-tunneling happens when there is no molecular level in the bias window. In first order transport is forbidden, but for a short time scale, dictated by the Heisenberg energy-time uncertainty principle, electrons can move to and from the molecule. Co-tunneling can be elastic and inelastic. In case of elastic co-tunneling, the electron preserves its energy in the process, and in the case of inelastic co-tunneling, the energy changes while moving through the intermediate states because of the additional interactions between the electron and the environment. In figure 2.2b we show the example of inelastic electron tunneling: in the initial state the electron is in μ_N state, it then tunnels to the drain, while at the same time an electron from the source is tunneling to the excited level μ_N^{exc} and stays there. These events occur once $eV \geq \delta$ and lead to the horizontal lines that intersect the Coulomb diamond at the same V that corresponds to the ground-excited states separation energy in the differential conductance map (drawn black lies in figure 2.2a).

2.4.3. KONDO EFFECT

The Kondo effect can also be observed in molecular junctions, manifesting as a complex many-body quantum phenomenon. A simplified illustration is shown in figure 2.2c. In this case, the electron on the molecule with spin 1/2 interacts with the conduction electrons in the contacts via an antiferromagnetic exchange coupling. This interaction leads to the screening of the molecular spin by the electrons in the contacts, resulting in a total singlet ground state for the system. A co-tunneling process could lead to an effective spin flip on the molecule and leads. This mechanism gives rise to the Kondo resonance: a sharp peak in the density of states near the Fermi level. The temperature below which the Kondo effect becomes significant is known as the Kondo temperature, T_K. For a more quantitative understanding of the process we refer to the article by Pustilnik and Glazman [12].

Here, we will focus solely on the formulas that are essential for analyzing the measured data. For simplicity we consider that the total spin on the molecule is $S = 1/2$. In this case, from the full peak width at half maximum (FWHM) of Kondo peak we can estimate the Kondo

temperature using [13]

$$\mathrm{FWHM} = \frac{2}{e}\sqrt{(\pi k_B T)^2 + 2(k_B T_K)^2}. \tag{2.12}$$

Furthermore, T_K can be extracted by measuring the amplitude of the Kondo conductance peak as a function of temperature. To achieve this, one should fit the data to empirical formula [14]:

$$G(T) = G_b + G_I\left(\frac{T^2}{T_K^2}(2^{\frac{1}{s}} + 1)\right)^{-s}, \tag{2.13}$$

where G_b is the background conductance coming from a parallel tunneling pathway between the leads, $G_I = \frac{2e^2}{h}\frac{4\Gamma_S\Gamma_D}{(\Gamma_S+\Gamma_D)^2}$ is the maximum conductance at zero temperature and $s = 0.22$ for a spin-1/2 system.

Finally, T_K can be investigated with the application of a magnetic field to the system. Above a certain magnetic field value, the Kondo peak is expected to undergo Zeeman splitting with $eV = 2g\mu_B B$, where g is Landé factor, and μ_B is Bohr magneton. Typically, the transition point is difficult to determine from the conductance measurements, however, this is possible with thermocurrent measurements (see more details and an example in chapter 4).

2.5. THERMOELECTRIC SIGNAL, ONSAGER RELATIONS

In this section we will give a brief theoretical background behind thermoelectrics in molecular junctions. We will extend it further in Chapter 4.

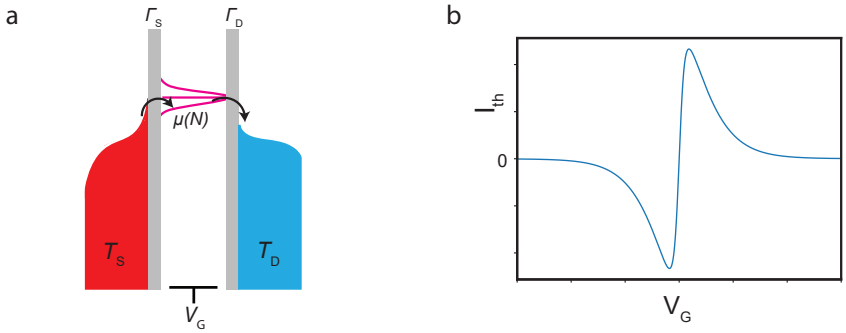

Figure 2.3: Thermocurrent. a. Schematic description of transport in a molecular three-terminal device under $\Delta\mu = 0$ and $\Delta T = T_S - T_D > 0$ conditions. b. Thermocurrent as a function of gate voltage modeled with the Landauer approach.

So far, for most of the figures we considered the Fermi function as a step function, considering $T = 0$ K. We will now investigate what would happen in case $T_{S,D} \neq 0$ K, and $T_S > T_D$. Figure 2.1a would then change to figure 2.3a. Let us follow the current that is going through the system as we change the gate voltage. Here, we consider $V = 0$ V, so $\mu_S = \mu_D$. If the molecular level energy is higher than the electrochemical potential of the contacts, but transmission function of the molecule is non-zero at energies corresponding to high-energy electrons within the Fermi-Dirac distribution, the electrons would move from the left contact to the right, and a negative current governed by the thermal gradient will appear there. As we increase the gate voltage, at a certain moment the molecular level would be in resonance with the contacts and the amount of the electrons that travel from the left to right would be equal to the amount of holes that travel in the same direction; the thermocurrent would be exactly zero. Further increasing V_G causes the hole transport to dominate, leading to a positive thermocurrent. This behavior is illustrated in figure 2.3b.

2.5.1. SINGLE-LEVEL MODEL AND THERMOCURRENT

We can get a quantitative expression for the thermocurrent described in figure 2.3b by applying Landauer-Butticker formula 2.10. In case of a small bias voltage and a small temperature gradient one can write:

$$f_S(E) - f_D(E) = -\frac{\partial f}{\partial E}\Delta\mu - \frac{\partial f}{\partial E}\left(\frac{E - E_F}{T}\right)\Delta T, \tag{2.14}$$

where E_F is the Fermi energy, $\Delta\mu = e\Delta V$, and $\Delta T = T_S - T_D$. Inserting this expression in 2.10 gives an expression for the total current:

$$I = G\Delta V + GS\Delta T, \tag{2.15}$$

where the integral expressions for G and GS can be written:

$$G = \frac{2e^2}{h}\int_0^\infty \mathrm{d}E T(E)\left(-\frac{\partial f}{\partial E}\right), \tag{2.16}$$

$$GS = \frac{2e}{hT}\int_0^\infty \mathrm{d}E T(E)(E - E_F)\left(-\frac{\partial f}{\partial E}\right). \tag{2.17}$$

If we use Sommerfield expansion at low T [15] we find that:

$$S \sim \left(\frac{\mathrm{d}\ln(T(E))}{\mathrm{d}E}\right)_{E_F}. \tag{2.18}$$

As demonstrated by this equation, the thermopower S could be enhanced by sharp features in the transmission function near the Fermi energy. This observation serves as a motivation to use molecules for energy harvesting purposes (see chapter 6).

2.5.2. ONSAGER RELATIONS

When a thermodynamic system is not in equilibrium, it has thermodynamic fluxes J_i caused by thermodynamic forces $\mathcal{F}_i$, e.g. heat flow Q or electron flow J. Fluxes are usually proportional to the forces that cause them when the system is near equilibrium. The Onsager relations describe the general relationships between different fluxes and forces:

$$J_i = \sum_j L_{ij}\mathcal{F}_j, \tag{2.19}$$

where L_{ij} are transport coefficients. The diagonal elements of the matrix characterize the relationship between J_i and the fundamental force that governs it, while off-diagonal terms describe the influence of other forces on it. L_{ij} can also be equal to 0 if there is no connection between J_i and $\mathcal{F}_j$. In addition, the Onsager reciprocal relation states that $L_{ij} = L_{ji}$ in case of the linear response regime.

During transport, carriers (electrons or holes) simultaneously transfer both charge and heat. Meanwhile, the charge current is primarily driven by electrochemical gradients, while the heat flow typically arises from temperature gradients. Thus, it is possible to introduce two forces $\mathcal{F}_1 = \frac{\Delta\mu}{eT} = \frac{V}{T}$, and $\mathcal{F}_2 = \nabla(\frac{1}{T})$. It allows to write the expression for the charge (I_e) and heat (I_q) current in the Onsager way:

$$\begin{pmatrix} I_e \\ I_q \end{pmatrix} = \begin{pmatrix} L_{11} & L_{12} \\ L_{21} & L_{22} \end{pmatrix} \begin{pmatrix} \frac{\Delta V}{T} \\ \frac{\Delta T}{T^2} \end{pmatrix} \tag{2.20}$$

By introducing the well-known physical quantities, such as electrical conductance G, thermal conductance K, Seebeck coefficient S, and Peltier coefficient Π, we can rewrite equation 2.19. First, let us recall that the electrical conductance G characterizes the charge flow per unit voltage in the absence of a temperature gradient:

$$G = \left(\frac{I_e}{\Delta V}\right)_{\Delta T=0} = \frac{L_{11}}{T}. \tag{2.21}$$

The thermal conductance K describes the heat flow in the system per unit of temperature gradient when no charge current is present:

$$K = \left(\frac{I_q}{\Delta T}\right)_{I_e=0} = \frac{1}{T^2}\left(L_{22} - \frac{L_{12}L_{21}}{L_{11}}\right). \tag{2.22}$$

The Seebeck coefficient S defines the voltage build-up due to temperature gradient in an open circuit:

$$S = -\frac{\Delta V}{\Delta T} = \frac{L_{12}}{TL_{11}}, \tag{2.23}$$

and the Peltier coefficient Π represents the amount of heat carried per unit of electrical current when charge carriers move through:

$$\Pi = \frac{L_{21}}{L_{11}}. \tag{2.24}$$

In summary, 2.20 can be rewritten in the following way:

$$\begin{pmatrix} I_e \\ I_q \end{pmatrix} = \begin{pmatrix} G & GS \\ G\Pi & (K + GS\Pi) \end{pmatrix} \begin{pmatrix} \Delta V \\ \Delta T \end{pmatrix}. \tag{2.25}$$

It makes the first equation for charge current the same as equation 2.15. Further on, in this thesis we measure the components of this equation separately, to extract the thermocurrent $I_{th} = GS\Delta T$ and estimate S values.

2.5.3. ZT FIGURE OF MERIT, EFFICIENCY OF MOLECULAR HEAT ENGINE

In comparison to semiconducting counterparts, molecular devices offer a high dimensionless figure of merit ZT:

$$ZT = \frac{GS^2T}{K}. \tag{2.26}$$

This value is characterizing the ratio between the work that can be done by the molecule to the heat flow that is running through it, thus it characterizes the efficiency of heat-to-energy harvesting abilities of the molecular heat engine. The maximal efficiency of a thermoelectric generator is related [6] to ZT:

$$\eta_{max} = \eta_C \frac{\sqrt{(ZT+1)} - 1}{\sqrt{(ZT+1)} + 1 - \eta_C}, \tag{2.27}$$

where η_C is Carnot efficiency, $\eta_C = 1 - \frac{T_D}{T_S}$, as $T_S > T_D$. In case of $ZT \to \infty$, the efficiency of a molecular heat engine would reach this Carnot limit. However, for practical applications, where the molecule can perform real work, it is useful to consider the efficiency for maximum power output. This value is given by the Curzon-Ahlborn efficiency limit [16]:

$$\eta_{CA} = 1 - \sqrt{\frac{T_D}{T_S}}. \tag{2.28}$$

2.6. MOLECULAR JUNCTIONS WITH SUPERCONDUCTING CONTACTS

Finally, in our three-terminal devices, we utilize superconducting contacts that touch the golden bridge. Primarily, they were supposed

to serve only for thermometry applications (see chapter 3), but as described in chapter 5 they can also influence the physics of the whole device.

The discovery of superconductivity occurred in 1911 in the laboratory of Heike Kamerlingh Onnes [17], and it has been extensively studied and exploited in physics ever since. The key characteristic of superconductivity is the loss of electrical resistance in a material below a certain temperature, known as the superconducting critical temperature. For an extensive study of the topic, we refer the reader to the excellent Tinkham book [18]. Here, we will primarily focus on the effects that occur when superconductors are brought into proximity with normal metals or magnetic impurities.

A superconductor is characterized by two key parameters: the superconducting energy gap, Δ, and the phase of the superconducting order parameter, which together describe the macroscopic quantum state of the material. Δ represents the energy required to break a Cooper pair and create excitations. When a normal metal is brought into contact with a superconductor, an intriguing effect can take place. The electron from the normal metal with an energy less than the superconducting gap cannot directly enter the superconductor, however, the superconductor accepts it by pairing it with another electron (of opposite spin and momentum to form a Cooper pair) and reflecting a hole back into the normal metal. This process is also known as Andreev reflection [19]. Now let us consider a situation where two superconductors are connected by a normal metal (SNS junctions). Multiple Andreev reflections are possible in this case. An electron from the normal metal can undergo an Andreev reflection on the first interface with the superconductor, and become retroreflected as a phase-coherent hole. This hole may then move through the normal metal to the other interface, undergo one more Andreev reflection, and be converted back to a phase-coherent electron. As a result, effectively, a Cooper pair from one superconductor travels to the other one without energy dissipation via phase-coherent multiple Andreev reflections. A supercurrent inside the SNS junction occurs, i.e., the normal metal is proximitised. The critical current, the current until which the SNS junction stays fully proximitised when increasing it, is very sensitive to the electron temperature and can therefore be exploited for thermometry.

2.6.1. THERMOMETRY

In chapter 3 we implemented long SNS junctions for thermometry objectives. Here, the characteristic length of the junction was larger than the mean free path but lower than the phase coherence length. Also, $\Delta >> \epsilon_T$ (which serves as a definition of the long junction), where ϵ_T is the Thouless energy related to the rate with which electrons diffuse

across the sample. The Thouless energy can be written as $\epsilon_T = \frac{\hbar D}{L^2}$, where D is the diffusion coefficient in the normal metal and L is the length of the junction. The behavior of the critical current as a function of temperature in long SNS junctions is given in [20]. The solution can be obtained by harvesting a quasi-classical approach based on Green's functions in imaginary space [20, 21] and solving the Usadel equation at all energies [20]. It does not have an analytical expression, but can be written at zero temperature as:

$$eR_N I_C = 10.82\epsilon_T, \tag{2.29}$$

where R_N is a resistance of the normal metal part of the junction and I_C is the critical current. Also, there is an expression for I_C in the high-temperature limit, $k_B T >> \epsilon_T$:

$$eR_N I_C = 64\pi k_B T \sum_{n=0}^{\infty} \frac{L}{L_{\omega_n}} \frac{\Delta^2 \exp(-L/L_{\omega_n})}{(\omega_n + \Omega_n + \sqrt{2(\Omega^2 + \omega_n \Omega_n)})^2}, \tag{2.30}$$

where $\Omega_n = \sqrt{\Delta^2 + \omega_n^2}$, $L_{\omega_n} = \sqrt{\frac{\hbar D}{2\omega_n}}$, and $\omega_n = (2n+1)\pi k_B T$ is the Matsubara frequency, n is integer starting from zero.

2.6.2. BOUND STATES AND YU-SHIBA-RUSINOV STATES

Multiple Andreev reflections can constructively interfere with one another, localize in an area with varying pair potential and form Andreev bound states inside the gap, that also may be observed in transport measurements. In case the superconducting gap of the electrode is much larger than the charging energy of the molecule, a proximity-induced bound state can be established (see for example [22]).

The opposite situation, when the superconducting gap of the electrode is much smaller than the charging energy of the molecule, the formation of a Yu-Shiba-Rusinov state (YSR) appears if the molecule is strongly coupled to the superconductor. In this case, the interaction between the spin on the molecule with the spins of Cooper pairs leads to the formation of bound states inside the superconducting gap. To determine how YSR would show up in a stability diagram, we need to solve the Anderson impurity model in a regime where the charging energy tends to infinity. In the appendix of chapter 5 we will solve this Hamiltonian with zero-bandwidth approximation.

REFERENCES

[1] Y. V. Nazarov and Y. M. Blanter. *Quantum transport: introduction to nanoscience*. Cambridge Univ. Press, 2009.

[2] S. Datta. *Electronic Transport in Mesoscopic Systems*. Cambridge University Press, Sept. 1995.

[3] P. Gehring, J. M. Thijssen, and H. S. J. van der Zant. “Single-molecule quantum-transport phenomena in break junctions”. *Nature Reviews Physics* 1.6 (June 2019), pp. 381–396.

[4] J. M. Thijssen and H. S. J. Van der Zant. “Charge transport and single-electron effects in nanoscale systems”. *physica status solidi (b)* 245.8 (2008), pp. 1455–1470.

[5] X. Wang. *Nanoscale Thermoelectrics*. Springer International Publishing, 2014. isbn: 9783319020129.

[6] G. Benenti, G. Casati, K. Saito, and R. S. Whitney. “Fundamental aspects of steady-state conversion of heat to work at the nanoscale”. *Physics Reports* 694 (June 2017), pp. 1–124. issn: 0370-1573.

[7] A. Canetta, S. Volosheniuk, S. Satheesh, J. P. Alvarinhas Batista, A. Castellano, R. Conte, D. G. Chica, K. Watanabe, T. Taniguchi, X. Roy, H. S. J. van der Zant, M. Burghard, M. J. Verstraete, and P. Gehring. “Impact of Spin-Entropy on the Thermoelectric Properties of a 2D Magnet”. *Nano Letters* 24.22 (2024), pp. 6513–6520.

[8] B. J. van Wees, H. van Houten, C. W. J. Beenakker, J. G. Williamson, L. P. Kouwenhoven, D. van der Marel, and C. T. Foxon. “Quantized conductance of point contacts in a two-dimensional electron gas”. *Phys. Rev. Lett.* 60 (9 Feb. 1988), pp. 848–850.

[9] L. D. Landau and E. M. Lifshits. *Quantum Mechanics: Non-Relativistic Theory*. Vol. V.3. Pergamon Press, 1991, pp. 63–65.

[10] R. Landauer. “Spatial Variation of Currents and Fields Due to Localized Scatterers in Metallic Conduction”. *IBM Journal of Research and Development* 1.3 (1957), pp. 223–231.

[11] J. Cuevas and E. Scheer. *Molecular Electronics: An Introduction to Theory and Experiment*. World Scientific, 2010. isbn: 9789814282581.

[12] M. Pustilnik and L. I. Glazman. “Kondo Effect in Real Quantum Dots”. *Phys. Rev. Lett.* 87 (21 Nov. 2001), p. 216601.

[13] K. Nagaoka, T. Jamneala, M. Grobis, and M. F. Crommie. “Temperature Dependence of a Single Kondo Impurity”. *Phys. Rev. Lett.* 88 (7 Feb. 2002), p. 077205.

[14] D. Goldhaber-Gordon, J. Göres, M. A. Kastner, H. Shtrikman, D. Mahalu, and U. Meirav. “From the Kondo Regime to the Mixed-Valence Regime in a Single-Electron Transistor”. *Phys. Rev. Lett.* 81 (23 Dec. 1998), pp. 5225–5228.

[15] A. M. Lunde and K. Flensberg. “On the Mott formula for the thermopower of non-interacting electrons in quantum point contacts”. *Journal of Physics: Condensed Matter* 17.25 (June 2005), p. 3879.

[16] F. L. Curzon and B. Ahlborn. “Efficiency of a Carnot engine at maximum power output”. *American Journal of Physics* 43.1 (Jan. 1975), pp. 22–24.

[17] H. Onnes. “The Superconductivity of Mercury”. *Comm. Phys. Lab. Univ., Leiden* 122 (1911), pp. 122–124.

[18] M. Tinkham. *Introduction to Superconductivity*. 2nd ed. Dover Publications, June 2004. isbn: 0486435032.

[19] A. F. Andreev. “The Thermal Conductivity of the Intermediate State in Superconductors”. *Zh. Eksp. Teor. Fiz.* 46 (1964). [Sov. Phys. JETP 19, 1228 (1964)], p. 1823.

[20] P. Dubos, H. Courtois, B. Pannetier, F. K. Wilhelm, A. D. Zaikin, and G. Schön. “Josephson critical current in a long mesoscopic S-N-S junction”. *Phys. Rev. B Condens. Matter* 63.6 (Jan. 2001), p. 064502.

[21] W. Belzig, F. K. Wilhelm, C. Bruder, G. Schön, and A. D. Zaikin. “Quasiclassical Green’s function approach to mesoscopic superconductivity”. *Superlattices and Microstructures* 25.5 (1999), pp. 1251–1288. issn: 0749-6036.

[22] T. Meng, S. Florens, and P. Simon. “Self-consistent description of Andreev bound states in Josephson quantum dot devices”. *Phys. Rev. B* 79 (22 June 2009), p. 224521.

3

IMPLEMENTATION OF SNS THERMOMETERS INTO MOLECULAR DEVICES FOR CRYOGENIC THERMOELECTRIC EXPERIMENTS

Thermocurrent flowing through a single-molecule device contains valuable information about the quantum properties of the molecular structure and in particular, on its electronic and phononic excitation spectra, and entropy. Furthermore, accessing the thermoelectric heat-to-charge conversion efficiency experimentally can help to select suitable molecules for future energy conversion devices, which – predicted by theoretical studies – could reach unprecedented efficiencies. However, one of the major challenges in quantifying thermocurrents in nanoscale devices is to determine the exact temperature bias applied to the junction. In this work, we have incorporated a superconductor-normal metal-superconductor (SNS) Josephson junction thermometer into a single-molecule device. The critical current of the Josephson junction depends accurately on minute changes of the electronic temperature in a wide temperature range from 100 mK to 1.6 K. Thus, we present a device architecture which can enable thermoelectric experiments on single molecules down to millikelvin temperatures with high precision.

Parts of this chapter have been published in Appl Phys Let. **122**, 103501 (2023) [1].

3.1. INTRODUCTION

Thermoelectric effects, i.e., the conversion between heat and charge currents, have received renewed interest from the nanoelectronics community [2, 3] and in particular in the field of single-molecule electronics [4, 5]. Recent studies [6–10] show that thermoelectric measurements at cryogenic temperatures contain important information about the physical and quantum-thermodynamic properties of nanoscale and molecular systems, which are hard to access with conventional transport experiments. Furthermore, according to theoretical predictions, molecular devices could achieve a very high dimensionless figure of merit [11] ZT – a quantity that is a measure for the heat-to-charge conversion efficiency. While the highest observed ZT of inorganic materials is currently only [12] about 5.4, the predicted ZT of molecular heat engines could reach values of ≈ 100, which would result in efficiencies close to the Carnot efficiency limit [13]. This efficiency could be even further enhanced at cryogenic temperature [14]. However, to quantify thermoelectric effects it is primordial to know the exact temperature drop across a molecular junction. This is in particular challenging at cryogenic temperature because most thermometers used so far are metal-based resistive sensors with low sensitivity at $T < 20$ K. This work fills this gap by developing a superconducting thermometer, which is sensitive down to mK temperature, and by implementing this thermometer into an electromigrated break junction (EMBJ) device.

Different types of low-temperature thermometry approaches have been explored in the literature, including Johnson Noise thermometry [15], Coulomb Blockade thermometry [16], and Hybrid Tunnel Junction thermometry [17]. In this chapter, we focus on superconductor-normal metal-superconductor (SNS) thermometers because of their excellent properties: low impedance, high sensitivity at low temperatures, and a negligible access resistance [18]. Furthermore, they can be easily implemented into molecular junctions: To this end, we further improve our single-molecule thermoelectric junctions [19], by contacting the source and drain gold contacts with two superconductors, forming a local SNS junction. By measuring the critical current over this SNS junction the temperature can be extracted. In this manner, the contacts can be simultaneously used for thermometry and transport measurements. Here, we use a molybdenum rhenium (MoRe) superconductor, for its high critical temperature of 8.7 K (with a zero-temperature superconducting gap of about $\Delta \approx 1.8 k_B T_C \approx 1.3$ meV).

3.2. DEVICE FABRICATION

The fabrication procedure of the devices on Si wafers with a 285 nm layer of SiO_2 oxide is illustrated in figures 3.1a-d. First (figure 3.1a), the local gate was made by depositing a 1 nm thick adhesion layer

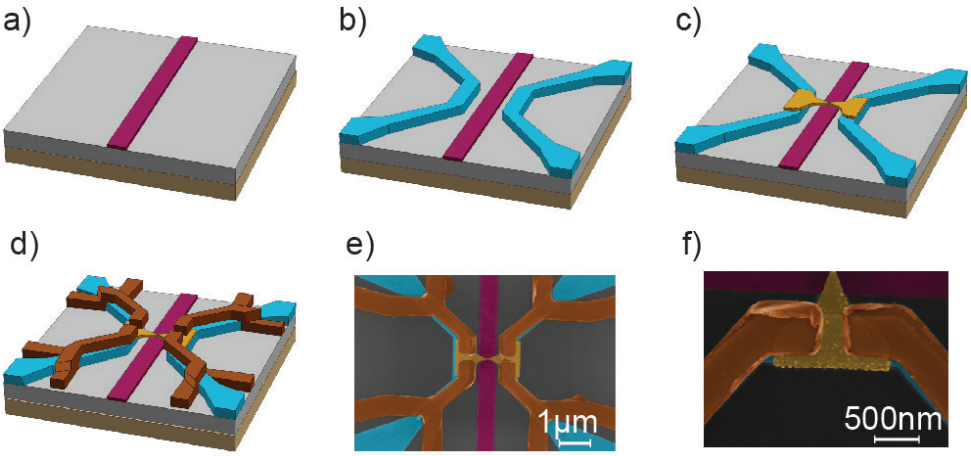

Figure 3.1: a-d. Fabrication process overview. a. Electron beam (E-Beam) deposition of the local back gate electrode (purple). b. Deposition of sample heaters (blue). c. Deposition of 13 nm thick golden bridge (yellow). d. Metal sputtering of superconducting contacts which act as source/drain connections and thermometers. e-f. False-colored scanning-electron microscopy (SEM) images of the fabricated sample. e. False-colored SEM picture of the thermopower device and (f) of the MoRe/Au/MoRe junction; purple: gate electrode; blue: heaters; yellow: gold bridge; brown: MoRe contacts.

of titanium (Ti) and a 7 nm thick layer of palladium (Pd) by standard electron-beam lithography and metal evaporation. This gate thickness is chosen to decrease the heat transport from source to drain [19]. Then, the heater was fabricated by depositing 3 nm of Ti and 27 nm of Pd (figure 3.1b). Subsequently, 10 nm Al_2O_3 was deposited by atomic layer deposition. The aluminium oxide forms the insulating layer between the heater and the electrical contacts, and acts as the dielectric of the local gate. Afterwards, the 13 nm thick Au bridge was made (see figure 3.1c). To get a high-quality gold bridge, the deposition rate during evaporation was kept low (0.5 A/s) and a high vacuum around 10^{-8} mbar was used. In the last step, the 100 nm thick MoRe contacts were created by electron-beam lithography, metal sputtering and lift-off (figure 3.1d).

False-colored scanning electron microscope (SEM) images of the final device together with a zoom-in of an individual Josephson junction are shown in figures 3.1e-f. The spacing between the superconducting contacts varies, and is 253 nm on one side of the gold bridge (thermometer A) and 247 nm on the other side (thermometer B), in the device shown here.

3.3. MEASUREMENT TECHNIQUE

To calibrate the thermometers, devices were cooled down to 100 mK in a dilution refrigerator. A four-point measurement scheme was applied, where a DC current (I_{JJ}) was biased over the junction and the voltage response (V_{JJ}) was simultaneously recorded. A typical DC current-voltage characteristic at 100 mK for thermometer A is shown in figure 3.2a. In the low-current regime, the gold bridge between the two superconductors is proximitized and the Cooper pairs can move from one superconductor to the other without dissipation, forming an Andreev bound state [20]. At a certain current level – i.e., at the switching current (I_{SW}) – the gold weak link changes its state from superconducting to normal, resulting in a voltage increase in the current-voltage ($I-V$) characteristic. From the slope of the $I-V$ characteristic at $I > I_{SW}$ the normal resistance of the gold weak link is calculated and the diffusion coefficient of the electrons in this region is estimated. When ramping the current back, the gold weak link becomes superconducting again at the retrapping current (I_R). This current value typically differs from I_{SW}, which has been explained by capacitive effects in the junction [21] or by heating of the electrons in the normal conducting junction during current sweeping [22]. Since the geometrical capacitance of the junctions used in this work is not sufficiently large to explain the existence of the retrapping current, we attribute the observed hysteresis to heating.

Importantly, the switching to the superconducting state with increasing current bias is a stochastic process [23], so several $I-V$ curves need to be recorded and a mean value of I_{SW} is calculated. To this end, the critical current was measured with an AC technique [24] (see figure 3.2b). In a typical measurement the junction is biased with a 300 Hz triangular AC current from -20 µA to 87 µA. At these settings, gold stays in the normal state only for a short time, preventing the system from heating. Also, the offset is chosen to ensure that the junction stays proximitized in the negative current part and can relax to the base temperature. Using this approach, in a typical experiment we recorded 3000 measurements of switching events with a current resolution of about 0.07 µA.

3.4. RESULTS AND DISCUSSION

Using the AC measurement technique, it is possible to measure I_{SW} at different base temperatures and calibrate the thermometers in the device. The I_{SW} histograms for thermometer A are shown in Figure 3.2c. It can be seen that the switching current is very sensitive to the sample temperature and decreases from 80 µA at 150 mK to 61 µA at 750 mK. We also note an asymmetry in the switching current distributions. Such asymmetry has been observed before [25] and attributed to thermal fluctuations. The stochasticity of switching current

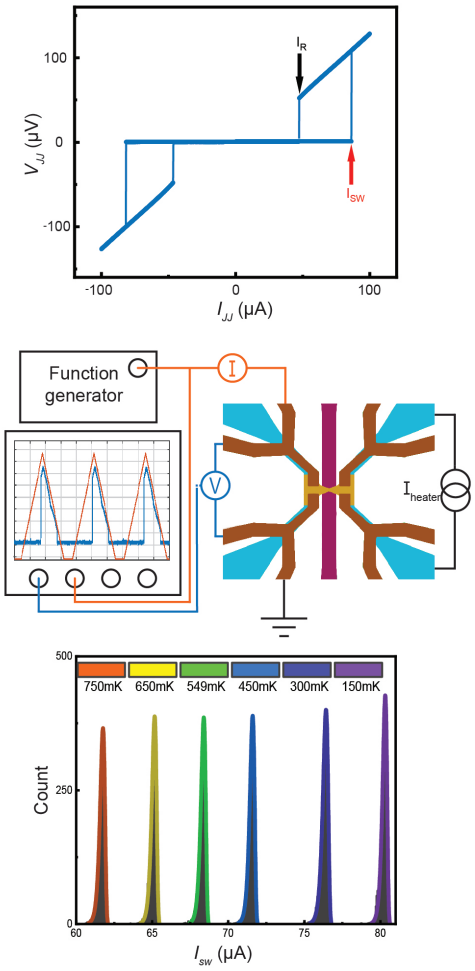

Figure 3.2: a. Voltage vs. current characteristics of a MoRe/Au/MoRe junction. The current was ramped up from 0 to 100 μA, then to -100 μA and back to zero. b. Schematic of the signal path during an AC experiment. A function generator was used to bias the superconducting thermometer with a current I and to measure the voltage drop V on the thermometer. A DC heater current I_{heat} can be applied to one of the micro heaters to generate a thermal bias on the junction. c. Histogram of stochastic switching current I_{SW} of a SNS junction at different temperatures.

is dominated by quantum noise at temperatures below the Thouless energy, while thermal fluctuations become the dominating mechanism

at higher temperatures (see discussion in appendix 3.6.3). From the fits to the current histograms we extract the average switching current $< I_{SW} >$ as a function of temperature for the two thermometers (see figure 3.3). The sensitivity of the thermometers, defined as $\frac{dI_{SW}}{dT}$, in the temperature range from 100 mK to 750 mK is 31.5 μA/K and 42 μA/K for thermometer A and B, respectively (see appendix 3.6.2 for data of other thermometers and appendix 3.6.5 for a comparison with other Au-based SNS thermometers). These values are typical for long SNS junctions and similar to those reported for Nb-Cu-Nb SNS junctions [26]. Furthermore, both thermometers have a temperature resolution better than 15 mK within the investigated temperature range (see appendix 3.6.4 for more details).

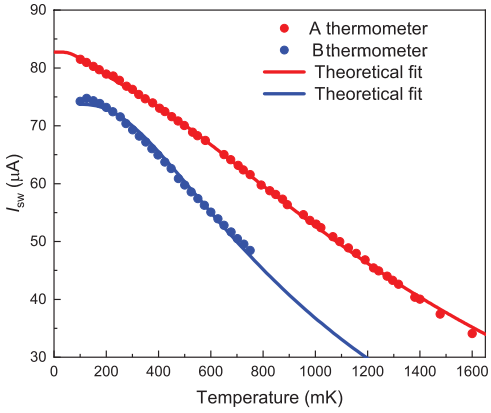

Figure 3.3: Temperature dependence of the averaged switching current, $< I_{SW} >$, for thermometers A (red) and B (blue), respectively. Theoretical fits using the Usadel equation (see main text) are shown as solid lines.

In the following, we discuss the temperature dependence of $< I_{SW} >$ (see figure 3.3). In Josephson junctions this dependence is very sensitive to the interplay between the energy scales of the proximity effect, the Thouless energy, $E_{TH} = \frac{\hbar D}{L^2}$, and the superconducting gap Δ. Here, $D = \frac{v_F l_e}{3}$ is the diffusion coefficient in the normal metal, where v_F, l_e are the Fermi velocity and the elastic mean free path of electrons, respectively, and L is the distance between the superconducting electrodes. In the long junction limit $\Delta > E_{TH}$, the temperature dependence of I_{SW} can be described theoretically by using a quasi-classical approach based on Green's functions in imaginary space [27, 28]; it requires solving the Usadel equation at all energies [28].

We used the *usadel1* package [29] to fit the experimental data. We assumed that the interfaces between the superconductor and the normal

metal are perfectly transparent and that the phase difference between the superconductors is fixed at $\phi = 1.27\pi/2$, similar to Dubos *et al.* [28]. Furthermore, we fixed the normal resistance, R_N, of the junction and Δ of the superconductor to values obtained from transport measurements. The solid lines in figure 3.3 show the resulting fits where the Thouless energy and the suppression coefficient, α, which accounts for the non-ideality of the normal metal-superconductor contact, were used as fitting parameters. Details about the fitting and the resulting parameters can be found in the appendix. We find a suppression coefficient $\alpha \approx 0.5$, similar to the value obtained by Courtois *et.al.* [22]. The Thouless energies, $E_{TH}^{FIT} = 49.4 - 87.2\mu$eV, obtained from the fits in figure 3.3 are close to the values determined from the transport measurements, $E_{TH}^{EXP} \approx 40\mu$eV, which can be calculated as [30] $E_{TH}^{EXP} = \frac{1}{VN(E_F)} \frac{R_Q}{2\pi R_N}$, where $V = L \cdot w \cdot t$ is the volume of the gold film, $N(E_F)$ is the volumetric electronic density of states of gold at the Fermi level and $R_Q = \frac{h}{2e^2}$ is the resistance quantum. $N(E_F)$ can be obtained from the electronic specific heat[31] $\gamma = 0.69 \cdot 10^{-3}$ J mol^{-1} K^{-2} and the molar volume[32] $v = 1.021 \cdot 10^{-5}$ m^3 mol^{-1} as[33] $N(E_F) = \frac{3\gamma}{\pi^2 k_B^2 v} = 1.73 \cdot 10^{28}$ eV^{-1} m^{-3}.

3.5. CONCLUSION

In summary, we implemented an SNS superconducting thermometer in a molecular thermoelectric device. MoRe is used as the superconductor, which allows to perform thermometry in a temperature range from 100 mK to 1.6 K with a high sensitivity of up to 40 µA/K. Other than previously used resistance thermometers, the SNS thermometers developed in this work directly measure the temperature of the electronic system in the immediate proximity to the molecule. Therefore, our devices will allow to e.g. extract the absolute Seebeck coefficient from thermopower measurements on a molecule and will thus pave the way for precise investigations of molecular heat engines.

3.6. APPENDIX

3.6.1. THERMOMETER A: FITS AND DISCUSSION

The best theoretical fit with two parameters α and E_{TH}^{EXP} is shown on figure 3.5. A clear disagreement in the lower temperature range is present that could be related to the fabrication issues. It is possible that edge sputtering artefacts are touching the golden bridge and that the spacing between the MoRe contacts is not homogeneous (see figure 3.4). In this case, the 1D approximation that we use would not be valid and 2D calculations would be required. To avoid complex calculations we decided to focus on a qualitative comparison and simulated the junction

Thermometer	w (nm)	L (nm)	R_N (Ω)	E_{TH}^{EXP} (μeV)	E_{TH}^{FIT} (μeV)	α
A	511	253	1.7	43.0	49.4	0.31
A*	511	253	1.7	43.0	87.2/7.5	0.5
B	503	247	1.8	40.9	31.5	0.47

Table 3.1: Sample parameters. The junctions width (w), length (L), normal resistance (R_N) are listed. The experimental Thouless energy (E_{TH}^{EXP}) is calculated from the normal resistance and geometry of the sample. The Thouless energy, E_{TH}^{FIT}, and suppression coefficient, α are determined from the fit to the data. (Note that the A* and B fits are shown in the main text.)

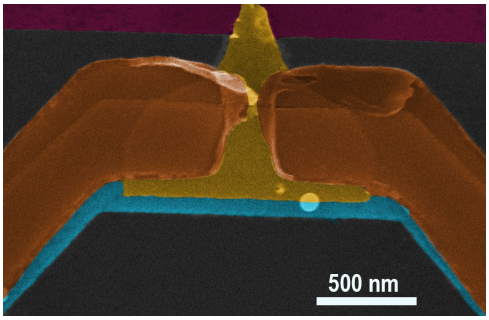

Figure 3.4: False-colored SEM picture of the A thermometer; purple: gate electrode; blue: heaters; yellow: gold bridge; brown: MoRe contacts.

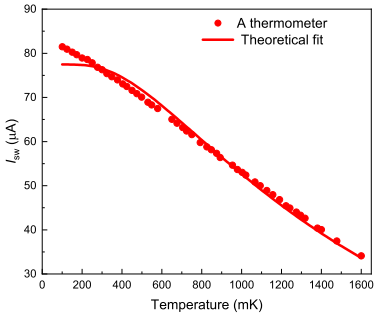

Figure 3.5: Temperature dependence of the averaged switching current, $< I_{SW} >$, for thermometer A and a theoretical fit to the data using the Usadel equation with two parameters α and E_{TH}^{FIT} are shown as solid lines.

with two junctions connected in parallel with $I_{SW} = I_{SW1} + I_{SW2}$, and $R = \frac{R_1 R_2}{R_1 + R_2}$. This approach allows us to get a good fit for the data (see main text for the fit, and fitting parameters in table 3.1). The extracted high Thouless energy for the first junction is two times smaller than the experimental value and corresponds to the part of the thermometer where edge sputtering artefacts are touching gold, thus making the effective distance smaller. The existence of a second Thouless energy $E_{TH} = 7.5\mu$eV can possibly be explained by a discontinuity of the gold film at the step edge over the heater electrode. The heater electrode is 30 nm thick, which is considerably thicker than the 13 nm thick gold film. Thus a parallel SNS junction with a relatively larger volume and normal state resistance, thus smaller Thouless energy, may be formed by the EMBJ constriction.

3.6.2. RESULTS OF OTHER THERMOMETERS

To optimize thermometer design we varied the spacing between superconducting contacts. In figure 3.6 we present the switching current and theoretical fits to the data for two test samples C and D with L of 300 nm and 350 nm, respectively. The parameters of the junctions and estimated theoretical fit values are listed in the table 3.2. We do observe at low temperatures that I_{SW} decreases with increasing length of the normal part of the junction.

	w (nm)	L (nm)	t (nm)	R_N (Ω)	E_{TH}^{EXP} (μeV)	E_{TH}^{FIT} (μeV)	α
C	440	305	14	1.6	38.4	23.1	0.45
D	436	332	14	1.5	36.5	25.8	0.31

Table 3.2: Sample parameters for thermometers C and D. The junctions width (w), length (L), normal resistance (R_N) are listed. The experimental Thouless energy (E_{TH}^{EXP}) is calculated from the normal resistance and geometry of the sample. The Thouless energy, E_{TH}^{FIT}, and suppression coefficient, α, are determined from the fit to the data.

3.6.3. ORIGIN OF THE fLUCTUATIONS OF SWITCHING CURRENT

The JJ switching is a stochastic process, and the distribution of switching currents is influenced by thermal activation and quantum noise/tunneling. The standard deviation normalized by the switching current, $\frac{\sigma}{I_{SW}}$, as a function of temperature is shown in figure 3.7. In figure 3.7, there are two different regions: 1) $\frac{\sigma}{I_{SW}}$ stays constant at the low temperatures. Here, the escape rate has a *quantum origin* with

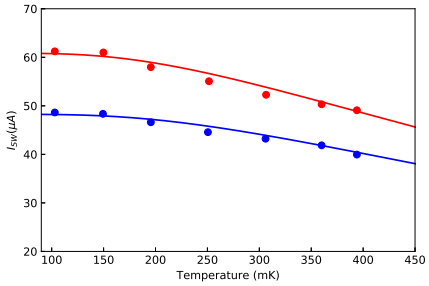

Figure 3.6: Temperature dependence of the averaged switching current, $< I_{SW} >$, for thermometers C (red data points), and D (blue data points). Theoretical fits using the Usadel equation are shown as solid lines.

$\frac{\sigma}{I_{SW}} \approx (\frac{E_{TH}}{E_J})^{(4/5)}$ (E_J Josephson energy) [34] up to temperatures of the order of E_{TH}. 2) At higher temperatures, the process is driven by *thermal activation* and scales with $\frac{\sigma}{I_{SW}} \propto (\frac{T}{E_J})^{(2/3)}$ (see green dashed lines) [34].

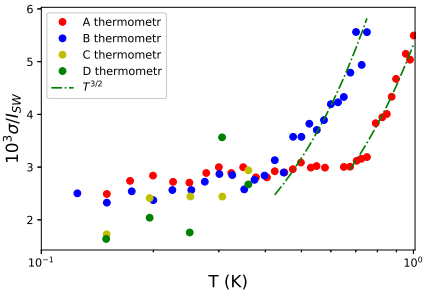

Figure 3.7: The standard deviation σ normalized by I_{SW} vs temperature for A (red), B (blue), C (yellow), and D (green) thermometers. The dashed green line is a theoretical fit assuming thermal activation.

3.6.4. TEMPERATURE RESOLUTION OF THERMOMETERS

The temperature resolution, ϵ_{TR}, of a thermometer is the minimum temperature that the thermometer can distinguish at a certain bath temperature, T_{bath}, of the cryostat. We define this value as $\epsilon_{TR} = -\frac{\Delta I}{dI_{SW}/dT_{bath}}$, where ΔI is full width at half maximum (FWHM) of measured switching current distribution at T_{bath}. In figure 3.8 ϵ_{TR}

is plotted as a function of temperature for thermometers A and B (described in main text), and C,D (see appendix 3.6.2).

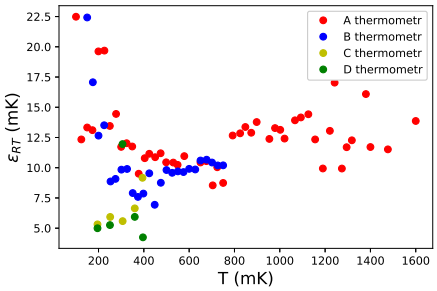

Figure 3.8: The temperature resolution,ϵ_{TR} of thermometers A (red), B(blue), C (yellow), and D (green) vs. temperature.

Thermometers A and B, mentioned in main text, have a resolution between 10 and 15 mK which stays constant in the temperature range from 200 mK to 700 mK. We observe a slight decrease in resolution at the lower temperatures, which we attribute to the fact that the switching current is less dependent on temperature as T approaches zero. The resolution of thermometers C and D is better than for A,B and reaches a value of 5 mK. Despite the fact that thermometers C and D perform better in the investigated temperature range (100 - 400 mK), for molecular devices we prefer to have thermometers with a higher I_{SW} and thus allowing to use them in a large temperature range.

3.6.5. OTHER POSSIBLE THERMOMETERS

SNS	I_{SW} (μA)	R_{N} (Ω)	E_{TH} (μeV)	Δ (meV)	$\frac{\mathrm{d}I_{\mathrm{SW}}}{\mathrm{d}T}^*$ (μA/K)	Source
Al-Au-Al	18	4	19	0.17	25	[35]
Nb-Au-Nb	178	1.7	52.0	1.23	60	[36]

Table 3.3: Parameters reported in literature for SNS junctions that can be implemented in molecular junctions for thermometry. I_{SW} -switching current, R_{N} -normal resistance, E_{TH} - Thouless energy, Δ -superconducting gap, $\frac{\mathrm{d}I_{\mathrm{SW}}}{\mathrm{d}T}^*$ current resolution in a temperature range from the lowest measured temperature to 1 K.

SNS thermometry can be readily implemented in EMBJ devices as it does not require many additional lithographic steps and provides negligible access resistance, which is beneficial for conductance

measurements. In this work, we used MoRe as a superconductor because of its high critical temperature. Below we present a list of parameters for previously reported SNS junctions that could be implemented for thermometry purposes. We limit this table to junctions that have Au as a normal metal because gold is the most used material to contact the molecule in single-molecule studies [37].

REFERENCES

[1] S. Volosheniuk, D. Bouwmeester, C. Hsu, H. S. J. van der Zant, and P. Gehring. “Implementation of SNS thermometers into molecular devices for cryogenic thermoelectric experiments”. *Applied Physics Letters* 122.10 (Mar. 2023), p. 103501.

[2] J. P. Heremans, M. S. Dresselhaus, L. E. Bell, and D. T. Morelli. “When thermoelectrics reached the nanoscale”. *Nature Nanotechnology* 8.7 (July 2013), pp. 471–473.

[3] A. Gemma and B. Gotsmann. “A roadmap for molecular thermoelectricity”. *Nature Nanotechnology* 16.12 (Dec. 2021), pp. 1299–1301.

[4] L. Rincón-García, C. Evangeli, G. Rubio-Bollinger, and N. Agraït. “Thermopower measurements in molecular junctions”. *Chemical Society Reviews* 45.15 (2016), pp. 4285–4306.

[5] K. Wang, E. Meyhofer, and P. Reddy. “Thermal and Thermoelectric Properties of Molecular Junctions”. *Advanced Functional Materials* 30.8 (Oct. 2019), p. 1904534.

[6] M. Josefsson, A. Svilans, A. M. Burke, E. A. Hoffmann, S. Fahlvik, C. Thelander, M. Leijnse, and H. Linke. “A quantum-dot heat engine operating close to the thermodynamic efficiency limits”. *Nature Nanotechnology* 13.10 (Oct. 2018), pp. 920–924.

[7] Y. Kleeorin, H. Thierschmann, H. Buhmann, A. Georges, L. W. Molenkamp, and Y. Meir. “How to measure the entropy of a mesoscopic system via thermoelectric transport”. *Nature Communications* 10.1 (Dec. 2019), p. 5801.

[8] B. Dutta, D. Majidi, A. García Corral, P. A. Erdman, S. Florens, T. A. Costi, H. Courtois, and C. B. Winkelmann. “Direct Probe of the Seebeck Coefficient in a Kondo-Correlated Single-Quantum-Dot Transistor”. *Nano Letters* 19.1 (2019), pp. 506–511.

[9] E. Pyurbeeva, C. Hsu, D. Vogel, C. Wegeberg, M. Mayor, H. van der Zant, J. A. Mol, and P. Gehring. “Controlling the Entropy of a Single-Molecule Junction”. *Nano Letters* 21.22 (2021), pp. 9715–9719.

[10] C. Hsu, T. Costi, D. Vogel, C. Wegeberg, M. Mayor, H. van der Zant, and P. Gehring. “Magnetic field Universality of the Kondo Effect Revealed by Thermocurrent Spectroscopy”. *Phys. Rev. Lett.* 128 (2022), p. 147701.

[11] M. Paulsson and S. Datta. “Thermoelectric effect in molecular electronics”. *Phys. Rev. B* 67 (24 June 2003), p. 241403.

[12] J. Zhang, H. J. Liu, L. Cheng, J. Wei, J. H. Liang, D. D. Fan, P. H. Jiang, L. Sun, and J. Shi. “High thermoelectric performance can be achieved in black phosphorus”. *J. Mater. Chem. C* 4 (5 2016), pp. 991–998.

[13] C. M. Finch, V. M. García-Suárez, and C. J. Lambert. “Giant thermopower and figure of merit in single-molecule devices”. *Phys. Rev. B* 79 (3 Jan. 2009), p. 033405.

[14] A. Harzheim, J. K. Sowa, J. L. Swett, G. A. D. Briggs, J. A. Mol, and P. Gehring. “Role of metallic leads and electronic degeneracies in thermoelectric power generation in quantum dots”. *Phys. Rev. Research* 2 (1 Feb. 2020), p. 013140.

[15] A. Casey, B. Cowan, H. Dyball, J. Li, C. Lusher, V. Maidanov, J. Nyeki, J. Saunders, and D. Shvarts. “Current-sensing noise thermometry from 4.2 K to below 1 mK using a DC SQUID preamplifier”. *Physica B: Condensed Matter* 329 (May 2003), pp. 1556–1559.

[16] J. P. Pekola, K. P. Hirvi, J. P. Kauppinen, and M. A. Paalanen. “Thermometry by Arrays of Tunnel Junctions”. *Phys. Rev. Lett.* 73 (21 Nov. 1994), pp. 2903–2906.

[17] J. M. Rowell and D. C. Tsui. “Hot electron temperature in InAs measured by tunneling”. *Phys. Rev. B* 14 (6 Sept. 1976), pp. 2456–2463.

[18] B. Dutta. “Energetics in metallic-island and quantum-dot based single-electron devices”. Theses. Université Grenoble Alpes, Nov. 2018.

[19] P. Gehring, M. van der Star, C. Evangeli, J. J. Le Roy, L. Bogani, O. V. Kolosov, and H. S. J. van der Zant. “Efficient heating of single-molecule junctions for thermoelectric studies at cryogenic temperatures”. *Applied Physics Letters* 115.7 (2019), p. 073103.

[20] J. A. Sauls. “Andreev bound states and their signatures”. *Phil. Trans. R. Soc. A.* 376 (2018).

[21] W. C. Stewart. “Current-voltage characteristics of josephson junctions”. *Applied Physics Letters* 12 (1968).

[22] H. Courtois, M. Meschke, J. T. Peltonen, and J. P. Pekola. “Origin of Hysteresis in a Proximity Josephson Junction”. *Phys. Rev. Lett.* 101 (6 Aug. 2008), p. 067002.

[23] L. Angers, F. Chiodi, G. Montambaux, M. Ferrier, S. Guéron, H. Bouchiat, and J. C. Cuevas. “Proximity dc squids in the long-junction limit”. *Phys. Rev. B Condens. Matter Mater. Phys.* 77.16 (Apr. 2008).

[24] B. Dutta, D. Majidi, N. W. Talarico, N. Lo Gullo, H. Courtois, and C. B. Winkelmann. “Single-Quantum-Dot Heat Valve”. *Phys. Rev. Lett.* 125 (23 Dec. 2020), p. 237701.

[25] K. Spahr, J. Graveline, C. Lupien, M. Aprili, and B. Reulet. “Dynamical voltage-current characteristics of SNS junctions”. *Phys. Rev. B.* 102.10 (Sept. 2020).

[26] P. Dubos, H. Courtois, O. Buisson, and B. Pannetier. “Coherent low-energy charge transport in a diffusive S-N-S junction”. *Phys. Rev. Lett.* 87.20 (Nov. 2001), p. 206801.

[27] W. Belzig, F. K. Wilhelm, C. Bruder, G. Schön, and A. D. Zaikin. “Quasiclassical Green’s function approach to mesoscopic superconductivity”. *Superlattices and Microstructures* 25.5 (1999), pp. 1251–1288. issn: 0749-6036.

[28] P. Dubos, H. Courtois, B. Pannetier, F. K. Wilhelm, A. D. Zaikin, and G. Schön. “Josephson critical current in a long mesoscopic S-N-S junction”. *Phys. Rev. B Condens. Matter* 63.6 (Jan. 2001), p. 064502.

[29] P. Virtanen and T. Heikkilä. “Thermoelectric effects in superconducting proximity structures”. *Appl. Phys. A* 89 (2007). Source code available at http://ltl.tkk.fi/ theory/usadel1/, p. 625.

[30] M. Janssen. *Fluctuations and Localization in Mesoscopic Electron Systems*. WORLD SCIENTIFIC, 2001.

[31] G. R. Stewart. “Measurement of low-temperature specific heat”. *Review of Scientific Instruments* 54.1 (1983), pp. 1–11.

[32] C. N. Singman. “Atomic volume and allotropy of the elements”. *Journal of Chemical Education* 61.2 (1984), p. 137.

[33] P. A. Beck and H. Claus. “Density of States Information from Low Temperature Specific Heat Measurements”. *J. Res. Natl. Bur. Stand. A Phys. Chem.* 74A.3 (1970), pp. 449–454.

[34] L. Angers, F. Chiodi, G. Montambaux, M. Ferrier, S. Guéron, H. Bouchiat, and J. C. Cuevas. “Proximity dc squids in the long-junction limit”. *Phys. Rev. B* 77 (16 Apr. 2008), p. 165408.

[35] M. Jung, H. Noh, Y.-J. Doh, W. Song, Y. Chong, M.-S. Choi, Y. Yoo, K. Seo, N. Kim, B.-C. Woo, B. Kim, and J. Kim. “Superconducting Junction of a Single-Crystalline Au Nanowire for an Ideal Josephson Device”. *ACS Nano* 5.3 (Feb. 2011), pp. 2271–2276.

[36] A. De Cecco, K. Le Calvez, B. Sacépé, C. B. Winkelmann, and H. Courtois. “Interplay between electron overheating and ac Josephson effect”. *Phys. Rev. B* 93 (18 May 2016), p. 180505.

[37] T. A. Su, M. Neupane, M. L. Steigerwald, L. Venkataraman, and C. Nuckolls. “Chemical principles of single-molecule electronics”. *Nature Reviews Materials* 1.3 (2016).

4

THERMOPOWER MEASUREMENTS WITH THE DOUBLE LOCK-IN TECHNIQUE

“Old man,” said a fellow pilgrim near,
“You are wasting your strength with building here;
Your journey will end with the ending day,
You never again will pass this way;
...
The builder lifted his old gray head;
“Good friend, in the path I have come,” he said,
“There followed after me to-day
A youth whose feet must pass this way.
This chasm that has been as naught to me
To that fair-haired youth may a pitfall be;
He, too, must cross in the twilight dim;
Good friend, I am building this bridge for him!”

"The Bridge Builder" by Will Allen Dromgoole

4.1. INTRODUCTION

The journey of exploring thermoelectric effects, i.e., the interplay between electrical currents and heat flow, dates back to the end of the XVIII century with the first experiments of Aepinus, Galvani and Volta. Particularly, Alessandro Volta [1] observed movement in the body of a frog when an arch with a temperature gradient was immersed into two glasses of water connected by the animal's body. After experimenting with various arches and temperatures, he concluded that the thermoelectric force arose from the temperature difference. This experiment was conducted almost 30 years before the famous Seebeck work [2] on "thermomagnetism", describing a magnetic needle changing its angle under the influence of a current caused by a temperature difference in a closed bismuth-copper loop. Despite an incorrect interpretation (later corrected by Oersted [3]) provided in the study, Seebeck's work had a huge impact on the field, and nowadays a coefficient that characterizes the voltage build-up in a wire under a temperature difference carries his name. Shortly thereafter, the inverse effect was observed by Peltier [4] and a theoretical explanation [5] by Lord Kelvin (a.k.a. William Thomson) followed. Thomson not only demonstrated that the effects described by Seebeck and Peltier were related and had the same nature but also predicted that generation or absorption of heat should be observed when current passes through a homogeneous wire under a temperature gradient (Thomson effect).

Observations of thermoelectric effects immediately sparked interest in their potential applications for different types of coolers, heat pumps, etc. The quest for optimizing the efficiency of heat engines stimulated both theoretical and experimental studies in the field. Theoretical works of Alternkitch focused on the efficiency of thermopiles [6] and deliberated over potential materials that could work close to the Carnot limit. Onsager works [7], as well as work by Callen [8] contributed to the understanding of fundamental processes behind thermoelectric effects and described these effects on a phenomenological level. At the same time, experimental studies predominately focused on the investigation of different semiconductors as prospective candidates for thermoelectric applications. In Ioffe's group, a selection of prospective materials was measured and evaluated, eventually leading to the development of one of the first commercial thermoelectrical power generators [9]. Ioffe also started using the intrinsic material figure of merit, Z, to characterize the quality and efficiency of a thermoelectric material [10], which is still widely used nowadays ($Z = \frac{S^2\sigma}{k}$, where S is the Seebeck coefficient of a material and σ and k are the electrical and heat conductivity, respectively). Consequently, the material research community gained understanding on candidates of potential "thermopower" materials with focus on highly doped semiconductors.

Despite these extensive studies and high hopes, the field slowed

down in the 1950-1960s. The ZT values peaked around 1 (currently, the highest figure of merit, 5.4, belongs to few-layer black phosphorus [11]), and for a long time, higher values were not considered realistic to be achieved. Even nowadays, many devices continue to employ materials that were investigated more than 50 years ago. For example, bismuth telluride, the heat conduction of which was measured by Goldsmid in 1958 [12], can be found in modern household refrigerators. Most of the current spaceships and autonomous satellites are powered by radioisotope thermoelectric generators that contain silicon-germanium thermocouples (thermoelectric properties of which were measured [13] in 1962). The Voyager 1 is still sending signals to Earth despite the degradation of the thermocouples that generate the energy harvesting from the heat of Plutonium-238.

The interdependence of electrical conductivity, the Seebeck coefficient and thermal conductivity fundamentally constrains the figure of merit Z, as altering one of these parameters typically affects the other two. This results in a limited increase in the figure of merit when optimizing one of them. For instance, enhancing the Seebeck coefficient often leads to a reduction in electrical conductivity. This interdependence stimulated scientists to think in other directions and try to utilize quantum mechanics principles to overcome this issue. At the end of the XX-th century two breakthrough theoretical works by Hicks and Dresselhaus appeared [14, 15]. They showed that by changing the dimension of the sample and harvesting quantum confinement, one can dramatically change the Z value. In Ref. [15] they calculated that the figure of merit of a 2D 4-nm quantum well Bi_2Te_3 is two times higher than in its bulk counterpart, and by going to 1D [14] this value can be further enhanced. Numerous experimental and theoretical studies have emerged investigating the potential of thermoelectricity at the nanoscale (see Ref. [16] and the references therein). One of the representatives of quantum objects is molecules. These nm-size entities can have remarkably high energy harvesting abilities [17, 18]. By utilizing their interference features [19], manipulating coupling to the leads [20] or changing their length [21] the figure of merit can be enhanced.

Thus, investigating the thermoelectric properties of molecules is an interesting field predominately governed by the search for the best heat-to-energy converter. To do it there should be a method to extract the components of the figure of merit. It is difficult to obtain the heat conductance during the experiment and this value is often calculated theoretically. Meanwhile, the electrical conductance and Seebeck coefficient can be determined experimentally. One of the ways would be to first measure the open-circuit voltage after applying a temperature gradient, and then measure the conductance under a small bias voltage. These two values strongly depend on the

position of the molecular energy levels relative to the electrochemical potentials of the contacts, which is why gate sweeps are commonly performed. Unfortunately, during the gate ramping, the electrostatic environment of the molecule can be changed, i.e., the molecular level can shift from one gate trace to another one, and that would lead to an error in the estimation of $S^2(V_G)G((V_G))$. To avoid this problem the double lock-in method was developed [22]. This method enables simultaneous measurement of thermocurrent and conductance, which, together with thermometry, provides the necessary data to calculate the numerator of the figure of merit. Additionally, it allows experiments to be conducted under non-zero bias voltage, which is advantageous, as thermoelectric measurements can reveal information not easily captured by conventional transport techniques (see, for example, [23]).

In this chapter, we will focus our attention on the thermopower measurements by the AC double lock-in technique. We start with a description of the method, providing a comprehensive guidance on how to perform the measurements and pointing out the systems where the method could be utilized. Special attention will be paid to accurately extracting the thermocurrent signal from the measurements (sign and prefactor) to avoid further inconsistencies in the literature. Subsequently, we will describe different temperature-voltage regimes that one can observe in the experiments and will link the readings of the lock-ins to real physical values such as the Seebeck coefficient, Power factor, etc.

The data to support this study is collected on various molecular and golden grain measurements, which are treated as single-level quantum dots. Therefore, Onsager equations hold for the zero-bias measurements in linear regime, where the thermocurrent is proportional to the temperature difference, $I_{th} \propto \Delta T$. We demonstrate that I_{th} can be linked to the open-circuit thermovoltage as $I_{th} = -GV_{th}$, where G is the electrical conductance. Thermopower, S, also known as the Seebeck coefficient, can then be derived as $S = -\frac{V_{th}}{\Delta T} = \frac{I_{th}}{G\Delta T}$.

Subsequently, we focus our attention on the high-bias regime. This is specifically interesting in case the conductance is temperature-sensitive in the range of applied temperature gradients. Finally, we conclude by providing a checklist containing recommendations and remarks for thermopower measurements in single-molecule devices.

4.2. METHOD

To simultaneously measure conductance and thermocurrent, we apply a double lock-in protocol. A scheme of the method with a scanning electron microscope image of a typical molecular device is depicted in figure 4.1. We utilize a small AC component on top of the DC bias voltage at a constant frequency, $\omega_1 = 13$ Hz, synchronously with an alternating

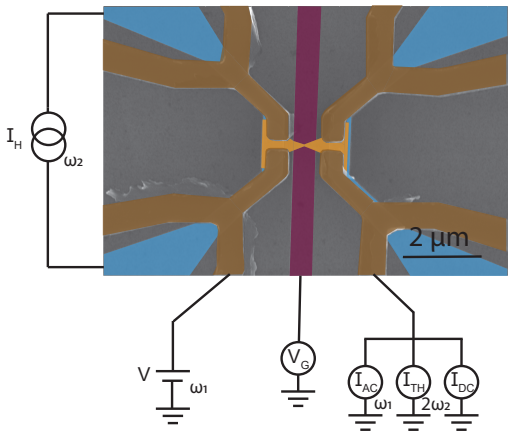

Figure 4.1: AC double lock-in measurement protocol applied to a typical molecular device.

current through the heater at $\omega_2 = 3$ Hz to demodulate the signal into different components. To disentangle the different components, the ammeter's readout is connected to a Keithley, a voltmeter measuring the DC output signal, and to two lock-in amplifiers recording the signals at ω_1 and $2\omega_2$. The current flowing through the molecule can be written as $I = I_{DC} + I_{\omega_1} + I_{2\omega_2}$. Here, I_{DC} is the DC component from which the conductance is extracted, $G = \frac{I_{DC}}{V}$, I_{ω_1} is the AC component that characterizes the differential conductance $G^* = \frac{dI_{\omega_1}}{dV}$, and $I_{2\omega_2}$ is the current related to the temperature gradient applied over the molecule. It is important to note that I_{DC} always contains a small DC component resulting from the temperature gradient (usually for molecular devices this component is at least 2 orders lower and in most cases can be neglected).

As described previously, $I_{2\omega_2}$ is the current caused by the temperature gradient over the molecule that will be further referred to as the thermocurrent:

$$I_{th} \propto \Delta T \propto P \propto \sin^2(\omega_2 t) \propto \frac{1 - \cos(2\omega_2 t)}{2}.$$

The current through the heater, I_{heater}, generates Joule heating with power, P, that leads to the generation of a temperature gradient over the molecule, ΔT. In the linear approximation (i.e., low I_{heater} and low T), $\Delta T \propto P$ and the generated signal has two components: a DC one and an AC one at $2\omega_2$. It is important to highlight that the AC signal is shifted by $\frac{\pi}{2}$ so that the thermocurrent signal occurs at the Y component of the

lock-in at the second harmonic of the signal sourced on the heater. To extract the thermocurrent, a factor of $-2\sqrt{2}$ has to be taken into account (see subsection 4.2.3), where -2 is the result of the transformation between the heater current and the temperature gradient enhancement, and $\sqrt{2}$ because of the working principle of the lock-in amplifier that displays the signal in V_{rms}. Below, we show that $I_{2\omega_2}$ multiplied by this prefactor matches DC measurements at I(V,T,ΔT)-I(V,T,0). Adding the prefactor is important as it contains physical information. First, by the sign of the signal one can judge if transport is dominated by electrons or holes (negative I_{th} corresponds to electron transport). Secondly, correct estimations of the Seebeck coefficient and Power Factor require the right prefactor.

In the next subsectioon, we provide snapshots of the used equipment, which are a valuable starting point for conducting the measurements. It is essential to select the correct frequency for accurate measurements. Firstly, the frequencies must be sufficiently spaced apart, so that they do not cross talk (the frequency difference between ω_1 and $\omega_2/2\omega_2$ should be sufficiently larger than the bandwidth of the lock-in low-pass filter). Secondly, lower frequencies are preferable to avoid spurious capacitive effects and to make sure that the temperature of the system is changing quasiadiabatically. Lastly, the frequencies should be moved far away from potential sources of noise (i.e., from 50/60 Hz). Additionally, it is worth keeping in mind that the time of acquiring the signal depends on the measured frequency. For experimental purposes, we recommend using specific frequencies based on our previous investigations. For instance, $\omega_1 = 13$ Hz, and $\omega_2 = 3$ Hz has been used for single-molecule measurements [24–26], and $\omega_1 = 91$ Hz, and $\omega_2 = 17$ Hz for experiments on a graphene quantum dot [27].

4.2.1. MEASUREMENT SET-UP

In this subsection, we will extend the description of the measurement protocol with the double lock-in technique focusing attention on the connections and providing a coherent step-by-step guide on the measurement itself. The experiment is done with two Standford Research SR830 digital lock-in amplifiers, two Keithley multimeters (Keithley 2100 and Keithley 2700), and with a home-built IVVI Rack [28] with voltage/current sources (S1d, S3b/S4c) and current/voltage measure modules (M1b/M2m). The specific details of each module (like input/output resistances, maximum voltage swing, noise level, bandwidth, etc.) can be found online [28]. Further on we specify some crucial information for the experiment settings; for convenience we indicate the settings that were used during Sme-2Os measurements as described in Chapter 6.

The measurement set-up is illustrated in figure 4.2. The IVVI Rack

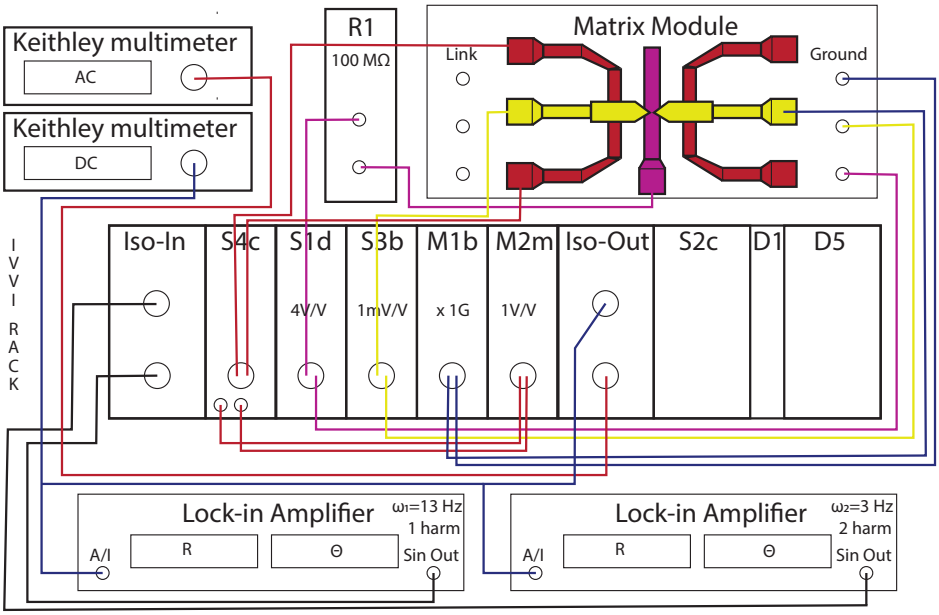

Figure 4.2: Set-up for thermopower measurements. Left lock-in sources the AC bias voltage to the sample through the S3b voltage source module at a constant frequency of $\omega_1 = 13$ Hz. At the same time, the second lock-in supplies the current to the heater at $\omega_2 = 3$ Hz with the help of the S4c voltage-to-current converter. The output voltage of the S4c module is recorded with a Keithley multimeter and provides information about the resistance of the heater. Then two lock-ins simultaneously measure the differential conductance (at ω_1) and thermocurrent (at $2\omega_2$) by reading the voltage from the M1b I-Measure module. Second Keithley multimeter monitors the DC component of the current, revealing information about the conductance of the system. All the modules are located on the IVVI Irack board and connected to the sample vias Matrix Module. Instead of real pins on the Matrix Module, the schematic of the molecular EMBJ device is shown. Here the different parts of the sample are highlighted with colors: purple (gate), red (heaters), and yellow (contacts to the gold bridge).

is the central unit that sends and receives the signals from and to the sample, employing different interchangeable modules. These modules can be controlled internally via a computer or externally by sending the

voltage signal from lock-in amplifiers to the Iso-In module. The signal is measured by M-modules and converted to a voltage, which further can be read out from the Iso-Out module. In this measurement we use the S3b module as the voltage bias source. The DC component is controlled via the internal DAC value of the IVVI Rack. Meanwhile a small AC component is supplied from the lock-in amplifier (at $\omega_1 = 13$ Hz; sine out) which is connected to Iso-In 2. The AC amplitude in the measurements is 10 μV. There is a factor of 0.01 for the signal that goes from Iso-In 2 to S3b (can be changed by rewiring the S2c summing module) and together with the S3b range (we use 1 mV/V for low bias measurements) the required lock-in amplitude is 1 V. Gate voltage is controlled by the S1d module that is connected to the gate contact through a 100 MΩ series resistance to ensure minimal gate currents during voltage ramping and avoid electrical discharges from the gate to the device. Temperature gradient is obtained by applying a current through the heater with the means of S4c I-source. The amplitude of the current is determined by the amplitude of the second lock-in ($\omega_2 = 3$ Hz) and the range of S4c that for Sme-2Os was chosen to be 1 mV/V. To obtain this, the output of the lock-in amplifier is connected to Iso-In 1 that is wired to the first slot of IVVI Rack, where S4c is located. Connection of M2m voltage measure module to the monitor output of the S4c module grands us the ability to read the voltage output of the current source. By measuring this value using a Keithley instrument in AC mode, we can estimate the resistance of the heater (440 Ω). The electrical current of the molecular device is measured with M1b I-measure module with further 0.1G A/V amplification. The output signal is then split between both lock-in amplifiers (see their settings in table 4.1) and second Keithley instrument operating in DC mode.

Typically, the measured differential conductance of the molecular devices at zero-bias ranges from tens of μS to nS; at the same time the thermocurrent in the linear regime rarely exceeds hundreds of pA, thus the correct amplifiers and filters should be applied. The M1b I-measure module allows to amplify the signal by a maximum of 100 GV/A and to perform measurements with a noise floor of $5\frac{\text{fA}}{\sqrt{\text{Hz}}}$ (at a multiplication of 1 GV/A). The energy that goes back to the device from the module is low and can be neglected, but that leads to a drawback caused by high internal resistance (R_{int}) of the I-measure module. This resistance, depending on the range of amplification, should be taken into account during the measurements to estimate the real voltage drop on the measured device. We recommend to avoid a situation where $R_{\text{int}} > \frac{R_{\text{sample}}}{10}$, and if it is not possible then the data should be corrected for the voltage drop over R_{int}. Frequently, amplification used for molecular devices is 0.1 GV/A ($R_{\text{int}} = 102$ kΩ) or 1G V/A (($R_{\text{int}} = 1$ MΩ), and these values could be lowered by one order by choosing the Low-Rin knob instead of the Low-Noise one. Also, the non-zero resistance of

the ammeter can play the role of active load and should be considered during heat-to-energy characterization of the molecular device.

	Lock-in 1 (G)	**Lock-in 2 (I_{th})**
Amplitude	1 V	0.1 V
Frequency	13 Hz	3 Hz
Phase	0°	0°
Harmonic	1	2
Source	Internal	Internal
Trig	Sine	Sine
Time constant	1 s	1 s
Slope/Oct	18 dB	18 dB
Sync < 200 Hz	Off	On
Sensitivity	50 mV	500 μV
Reserve	Normal	Normal
Filters	Nan	Nan
Signal input	A, DC, Float	A, DC, Float
Display	R, θ	X,Y

Table 4.1: Lock-in settings during thermopower investigation of the Sme-2Os molecule.

Finally, a step-by-step guide to perform thermopower measurements on the molecular device is the following:

- Perform a low-bias DC gate trace in the accessible voltage range (for 10 nm Al_2O_3 that is used in the device design illustrated in figure 4.1, the safe voltage range is [-7.5 .. 7.5] V). The recommended starting bias is 0.1 mV; this value can be increased in case the gate sweep does not show any signatures of molecular presence (e.g. this could happen in a case of Franck-Condon blockade [29] or spin blockade [30]). The DC voltage below 5 mV is considered to be safe for the molecule, but extra care in slow ramping should be present to avoid reconfiguration of the molecule inside the electromigrated gap and potential damaging of the sample. The quality of the gate oxide can be extracted from the background slope of the gate trace and the resistance between gate and ground must exceed 100 GΩ.
- Set up the lock-in amplifiers (for starting point see table 4.1).
- Put lowest possible AC bias voltage that allows recording the differential conductance (recommended starting point is 5 μV). Verify that the $|\theta| \leq 5°$ of the left lock-in (the one that measures differential conductance); θ can be higher when passing the charge degeneracy point as the conductance can change by orders of magnitude.

- Apply a reasonable heater current from the second lock-in. The value should be determined experimentally and should satisfy few conditions: being small, so that the double lock-in method is valid, and in the linear regime but large enough to be able to detect a signal. We recommend using $P = 4.4 \times 10^{-10}$ W at 300 mK, which for the used sample design creates a 50 mK temerature difference, and $P = 2.6 \times 10^{-8}$ W power at 1.7 K as a starting point, that leads to a 0.4 K gradient across the junction. Verify that the θ of the second lock-in is close to ±90°, so that the whole signal is in the Y-component.

- Cross-check that there is no signal at ω_2 and $3\omega_2$. The last one indicates leakages and parasitic capacitance couplings.

4.2.2. THERMOCURRENT, THERMOVOLTAGE, SEEBECK AND RELATIONS BETWEEN THEM.

In this subsection, we discuss the relations that connect the thermocurrent, the thermovoltage and the Seebeck coefficient, addressing a sign discrepancy that is present in some of the past literature. In particular, we will justify why the thermocurrent and the thermovoltage have the opposite sign, by connecting the charge carrier type that I_{th}, V_{th}, and S predict, when we heat the source side and keep the drain side at base temperature. Here, we will provide an experimental confirmation why the relations should be written as:

$$S = -\frac{V_{\text{th}}}{\Delta T}, \qquad I_{\text{th}} = -GV_{\text{th}}. \tag{4.1}$$

We performed thermocurrent measurement with the double lock-in technique on a junction with the molecule $[Zn(Tpy)_2](ClO_4)_2$. The zero-bias gate traces can be seen in figure 4.3a. The differential conductance shows a pronounced Fano resonance that arises from quantum interference. Strikingly, the measured simultaneously thermocurrent is very asymmetric and gives a high $I_{\text{th}} = 150$ fA for a temperature difference of not more than 40 mK across the junction at a base temperature of 630 mK. The direct measurement of thermovoltage (red curve in figure 4.3b) on the same configuration also exhibits the same asymmetry with a dominant hole-mediated thermotransport. Upon comparing the red curves in figures 4.3a and 4.3b, it becomes evident that a minus sign should be applied. In figure 4.3b the measured thermovoltage is in good agreement with the calculated value, $V_{\text{th}} = -\frac{I_{\text{th}}}{G}$, from double lock-in measurements (see blue curve in figure 4.3b). There is a gate shift of 0.1 V between the two curves, which is a typical drift of the molecule caused by changes in its electrical environment due to gate ramping. This is not a problem

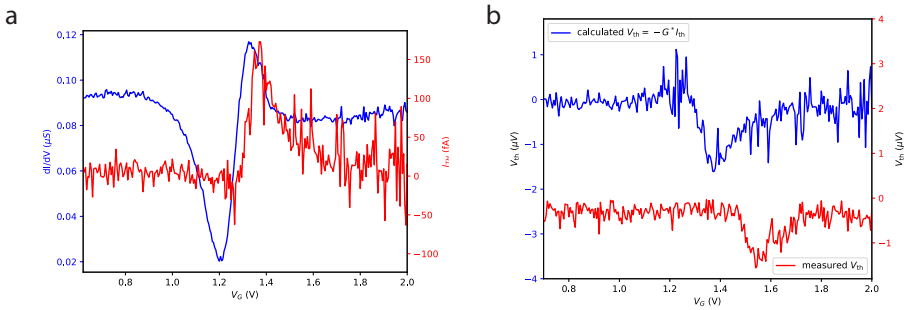

Figure 4.3: Thermocurrent and thermovoltage measured for a $[Zn(Tpy)_2](ClO_4)_2$ molecule. a. Differential conductance (blue) and thermocurrent (red) measured simultaneously with the double lock-in technique allow us to calculate the thermovoltage. b. Thermovoltage measured on the device under the same temperature gradient that is applied in (a) portrayed with the red color. The minus sign should be taken into account to get the same dependence as the thermocurrent measurements, $V_{th} = -\frac{I_{th}}{G}$. presented in (a). The calculated value is demonstrated with the blue color and shifted in vertical direction by 2 μV for clarity.

when comparing data but at the same time it highlights the necessity to measure thermocurrent and conductance simultaneously when using data to calculate the Seebeck coefficient.

4.2.3. JUXTAPOSITION OF AC AND DC THERMOCURRENT, -2$\sqrt{2}$ PREFACTOR.

In this subsection, we examine the thermocurrent measured with the double lock-in technique and compare it with the signal extracted from a direct measurement of I_{th}, where a constant temperature difference is applied across the junction. We refer to the latter as the DC measurement of thermocurrent. In the following we experimentally show that a prefactor of $-2\sqrt{2}$ for the AC thermocurrent should be applied in case of non-zero bias points in V_G-V space. As an example, the co-tunneling region will be considered below.

We performed several V-bias sweep measurements at constant $V_G = 0$ V on a Sme-2Os molecular junction that showed inelastic co-tunneling for the whole accessible gate range. First, DC measurements were performed as following: the I-V trace from 7 mV to -7 mV was recorded without current through the heater, and the retrace was taken at constant I_{heater}. Subtraction of the first curve from the second

directly provides the DC thermocurrent $I_{\mathrm{th}}(V) = I_{\mathrm{DC}}(V, \Delta T) - I_{\mathrm{DC}}(V, 0)$. Subsequently, another DC measurement was performed: for each V-bias point the heater was switched on and off and the two respective current values were determined. This measurement was in good agreement with the first one but lasted significantly longer (not presented in this thesis).

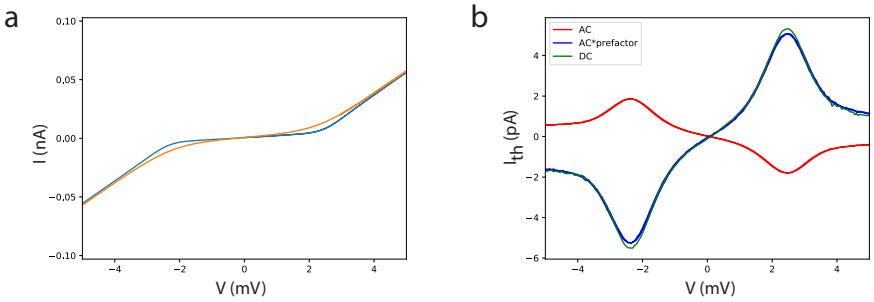

Figure 4.4: AC & DC thermocurent signals at finite bias. a. DC measurement of current as a function of applied bias voltage without heater (blue line) and with heater on (orange line). b. Thermocurrent as a function of bias voltage: AC response (red line), I_{th} extracted from (a) (green line), and calculated curve, with a prefactor of $-2\sqrt{2}$ (blue line).

Next, we repeated these DC measurements for heater values in the range between 0.06 and 1.47 mA. A representative measurement outcome is shown in figure 4.4a ($I_{\mathrm{heater}} = 0.1$ mA). Subsequently, we connected the lock-ins and performed the AC measurements for the same amplitudes. All AC measurements resulted in a lower thermocurrent and had an opposite sign (red curve in figure 4.4b). There was a good agreement between AC and DC data once the prefactor of $-2\sqrt{2}$ was used (green and blue lines in figure 4.4b). The coefficient of determination, $R^2 = 1 - \frac{\sum_{i=1}^{n}(I_{\mathrm{th}}^{\mathrm{DC}}(V_i) - (-2\sqrt{2}) * I_{\mathrm{th}}^{\mathrm{AC}}(V_i))^2}{\sum_{i=1}^{n}(I_{\mathrm{th}}^{\mathrm{DC}}(V_i) - \overline{I_{\mathrm{th}}^{\mathrm{DC}}})^2}$, where $\overline{I_{\mathrm{th}}^{\mathrm{DC}}}$ is the mean value of $I_{\mathrm{th}}^{\mathrm{DC}}(V)$, remained above 0.98 for the measurements.

4.3. DOUBLE LOCK-IN TECHNIQUE APPLICATION: RESULTS AND DISCUSSION

Electrical current through the heater, bias voltage and gate voltage can be seen as tuning knobs to drive the system through different regimes. Further on, we take a look into them separately to correctly interpret the measured values and to match lock-in readings with the

physical quantities such as Seebeck coefficient, Power Factor (*PF* that characterises the heat-to-energy conversion efficiency [31], $PF = S^2G$), etc.

Linear regime. The most simple case to analyse is the linear regime (LR). It is characterized by both the temperature difference ΔT and the bias voltage V being much smaller than the thermal energy of the system, specifically $\Delta T \ll \bar{T}$ and $eV \ll k_B\bar{T}$, where $\bar{T}$ is the base temperature of the environment near the nano object during the experiment, e is the electrical charge, and k_B is the Boltzmann constant. Note that $\bar{T}$ is in general different from the base temperature, T_{base}, and the temperature on the cold side, T_C ($T_{base} \leq T_C \leq \bar{T}$), which can be particularly relevant for large ΔT. Within this regime, the Onsager relations can be applied [7], allowing electrical current and heat flow to be expressed as:

$$\begin{aligned} I &= GV + SG\Delta T, \\ J &= G\Pi V + (K + GS\Pi)\Delta T, \end{aligned} \tag{4.2}$$

where S and Π are the Seebeck and Peltier coefficients, respectively, and K denotes the thermal conductance, comprised by electron K_{el} and phonon K_{ph} components (the second one can be neglected at low temperatures). These parameters together with G are sufficient to describe the thermoelectric dynamics of the system in this regime, simplifying the further analysis significantly. The double lock-in technique allows to directly obtain G^*, which equals G in the linear regime, and the thermal current at $2\omega_2$ ($I_{th} = SG\Delta T$), so that S can be determined.

The results of a typical measurement at zero bias at a small constant temperature gradient on a gold grain quantum dot (QD) are depicted in figure 4.5a. By sweeping the gate voltage, the position of the energy levels of the QD are tuned. A conductance peak occurs once the energy level is in resonance with the leads; this point also coincides with zero thermocurrent. This behavior aligns with the schematics of the chemical potential diagrams in figure 4.5a. When the resonant energy level of the QD is above the chemical potentials of the leads, the thermocurrent is primarily driven by electrons moving from the hot to the cold side, resulting in a negative thermocurrent detected by the amperometer. Conversely, when the molecule's energy level is below the chemical potentials of the leads, electrons from the cold side move to the hot side, generating a thermocurrent with a positive sign. This condition corresponds to hole-mediated transport, characterized by the QD level being predominantly occupied and the charge carriers entering the system being effectively holes. Thus, the thermocurrent sign holds important information about the transport carriers in the system.

In this linear regime, it is possible to extract the thermovoltage $V_{th} = -I_{th}/G$ and by knowing the temperature gradient (see the paragraph

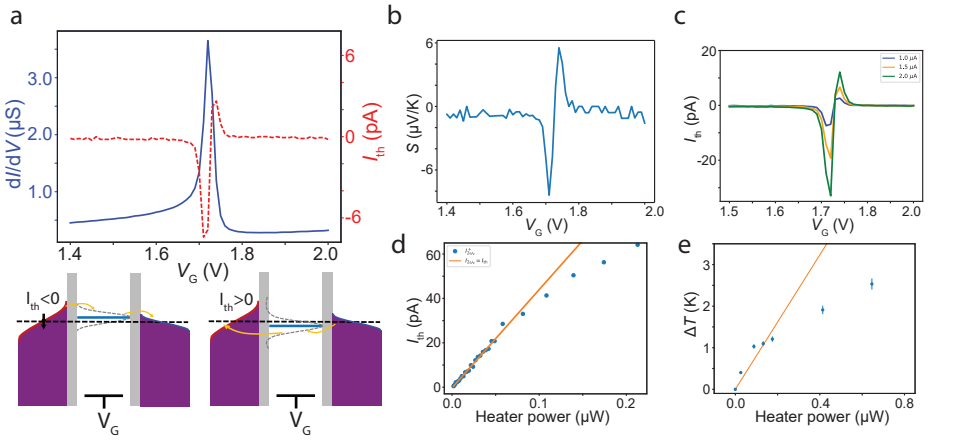

Figure 4.5: Zero-bias measurements with the double lock-in technique on a gold quantum dot (QD). a. Differential conductance (blue) and thermocurrent as a function of gate voltage V_G. The differential conductance shows a pronounced peak at $V_G = 1.72$ V, once the energy level of the QD is in resonance with the leads; meanwhile, the thermocurrent changes its sign at this point. The different signs correspond to different types of carriers that are responsible for the transport with electron transport for $I_{th} < 0$, and hole transport for $I_{th} > 0$ (see schematic diagram explaining the process below). b. Seebeck coefficient as a function of gate voltage calculated from the data measured in (a). c. Thermocurrent with gate voltage for different heater currents (see inset for color clarification). d. Maximum of positive thermocurrent as a function of power dissipated in the heater. The double lock-in technique can be applied when $I_{th} = I_{2\omega_2}$ (below 1 μW for this device). e. Temperature difference over the QD as a function of heater power.

on thermometry in appendix) the Seebeck coefficient, depicted in figure 4.5b. Further on, the system's Power Factor ($S^2G = 5.3 * 10^{-4} \frac{k_B^2}{h}$) and the dimensionless figure of merit ($ZT = S^2GT/K$) can be estimated. These metrics are useful for comparing the performance of different nano-scale objects as heat-to-energy harvesters. It is essential to perform such measurements for different molecules in order to achieve the best values and consequently realize particle exchange heat engine [32] that would meet theoretical expectations [18, 33, 34] and would operate close to the Carnot limit. Recent scientific publications [22, 35] reveal values that are still much smaller then

theoretical limit for the Power Factor for a non-interacting single level which equals $0.46 \times \frac{k_B^2}{h}$ [36], where h is Planck constant.

To determine the applicability of formula 4.1 in describing the current, it is important to understand the range for the values of temperature gradient and voltage bias that can be applied to the system. The accuracy of these formulas under conditions of non-negligible temperatures and voltages has been examined through simulations of microscopic models [37–39]. These studies provide a practical definition of small perturbations, suggesting that $\Delta T \lesssim \bar{T}$ and $eV \lesssim k_b \bar{T}$ are adequate for ensuring less than 5% error in the current predictions. However, we recommend to determine the range during the experiment by sweeping the heater current and checking the thermocurrent response and change of the lead temperature. Both measurements and interpretation of the results are less complex in linear regime.

Figure 4.5c illustrates the response of the thermosignal to various heater powers, showing that while the zero-value point remains constant (position of energy level is not influenced by the heater), the amplitude of the thermopower signal varies. Figure 4.5d depicts the evolution of the I_{th}^{+} (positive maximum of thermocurrent) at a fixed gate voltage across a range of heater powers. It is noted that the linear temperature regime assumption is not valid for all heater powers, and there is a point where the dependence stops being linear, enabling the estimation of $P_{h,\mathrm{max1}}$. This point serves as an cut-off value below which the linear regime assumption is valid.

Partially linear voltage regime. It is useful to perform thermometry during the measurements (see figure 4.5e) and to find the point where the system is in the partially linear regime (PLR) experimentally. The PLR occurs when one of the two external parameters (temperature difference or bias voltage) meets the linearity condition, while the other does not. In this context, we consider $\Delta T \not\ll \bar{T}$, and $eV \ll \mathrm{k_B}\bar{T}$. Here, thermoelectric parameters depend on temperature, and the non-linear thermocurrent can be represented as $I_{\mathrm{th}} = G(T)S(T)\Delta T$. In this regime, an engineering figure of merit, $(ZT)_{\mathrm{eng}}$, can be utilized for efficiency indication [39]. Note, that it can require integrating thermoelectric parameters over the temperature range from T_C to T_H, which practically means measuring the conductance and the thermocurrent at several base temperatures, thereby complicating the measurement. It is worth discussing what temperature should be used in this case. The temperature of the nanoobject is not defined, but the temperature of its surroundings can be estimated as $\bar{T} = \frac{T_H + T_C}{2}$, where T_H and T_C are the temperatures on the heater side and on the opposite side, respectively. Figure 4.5e details the calibration of temperatures within the system, measured using SNS thermometry (see appendix). Figure 4.5e summarizes how ΔT depends on heater power.This figure shows that the double lock-in

method remains applicable when $\Delta T \sim \bar{T}$. However, in this regime, it is advisable to use the engineering figure during the characterization of efficiency, and thermoelectric measurements should be conducted at different temperatures.

Partially linear temperature regime. A general method to electrically characterize a nanoobject is to measure the stability diagram in which differential conductance or current is plotted as a function of gate and bias voltage. With the double lock-in method the thermocurrent signal can be obtained simultaneously, and in case of a small temperature gradient across the nanoobject the partially linear temperature regime (PLTR), i.e. $\Delta T \ll \bar{T}, eV \not\ll k_B\bar{T}$, can be accessed. It is important to understand the meaning of the signal and correctly estimate the Seebeck coefficient and Power Factor in this regime to avoid further misinterpretations (reported values [40] in the PLTR regime are usually much higher than at zero bias, and are calculated in the same way as done at zero-bias which is in general not correct).

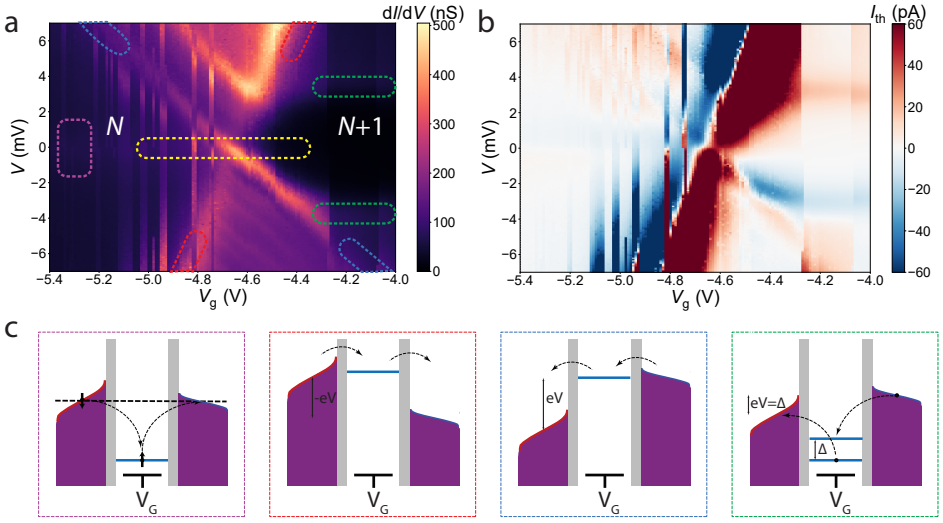

Figure 4.6: Stability diagram of a Sme-2Os molecule. a-c. Differential conductance (a) and thermocurrent (b) as a function of the gate and bias voltage measured simultaneously with the double lock-in technique at 1.7 K. Different regions at the stability diagram are highlighted with colors: zero-bias regime (yellow), Kondo region (purple), co-tunneling region (green), high-bias edges of Coloumb diamonds (red for source lead in resonance with molecular energy level, and blue for the situation when drain is in resonance), and their schematic description is described in (c).

A typical measurement in the PLTR regime is illustrated in figure 4.6. In this case the system under investigation is a biradical organic molecule abriviated with Sme-2Os. The differential conductance stability map indicates the presence of a charge degeneracy point at $V_G = -4.7$ V, where the system changes the amount of electrons from N to $N+1$ with pronounced edges of Coulomb diamonds that appear once the energy level of the molecule is in resonance with the Fermi level of one of the leads (see figure 4.6c). In the N state a zero-bias Kondo peak is present. It arises from the interaction between the spin on the molecule and the Kondo cloud in the leads. In the $N+1$ state inelastic co-tunneling is present as a result of a change from the singlet ground state to the triplet excited state (indicated by the green dashed region in figure 4.6a).

As can be seen from figure 4.6b, the thermocurrent changes its amplitude and sign in different parts of the stability diagram and contains information about the features mentioned above. I_{th} changes from a minimum value of -187 to 575 pA. The figure can be split in different regions of interest: zero-bias region (yellow), Kondo region (purple), inelastic co-tunneling region (green) and edges of Coulomb diamonds at higher voltage related to the source (red) and drain (blue) resonances with the molecular energy level.

Before undertaking a comprehensive review of the regimes, it is worth to define what is the effective temperature difference, ΔT_{eff}, that governs the thermocurrents across different sections of the stability diagram. In the yellow region, where $|V| \lesssim k_B\bar{T}$, the effective temperature gradient is $\Delta T_{eff} = \Delta T = T_H - T_C$. In the higher voltage range, the red and blue regions in the stability diagram, the thermocurrent is dictated by the temperature of the lead that is in resonance with the molecular level. The influence of the other lead is negligible because of minimal overlap between the transmission function of the molecular level with the density of states of the other lead (see the two middle panels in figure 4.6c). Thus, the red region, defined by $e|V| \gg k_B\bar{T}$ and $\mu(N) \approx \mu_H$, should be characterized with $\Delta T_{eff} = T_H - T_{base}$, and blue one, with $e|V| \gg k_B\bar{T}$ and $\mu(N) \approx \mu_C$, has $\Delta T_{eff} = T_C - T_{base}$.

Another feature that should be taken into account is the fact that the heater not only creates a temperature difference ΔT but also raises the overall temperature $\Delta\bar{T} = (T_H + T_C)/2 - T_{base}$ in the close vicinity to the molecule. If in this situation G depends on the temperature in the range $[T_{base}, \Delta\bar{T}]$, then in the non-zero bias case the double lock-in method picks up an extra signal, $I_{\Delta\bar{T}}$, which also has a frequency of $2\omega_2$. In the PLTR this term can be approximated as a first-order temperature perturbation of the conductance:

$$I_{\Delta\bar{T}} = \left.\frac{\partial G(V,T)}{\partial T}\right|_{T_{base}} V\Delta\bar{T}. \tag{4.3}$$

The contribution of $I_{\Delta\bar{T}}$ is negligible at zero bias due to its proportionality to the applied bias voltage. However, at finite bias, this term can significantly impact the signal, and one can expend the thermocurrent signal to first order, giving:

$$I_{\mathrm{th}}(V, \Delta T, \Delta\bar{T}) = G(V)S(V)\Delta T + < \frac{\partial G(V,T)}{\partial T} > \Big|_{T_{\mathrm{base}},\bar{T}} V\Delta\bar{T}, \tag{4.4}$$

where the average value of $\frac{\partial G(V,T)}{\partial T}$ over the range $[T_{\mathrm{base}}, \bar{T}]$ is used. Here, $S(V)$ is an effective Seebeck coefficient at constant voltage that still can be used to estimate the engineering Power Factor.

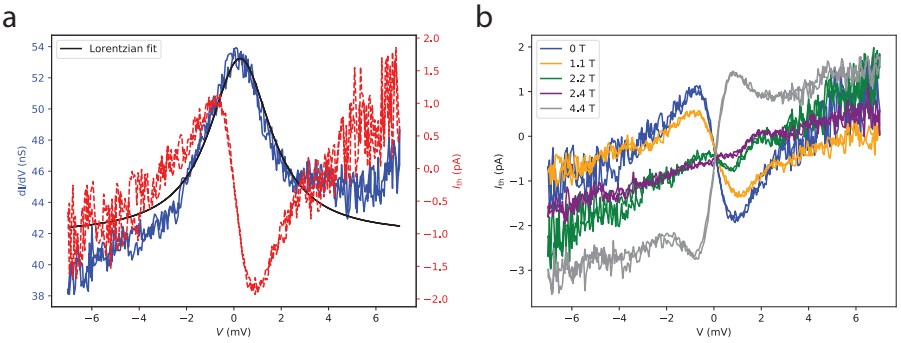

Figure 4.7: Kondo effect. a. AC differential conductance (blue) of the Kondo peak fitted with a Lorentzian function (black line) and thermocurrent (red) as a function of bias voltage. b. Thermocurrent as a function of bias voltage at different magnetic fields (see colors in inset for clarification).

In figure 4.7a the differential conductance and $I_{2\omega_2}$ for the purple region at $V_G = -5.6$ V, is depicted. This region exhibits a Kondo resonance. A pronounced zero-bias peak with $G = 54$ nS with a half width at half maximum (HWHM) of 1.59 ± 0.08 mV can be seen. At the same time, the thermocurrent signal changes its sign at $V = 0$ V and reaches its minimum of -1.93 pA at 0.9 mV and its maximum of 1.12 pA at -0.8 mV. Observation of a negative thermocurrent at positive bias voltage immediately rises the question of potentially creating a particle exchange heat engine at constant bias. To achieve this, it is possible to connect a load resistance (R_{load}) to the system in series (here the useful work is done), and perform the measurements. After performing the temperature dependence measurement it is possible to extract the first term of equation 4.4. Then, by calculating the heat flow J through the system, it is possible to estimate the engineering efficiency of this

heat engine:

$$\eta_{\text{eng}}(V) = \frac{(G(V)S(V)\Delta T)^2 R_{\text{load}}}{J + I_{\text{DC}}^2(R_{\text{load}} + 1/G(V))}, \tag{4.5}$$

where we also take into account the work done by the source, $I_{\text{DC}}^2(R_{\text{load}} + 1/G(V))$.

In the Kondo region the double lock-in method also plays a significant role in extracting the Kondo temperature. It has been demonstrated previously [23] that the derivative of the thermocurrent with respect to voltage bias at 0 V is a universal function of the ratio between magnetic field and Kondo temperature. By performing a magnetic field (B) sweep it is difficult to extract the Zeeman splitting point from a differential conductance measurement. Meanwhile, I_{th} changes the sign of the slope at zero-bias at a critical field, B_{c}, from which T_{K} can be extracted. Figure 4.7b illustrates the dependence of the thermocurrent as a function of magnetic field. The change of the slope at zero-bias is seen for the purple curve taken at $B = 2.4$ T yielding $T_{\text{K}} = 7$ K (estimated using $B_{\text{c}} \approx 0.5 k_{\text{B}} T_{\text{K}} g \mu_{\text{B}}$, where μ_{B} is the Bohr magneton constant and $g = 2$). At the same time, we can estimate T_{K} from the HWHM using the formula 2.12 which yields a temperature, that is in a good agreement with the previous estimation.

In the green region in figure 4.6b it is recommended to perform temperature measurements of differential conductance to check if there is a contribution to the thermocurrent from $\frac{\partial G(V,T)}{\partial T}$. Once such a measurement is done, it is possible to utilize formula 4.4 and extract Seebeck coefficient at constant voltage. This value could potentially be a hallmark to characterize the ground – first excited state transition. Here, the ground state of the molecule in the $N+1$ state would either be a singlet or triplet with the opposite being the excited state. This could be clarified with a magnetic field sweep, mapping the evolution of the energy and the possible splitting of the IETS. However, in case $gS\mu_{\text{B}}B \lesssim 3.5 \text{k}_{\text{B}} T$, the temperature broadening of the peaks smoothens the peaks and then it is difficult to draw clear conclusions about the spin states involved. We speculate that the Seebeck coefficient extracted above should in principle contain information about the entropy. Thus, it should be different for a singlet-triplet or a triplet-singlet transition. This statement requires further experimental and theoretical verification.

Non-Linear regime. Finally, the non-linear regime (NR) arises when $\Delta T \not\ll \bar{T}$ and $eV \not\ll \text{k}_{\text{B}}\bar{T}$. In this case linear expressions for I and J are not valid, and it is impossible to use only G, S, Π, K to describe the system dynamics. These quantities become functions of both the temperature and voltage, and the non-linear figure of merit $Z(V,T)T$ can no longer be used as an efficiency metric. Despite attempts to derive expressions that align with complex numerical simulations, success in obtaining them remains elusive. A possible approach is to utilize the engineering

power factor (PF_{eng}) and efficiency (η_{eng}) proposed by Kim et al., which have shown reliable results in several examples [39]. In the case of the realization of a heat engine we recommend to directly measure the power output at the load resistance connected to the system under investigation. Also, it is more practical to use an engineering efficiency (ratio between useful work to energy dissipated in the heater) instead of the real efficiency. Extraction of the latter seems elusive, as it is both theoretically and experimentally challenging to estimate the heat flow through the system. Aligning results with microscopic models presents difficulties, as standard methods such as the rate equation or scattering theory rely on simplifying assumptions and are characterized by numerous free parameters. Also, one should pay attention to the source that performs the useful work. It should be done by the thermovoltage, but not by the voltage source. To make sure that this is the case, one should check that the direction of thermocurrent is opposite to the bias voltage.

4.4. CONCLUSION

To summarise, in this chapter we provided a detailed explanation of the double lock-in method that allows to simultaneously preform differential conductance and thermocurrent measurements. It is essential to understand the boundaries of this technique and correctly interpret the signal in different voltage and temperature regimes. In this work, we described the most common features that appear during the measurements of a single molecule and discussed the physical meaning of the measured thermocurrent. For application purposes, we recommend to stay within the linear regime in order to extract the correct Seebeck coefficient and Power Factor in the hunt for an ideal molecular energy harvester. It is important to apply a prefactor to the measured data to get the correct value. Thermocurrent data at constant bias need further theoretical and experimental analysis. Both theory and experiment should go hand in hand to search for universalities in I_{th} that would provide information on physical quantities that can not be extracted simply from transport measurements.

4.5. APPENDIX

4.5.1. TEMPERATURE CALIBRATION.

In this subsection, we will focus on extracting the temperature difference across the molecular junction once the power is applied to the heater. Accurate temperature calibration is essential for extracting thermoelectric parameters from measured currents. This can be

achieved either by directly measuring temperatures with methods reliable within the target range or through microscopic modeling, which relies on assumptions and can therefore include numerous parameters. In our device, shown in figure 4.1, we used superconductor-normal metal-superconductor (SNS) thermometers [41] (see also chapter 3) to determine the contact temperatures between 1.7 and 5.2 K. The calibration also confirms that ΔT scales linearly with P_{heater} at low heater currents thereby providing information where the double lock-in technique can be used, and where AC measurements accurately represent the thermocurrent I_{th}.

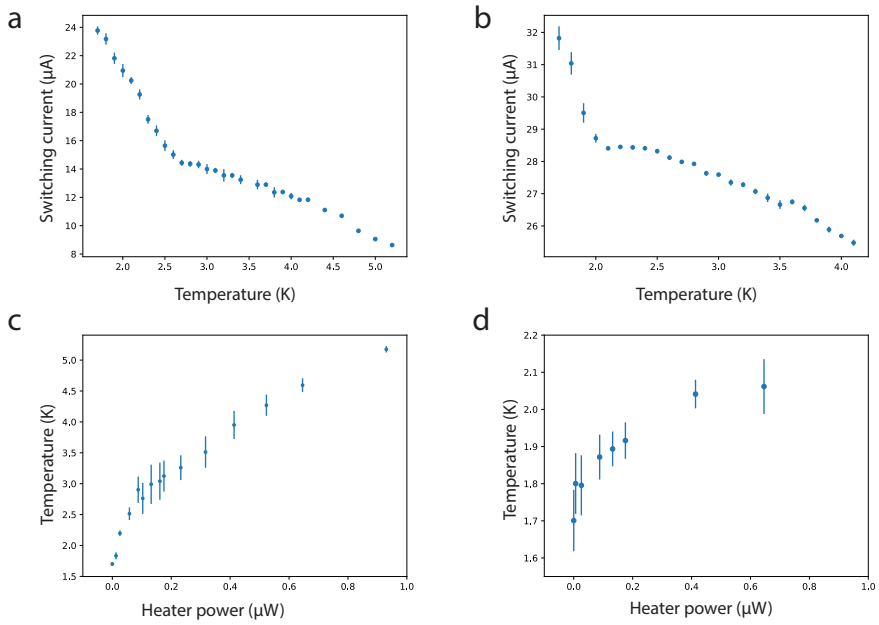

Figure 4.8: SNS thermometry. a-b. Temperature dependence of the switching current for the SNS thermometer near the heater (a), hot side, and for the thermometer on the opposite side (b), cold side. c-d. Temperature on the hot (c) and cold (d) sides as a function of heater power.

In particular, MoRe contacts connected to the gold bridge create two SNS junctions that are used as secondary thermometers on each side of the molecule. To calibrate them, we first record th switching current, I_{SW}, as a function of the base temperature. Representative data for one of the thermometers is shown in figure 4.8a. The switching current changes from 23.8 μA at 1.7 K to 8.6 μA at 5.2 K. The sensitivity of the thermometer, defined as $\frac{dI_{\text{SW}}}{dT}$, changes accordingly

from approximately 9.7 $\frac{\mu A}{K}$ in the lower temperature region to 2.5 $\frac{\mu A}{K}$ at higher temperatures. These values are much lower than the values reached at milli-Kelvin temperatures with the same junction design [41] and should be optimized to achieve the best performance in this temperature range. There is also a kink in the $I_{SW}(T)$ curve around 2.8 K, it increases the temperature measurement error in range between 2.8 K and 3.1 K.

The calibration curve for the second thermometer, the one on the cold side, is shown in figure 4.8b. Here, the switching current at 1.7 K is slightly higher than that of the first thermometer and reaches 31.8 μA. Similar to figure 4.8a, we observe two regions with different $\frac{dI_{SW}}{dT}$. In this case, the change occurs around 2.1 K. The difference in temperatures where the switch happens between the thermometers suggests that this phenomenon is not related to sample thermalization issues. The region below 2.1 K has a higher sensitivity of around 8.5 $\frac{\mu A}{K}$ but suffers from a larger switching current distribution width that leads to errors in the determination of I_{SW} in the order of 0.4 μA. In the second region, above 2.4 K, the switching current dependence exhibits an almost linear behavior with $\frac{dI_{SW}}{dT}$=1.8 μA. The highest error in the switching current determination is 0.1 μA.

Subsequently, we reduce the temperature to the minimum achievable base temperature of 1.7 K and measure the switching current for both thermometers as a function of power dissipated by the heater located in the closest vicinity to the first thermometer. This allows to determine the temperature on the hot and cold sides of the golden bridge. The results are illustrated in figure 4.8c and 4.8d. Both dependencies are probed up to P_{heater} =1.0 μW, which demonstrates the impact on temperature on both sides of the bridge. The hot side has a much stronger response to heating with its temperature rising up to 5.1 K. At the same time, the temperature on the cold side stays below 2 K for $P_{heater} < 0.65\ \mu W$.

Finally, we calculate the temperature gradient across the golden bridge, $\Delta T = T_{hot} - T_{cold}$, and estimate its error by $\delta\Delta T = \Delta T\sqrt{(\frac{\delta T_{hot}}{T_{hot}})^2 + (\frac{\delta T_{cold}}{T_{cold}})^2}$. Despite the small amount of data points, we conclude that the temperature gradient is linear for low heater current values, and deviates from this linear behavior when the heating power is increased above about 0.2 μW, as is illustrated in figure 4.9. The exact transition point can not be determined from this plot, but the figure shows that for ΔT gradients of the order of the T_{base} the double lock-in technique can still be used (orange line in figure 4.9). Strikingly, a similar ΔT was extracted when analyzing the dependence of thermocurrent amplitude as a function of applied heating power. Thus, when performing thermometry on a sample is not possible, I_{th} vs. I^2_{heater} can be a reasonable indication of the applicability of the AC-measurement technique, with the remark that linear thermoresponse is expected from the physical system under

investigation.

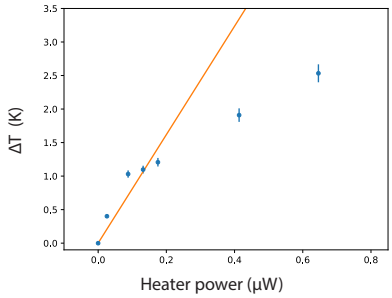

Figure 4.9: SNS thermometry. Temperature gradient across the gold bridge vs. heater power showing more or less linear relation for low P_{heater} values as indicated by the drawn orange line.

REFERENCES

[1] L. Anatychuk. “On the discovery of thermoelectricity by Volta”. *Journal of thermoelectricity* 2 (2004), pp. 5–10.

[2] T. J. Seebeck. “Ueber die magnetische Polarisation der Metalle und Erze durch Temperaturdifferenz”. *Annalen der Physik* 82.3 (1826), pp. 253–286.

[3] H. C. Ørsted. “Nouvelles expériences de M. Seebeck sur les actions électro-magnétiques”. *Annales de Chimie et de Physique*. Vol. 22. 1823, pp. 199–201.

[4] J. C. A. Peltier. *Nouvelles expériences sur la caloricité des courans électriques*. 1834.

[5] W. Thomson. “On a Mechanical Theory of Thermo-Electric Currents”. *Proceedings of the Royal Society of Edinburgh* 3 (1857), pp. 91–98.

[6] E. Altenkirch. “Über den Nutzeffekt der Thermosäule”. *Physikalische Zeitschrift* 10 (1909), pp. 560–580.

[7] L. Onsager. “Reciprocal Relations in Irreversible Processes. I.” *Phys. Rev.* 37 (4 Feb. 1931), pp. 405–426.

[8] H. B. Callen. “The Application of Onsager’s Reciprocal Relations to Thermoelectric, Thermomagnetic, and Galvanomagnetic Effects”. *Phys. Rev.* 73 (11 June 1948), pp. 1349–1358.

[9] M. Vedernikov and E. Iordanishvili. “A.F. Ioffe and origin of modern semiconductor thermoelectric energy conversion”. *Seventeenth International Conference on Thermoelectrics. Proceedings ICT98 (Cat. No.98TH8365)*. 1998, pp. 37–42.

[10] A. F. Ioffe, L. S. Stil’bans, E. K. Iordanishvili, T. S. Stavitskaya, A. Gelbtuch, and G. Vineyard. “Semiconductor Thermoelements and Thermoelectric Cooling”. *Physics Today* 12.5 (May 1959), pp. 42–42.

[11] J. Zhang, H. J. Liu, L. Cheng, J. Wei, J. H. Liang, D. D. Fan, P. H. Jiang, L. Sun, and J. Shi. “High thermoelectric performance can be achieved in black phosphorus”. *J. Mater. Chem. C* 4 (5 2016), pp. 991–998.

[12] H. J. Goldsmid. “Heat Conduction in Bismuth Telluride”. *Proceedings of the Physical Society* 72.1 (July 1958), p. 17.

[13] B. Abeles, D. S. Beers, G. D. Cody, and J. P. Dismukes. “Thermal Conductivity of Ge-Si Alloys at High Temperatures”. *Phys. Rev.* 125 (1 Jan. 1962), pp. 44–46.

[14] L. D. Hicks and M. S. Dresselhaus. “Thermoelectric figure of merit of a one-dimensional conductor”. *Phys. Rev. B* 47 (24 June 1993), pp. 16631–16634.

[15] L. D. Hicks and M. S. Dresselhaus. “Effect of quantum-well structures on the thermoelectric figure of merit”. *Phys. Rev. B* 47 (19 May 1993), pp. 12727–12731.

[16] J. P. Heremans, M. S. Dresselhaus, L. E. Bell, and D. T. Morelli. “When thermoelectrics reached the nanoscale”. *Nature Nanotechnology* 8.7 (July 2013), pp. 471–473.

[17] S. Park, H. Kang, and H. J. Yoon. “Structure–thermopower relationships in molecular thermoelectrics”. *J. Mater. Chem. A* 7 (24 2019), pp. 14419–14446.

[18] J. Koch, F. von Oppen, Y. Oreg, and E. Sela. “Thermopower of single-molecule devices”. *Phys. Rev. B* 70 (19 Nov. 2004), p. 195107.

[19] C. J. Lambert, H. Sadeghi, and Q. H. Al-Galiby. “Quantum-interference-enhanced thermoelectricity in single molecules and molecular films”. *Comptes Rendus Physique* 17.10 (2016). Mesoscopic thermoelectric phenomena / Phénomènes thermoélectriques mésoscopiques, pp. 1084–1095.

[20] J. R. Widawsky, P. Darancet, J. B. Neaton, and L. Venkataraman. “Simultaneous determination of conductance and thermopower of single molecule junctions”. *Nano Lett.* 12.1 (Jan. 2012), pp. 354–358.

[21] S. Park, S. Kang, and H. J. Yoon. “Power Factor of One Molecule Thick Films and Length Dependence”. *ACS Central Science* 5.12 (Dec. 2019), pp. 1975–1982.

[22] P. Gehring, J. K. Sowa, C. Hsu, J. de Bruijckere, M. van der Star, J. J. Le Roy, L. Bogani, E. M. Gauger, and H. S. J. van der Zant. “Complete mapping of the thermoelectric properties of a single molecule”. *Nature Nanotechnology* 16.4 (Apr. 2021), pp. 426–430.

[23] C. Hsu, T. A. Costi, D. Vogel, C. Wegeberg, M. Mayor, H. S. J. van der Zant, and P. Gehring. “Magnetic-Field Universality of the Kondo Effect Revealed by Thermocurrent Spectroscopy”. *Phys. Rev. Lett.* 128 (14 Apr. 2022), p. 147701.

[24] P. Gehring, J. K. Sowa, C. Hsu, J. de Bruijckere, M. van der Star, J. J. Le Roy, L. Bogani, E. M. Gauger, and H. S. J. van der Zant. “Complete mapping of the thermoelectric properties of a single molecule”. *Nature Nanotechnology* 16.4 (Apr. 2021), pp. 426–430.

[25] P. Gehring, M. van der Star, C. Evangeli, J. J. Le Roy, L. Bogani, O. V. Kolosov, and H. S. J. van der Zant. “Efficient heating of single-molecule junctions for thermoelectric studies at cryogenic temperatures”. *Applied Physics Letters* 115.7 (Aug. 2019), p. 073103.

[26] C. Hsu, T. A. Costi, D. Vogel, C. Wegeberg, M. Mayor, H. S. J. van der Zant, and P. Gehring. “Magnetic-Field Universality of the Kondo Effect Revealed by Thermocurrent Spectroscopy”. *Phys. Rev. Lett.* 128 (14 Apr. 2022), p. 147701.

[27] A. Harzheim, J. K. Sowa, J. L. Swett, G. A. D. Briggs, J. A. Mol, and P. Gehring. “Role of metallic leads and electronic degeneracies in thermoelectric power generation in quantum dots”. *Phys. Rev. Research* 2 (1 Feb. 2020), p. 013140.

[28] *QT designed instrumentation: IVVI rack*. url: https://qtwork.tudelft.nl/~schouten/ivvi/index-ivvi.htm.

[29] E. Burzurí, Y. Yamamoto, M. Warnock, X. Zhong, K. Park, A. Cornia, and H. S. J. van der Zant. “Franck-Condon Blockade in a Single-Molecule Transistor”. *Nano Letters* 14.6 (June 2014), pp. 3191–3196.

[30] G. Luo and K. Park. “Magnetic-anisotropy-induced spin blockade in a single-molecule transistor”. *Phys. Rev. B* 94 (17 Nov. 2016), p. 174412.

[31] K. Behnia. “Fundamentals of Thermoelectricity”. *Oxford University Press.* (2015).

[32] T. Humphrey and H. Linke. “Quantum, cyclic, and particle-exchange heat engines”. *Physica E: Low-dimensional Systems and Nanostructures* 29.1 (2005). Frontiers of Quantum, pp. 390–398.

[33] C. J. Lambert, H. Sadeghi, and Q. H. Al-Galiby. “Quantum-interference-enhanced thermoelectricity in single molecules and molecular films”. *Comptes Rendus. Physique* 17.10 (2016), pp. 1084–1095.

[34] P. Murphy, S. Mukerjee, and J. Moore. “Optimal thermoelectric figure of merit of a molecular junction”. *Phys. Rev. B* 78 (16 Oct. 2008), p. 161406.

[35] A. K. Ismael, L. Rincón-García, C. Evangeli, P. Dallas, T. Alotaibi, A. A. Al-Jobory, G. Rubio-Bollinger, K. Porfyrakis, N. Agraït, and C. J. Lambert. “Exploring seebeck-coefficient fluctuations in endohedral-fullerene, single-molecule junctions”. *Nanoscale Horiz.* 7 (6 2022), pp. 616–625.

[36] P. Gehring, A. Harzheim, J. Spièce, Y. Sheng, G. Rogers, C. Evangeli, A. Mishra, B. J. Robinson, K. Porfyrakis, J. H. Warner, O. V. Kolosov, G. A. D. Briggs, and J. A. Mol. “Field-Effect Control of Graphene–Fullerene Thermoelectric Nanodevices”. *Nano Letters* 17.11 (Nov. 2017), pp. 7055–7061.

[37] J. Azema, P. Lombardo, and A.-M. Daré. “Conditions for requiring nonlinear thermoelectric transport theory in nanodevices”. *Phys. Rev. B* 90 (20 Nov. 2014), p. 205437.

[38] G. Benenti, G. Casati, K. Saito, and R. S. Whitney. “Fundamental aspects of steady-state conversion of heat to work at the nanoscale”. *Physics Reports* 694 (June 2017), pp. 1–124. issn: 0370-1573.

[39] H. S. Kim, W. Liu, G. Chen, C.-W. Chu, and Z. Ren. “Relationship between thermoelectric figure of merit and energy conversion efficiency”. *Proc. Natl. Acad. Sci. U. S. A.* 112.27 (July 2015), pp. 8205–8210.

[40] P. Gehring, J. K. Sowa, C. Hsu, J. de Bruijckere, M. van der Star, J. J. Le Roy, L. Bogani, E. M. Gauger, and H. S. J. van der Zant. “Complete mapping of the thermoelectric properties of a single molecule”. *Nature Nanotechnology* 16.4 (Apr. 2021), pp. 426–430.

[41] S. Volosheniuk, D. Bouwmeester, C. Hsu, H. S. J. van der Zant, and P. Gehring. “Implementation of SNS thermometers into molecular devices for cryogenic thermoelectric experiments”. *Applied Physics Letters* 122.10 (Mar. 2023), p. 103501.

5

ENHANCING THERMOELECTRIC EFFICIENCY IN A MOLECULAR HEAT ENGINE UTILIZING YU-SHIBA-RUSINOV BOUND STATES

The interaction between magnetic impurities and superconductors leads to fascinating phenomena resulting from the competition between Kondo screening and Cooper pair formation. For example, individual magnetic impurities can form states within the superconducting gap, called Yu-Shiba-Rusinov (YSR) bound states, that create sharp features in the density of states. Here, we employ thermocurrent spectroscopy to experimentally study the thermoelectric properties of a neutral and stable all-organic radical molecule coupled to proximity induced superconducting break-junction electrodes at milliKelvin temperatures. We find that the sharp YSR features also result in a strong enhancement of the thermoelectric response. By driving the molecular heat engine through a phase transition from a Kondo state into the YSR regime, we observe a five-fold increase in the thermoelectric power factor. This observation could pave the way for practical applications such as cryogenic waste heat recovery and efficient spot-cooling for future quantum computing architectures.

5.1. INTRODUCTION

Quantum systems coupled to superconductors offer a rich landscape of fundamental insights and potential applications in electronics and quantum computing. In recent years, multiple extensive studies were performed on nanotubes [1–3], nanowires [4–7], semiconducting quantum dots [8], molecules [9–12], atoms [13, 14] and topological insulators [15] directly linked to a superconductor. A variety of physical phenomena including Andreev reflections [16], multiple Andreev reflection [17], and Cooper pair splitting [18, 19] have been studied under different conditions. Special emphasis has been placed on examining the interplay between a superconductor and a magnetic moment on a quantum dot. This interplay is similar to a normal metal-impurity connection, where electrons in the metal actively screen the impurity, thereby giving rise to the Kondo effect [20]. In case of a coupled superconductor-quantum dot system, superconducting phenomena compete with Kondo screening. This competition can reveal itself through the formation of Yu-Shiba-Rusinov (YSR) bound states induced inside the superconductor gap [21–23]. Lately, YSR states have gained interest due to their potential to form topological bands that support non-Abelian Majorana modes, as indicated in several studies [24–27]. This allows potential realisation of topological superconductivity and presents a good platform for developing a quantum computer.

So far, the studies exploring YSR were performed mostly using the scanning tunnelling spectroscopy (STM) technique [28–30], primarily focused on magnetic atoms/molecules coupled to superconducting substrates. The use of STM spectroscopy allowed examination of the YSR state hybridization[31, 32] and identification of the different subgap excitations. However, STM has limitations in tuning the energy level of the investigated structure without changing the coupling rates, which could be surpassed by using a 3-terminal device. This approach allows exploration of the phase diagram in a more controllable manner. However, it requires complicated device fabrication, and as a consequence there are limited reports on YSR in molecular devices[11, 12]. In particular, Island *et al.*[12] investigated all-organic radical molecules in break junction devices with proximity-induced leads that behaved as a spin 1/2 system but did not vary the number of electrons on the molecule by gate.

In this chapter, we explore if sharp features in the density of states created by YSR bound states can serve as efficient energy filters to enhance the performance of a molecular heat engine. To this end, we measured a diradical nitronyl nitroxide compound (NNDR) molecule in a three-terminal device with proximity-induced superconducting leads. The subject of study behaves as a spin-1/2 system with a large charging energy. The induced superconductivity leads to the existence of in-gap

bound states. We were able to tune the system from a magnetic doublet ground state to a Kondo singlet by applying an external magnetic field and to a BCS-like singlet by changing the number of electrons on the molecule. We find that this phase transition enhances the thermoelectric power factor – a quantity proportional to the efficiency of the molecular particle exchange heat engines – by a factor of five.

5.2. MAIN

To investigate the performance of the molecular particle exchange heat engine we measure its electrical and thermoelectric properties at the same time, and at millikelvin temperatures, by using our recently developed device architecture [33, 34] whose working principle is shown in figure 5.1a. To this end, we electrically and thermally bias the junction simultaneously using an AC bias voltage V_{AC} at frequency ω_1 and an AC heater current $\tilde{I_H}$ at ω_2. At the source terminal we then demodulate the resulting AC current at ω_1 and $2\omega_2$ to access both the differential conductance $dI/dV = \tilde{I}_{AC}/V_B$ and the thermocurrent I_{th} (see chapter 4 for more details). For the molecule, an all-organic NNDR is used (figure 5.1c), which is a stable diradical. As will be shown later, by applying a negative gate voltage V_G, one electron can be removed from the molecule and it then acts as a spin-1/2 system.

The superconducting contacts used in this study serve a dual purpose as they are used as thermometers [34] and allow to induce proximity superconductivity in the molecular junction which leads to a competition between Kondo screening (characterized by the Kondo temperature, T_K) and superconducting pairing (characterized by the gap energy, $\Delta = (\Delta_1 + \Delta_2)/2$, where Δ_1 and Δ_2 are source and drain gap energy respectively). As depicted in figure 5.1a, the coupling of a spin-1/2 impurity (i.e., the molecule) to the superconducting electrodes yields the formation of bound states inside the superconducting gap as quasi-particles try to screen the spin of the impurity.

Figure 5.1d shows a detailed V_B and V_G map of dI/dV around the charge degeneracy point (CDP) recorded at a temperature of 62 mK. Two horizontal lines (highlighted by white dotted guidelines for the eye in figure 5.1d) indicate the voltage at which the coherence peaks of the source and the drain overlap, with their respective gap energies Δ_1 and Δ_2 (where $\Delta_1 + \Delta_2 \approx 130\ \mu$eV). When V_G is decreased below -2.8 V, the charge ground state changes from N to $N-1$ and the molecule is in the spin-1/2 state. As we find only one CDP in the accessible gate range, the charging energy, E_C, is much larger than the other relevant energy scales (Δ, T_K, Γ). Furthermore, two excited state lines at $V = 90\ \mu$V in the $N-1$ and at $V = 120\ \mu$V in the N charge state, respectively, merge near the charge degeneracy point. We attribute the bound state to a YSR state since the electronic coupling to the leads in our device

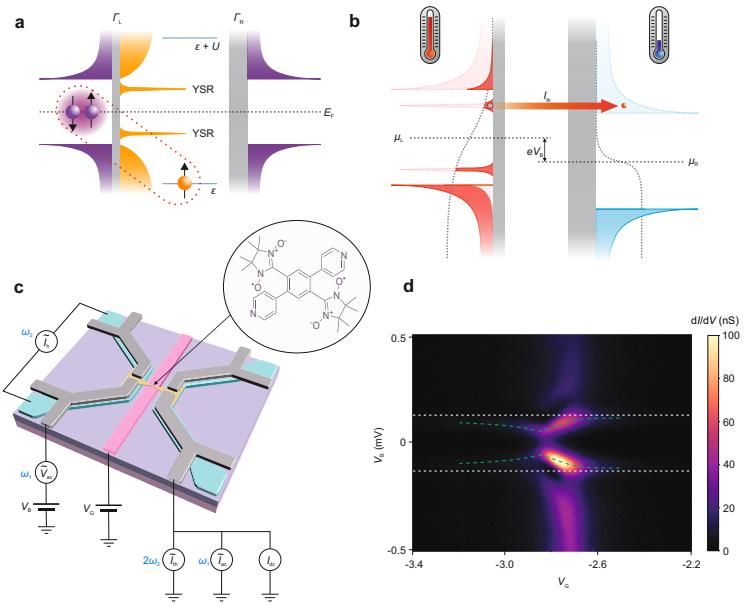

Figure 5.1: a. Sketch of the superconductor–quantum dot–superconductor (S-QD-S) system. An unpaired spin (orange sphere) residing on the molecule couples to a Cooper pair (purple spheres) inside the proximitized gold leads forming YSR bound states. b. Energy filtering via YSR states. A thermoelectric current I_{th} (red arrow) is flowing from the left (hot) side to the right (cold) side. The grey dotted lines depict the Fermi-Dirac distribution functions of the leads. c. Schematic of the thermopower device (back gate electrode (pink), heaters (light blue), golden bridge (yellow), superconducting contacts (grey)). The circuit diagram indicates which terminals are used to apply a gate voltage V_{G}, a DC bias voltage V_{B}, an AC bias voltage V_{AC} (ω_1) and an AC heater current I_{H} (ω_2), and which terminals are used to measure the DC I_{DC}, the AC I_{AC} (ω_1) and the thermocurrent I_{th} (ω_2). The insert shows the structure of the Nitronyl nitroxide diradical molecule (NNDR) which posseses two free spins on the oxygen atoms. d. Map of the differential conductance as a function of gate and bias voltage recorded at 62 mK. The bound states and the superconducting gap are highlighted by green and white dotted lines, respectively.

is highly asymmetric and $\Delta \gtrsim T_{\mathrm{K}}$ (see discussion of figure 5.2 below). The bound state undergoes a phase transition and changes its ground and excited state when increasing V_{G} and changing the charge state to

N (see discussion below). When going through this transition, the gap between bound states at positive and negative bias voltage decreases to 100 μeV – without a complete closing – which is the typical behaviour of a superconductor-quantum dot-superconductor system.

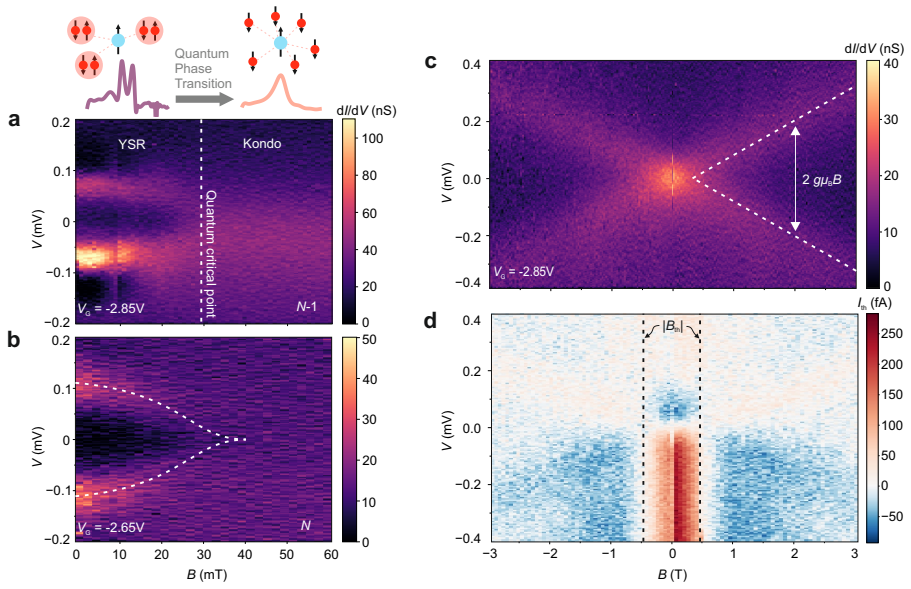

Figure 5.2: a, b. Differential conductance as a function of bias voltage and magnetic field at V_G=-2.85 V (a) and V_G=-2.65 V (b), respectively. c, d. Differential conductance (c) and thermocurrent (d) measured simultaneously as a function of bias voltage and magnetic field. The white dotted line indicates the Zeeman splitting of the Kondo resonance that occurs at a field of B_{th} 0.49 T (vertical black dotted lines).

An external out-of-plane magnetic field is expected to suppress Cooper pairing while favouring Kondo screening. In figure 5.2a the differential conductance as a function of bias voltage and magnetic field, at constant $V_G = -2.85$ V (left hand side of CDP, $N-1$) is depicted. Around zero magnetic field two differential conductance peaks which we attribute to the YSR states are visible: one at positive and one at negative bias. The voltage difference between the two peak positions stays almost constant up to a field of 10 mT and decreases – due to a change of the exchange coupling J and Δ with magnetic field – in the range between 10 mT and 30 mT, where the two peaks merge and form a single zero-bias peak. We attribute this zero-bias peak to a Kondo resonance. The continuous evolution between the two competing ground states of the system, which can be triggered at nearly zero temperature, is a hallmark

for quantum criticality[35]. For our molecular junction we observe that the quantum phase transition, driven by the external magnetic field, has a quantum critical point at ≈ 30 mT. Such quantum phase transition of the molecular quantum dot is absent in the N charge state ($V_G = -2.65$ V, see figure 5.2b): the in-gap bound states are closing with the magnetic field and disappear completely, indicating the transition of the proximitized gold electrodes to their normal state. Furthermore, the presence/absence of a Kondo resonance on the left/right hand side of the CDP, respectively, allows us to conclude that an unpaired electron resides on the molecule in the $N-1$ charge state.

In figure 5.2c and 5.2d we show the V_B and high B-field dependence of the differential conductance and thermocurrent measured simultaneously at $V_G = -2.85$ V. The Kondo resonance starts to Zeeman split at a magnetic field of $B_{th} = 0.49$ T. At the same time, the slope dI_{th}/dV of the thermocurrent at zero bias changes sign. It have been shown recently [36] that the magnetic field B_{th} at which this sign-change occurs, can be used to accurately extract the Kondo temperature $T_K = \frac{4}{3}\frac{\mu_B B_{th}}{k_B}$, where k_B is the Boltzmann constant and μ_B is the Bohr magneton. We find $T_K = 0.8 \pm 0.1$ K, which agrees well with the value estimated from the width of the Kondo peak (0.73 ± 0.04 K). Furthermore, from the Zeeman splitting at high magnetic fields (dotted line in figure 5.2c) we conclude that the junction is a spin-1/2 system with a g factor of 2 (see more details and Kondo analysis in appendix).

To further study how the quantum phase transition between the YSR and the Kondo regime impacts the thermoelectric properties of the single-molecule particle exchange heat engine, we simultaneously recorded maps of the bias and gate voltage dependent differential conductance and thermocurrent at a temperature of 150 mK for different applied magnetic fields between 0 and 60 mT (figure 5.3). For zero magnetic field, the differential conductance map (see figure 5.3a) resembles that shown in figure 5.1d; YSR bound states can be observed on the left/right hand side of the CDP, respectively. There is a small asymmetry between the differential conductance at positive and negative bias voltage with peak heights in the range of 2 to 62 nS for the upper arc and 2 to 108 nS for the lower one, which do not exceed the upper bound ($\frac{2e^2}{\hbar}$) of the theoretical expectations for YSR [37]. We note that the asymmetry in intensity of the in-gap excitations at positive/negative bias is changing as the gate voltage is increased (i.e., when changing the exchange coupling). Furthermore, the gate voltage can also be used to tune the phase transition from a doublet ground state on the left to an BCS-like singlet ground state on the right hand side. By applying a small perpendicular magnetic field, the proximity effect in the gold leads is suppressed. This leads to a broadening of the in-gap states (figure 5.3b) and to a quantum phase transition to the Kondo regime (figure 5.3d) at higher magnetic fields.

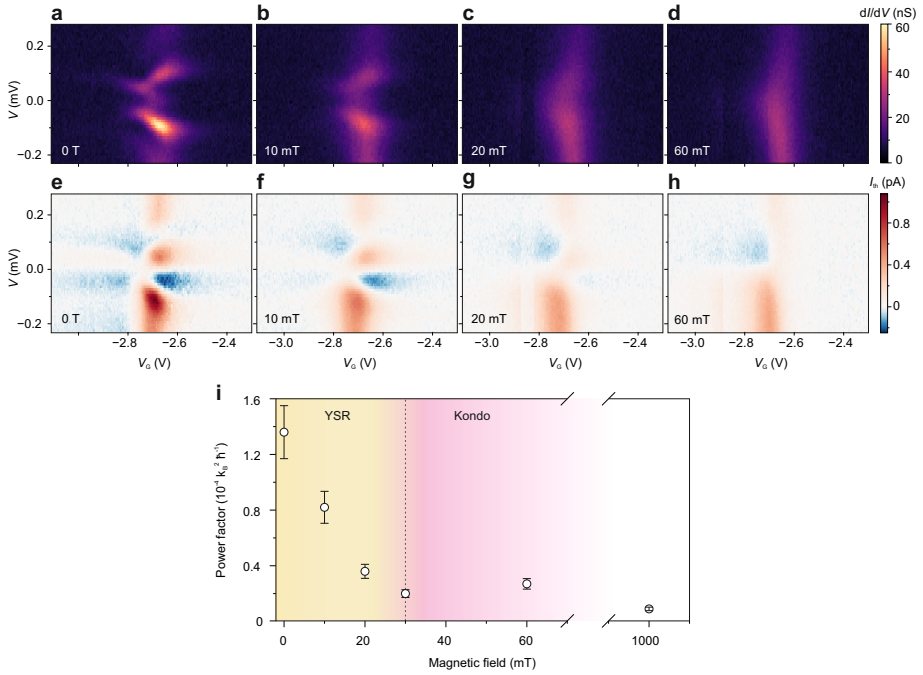

Figure 5.3: a-d. Maps of differential conductance and e-h, thermocurrent measured simultaneously as a function of bias and back gate voltage at different magnetic fields (0, 10, 20, and 60 mT, respectively). i. Thermoelectric power factor $S_0^2 G$ as a function of magnetic field.

The thermocurrent measured simultaneously with the differential conductance is shown in figures 5.3e-h. We observe that the bias-dependent I_{th} changes sign at bias voltages where the slope of the differential conductance, $\mathrm{d}^2I/\mathrm{d}V^2$, changes. The magnitude of I_{th} is proportional to $\mathrm{d}^2I/\mathrm{d}V^2$ and exhibits an enhancement near sharp features of the differential conductance (see figures 5.3e-h). At zero magnetic field, the maximum/minimum values of I_{th} are around 1 pA / -250 fA, respectively, and are at negative bias (bound state with negative energy with respect to the Fermi level). When a magnetic field is applied, the I_{th} maps change in shape and magnitude: while the bias dependent I_{th} changes sign 3 times in the YSR regime at $B = 0$ (figure 5.3e), it changes once in the Kondo regime (left-hand side of figure 5.3h). Furthermore, I_{th} decreases with increasing B and is reduced by a factor of ≈ 2.8 when going from 0 to 60 mT.

Using our cryogenic superconducting on-chip thermometers, we

extract a temperature drop of $\Delta T = 105 \pm 15$ mK across the molecule and calculate the differential thermoelectric conductivity (differential Seebeck coefficient) $dS = dV_{th}/dT \approx I_{th}/(dI/dV)/\Delta T$. We find a high $dS = 470\ \mu VK^{-1}$ at $V_G = -2.71$ V, $V = -135\ \mu$V and $B = 0$. The quantum phase transition at finite magnetic fields reduces this maximum value by almost 50% to $dS = 255\ \mu VK^{-1}$ at $V_G = -2.74$ V, $V = -200\ \mu$V at $B = 60$ mT. A similar enhancement by a factor of two originating from the presence of YSR states was found for the Seebeck coefficient, $S_0 = dV_{th}/dT|_{V=0}$, defined at zero bias voltage. We find $S_0 = 154\ \mu VK^{-1}$ at $B = 0$ and $S_0 = 45\ \mu VK^{-1}$ at 60 mT (i.e., in the Kondo regime). Furthermore, the corresponding power factor, $S_0^2 G$, at zero bias can be calculated (see Fig. 3i). This value serves as a valuable indicator for assessing the efficiency of heat-to-energy conversion [38]. Our calculation reveals a five-fold enhancement by the YSR states to $S_0^2 G = 1.36 \times 10^{-4} \frac{k_B^2}{\hbar}$, compared to $S_0^2 G = 0.27 \times 10^{-4} \frac{k_B^2}{\hbar}$ in the Kondo regime.

5

5.3. DISCUSSION

At small magnetic fields $B > 60$ mT, in the absence of superconductivity, gold is in its normal state and the system reveals the Kondo effect on the left-hand side of the CDP. From the Zeeman splitting (figure 5.2c), the temperature dependence of the width of the zero bias peak, and the shift of the CDP with magnetic field to more negative energies (see more details in the appendix), we deduce that the molecule hosts an unpaired electron ($S = 1/2$). The extracted Kondo temperature $k_B T_K \approx 70\ \mu$eV is greater than the typical values observed in GaAs quantum dots, yet aligns with the lower range associated with molecules[39]. Simultaneously, the tunnel coupling to the contacts exhibits notable asymmetry (from the Kondo analysis we extract a value of $\approx 1.2 \times 10^4$) that is frequently observed in electromigrated molecular junctions. Subsequently, the introduction of an additional electron to the system results in the disappearance of the zero-bias peak and changes the total spin of the molecule to zero (right-hand side of CDP).

When reducing B to zero, the gold undergoes a transition to proximity-induced superconductivity, resulting in a substantial reduction of the current within the bias window of the order of $\pm(\Delta_1 + \Delta_2)/e$. However, in-gap excited states remain which originate from the interaction between proximity-induced quasi-particles on the contacts and the spin on the molecule. The high asymmetrical tunnel coupling to the contacts excludes the possibility that the peaks originate from Andreev multiple reflections because tunnel coupling asymmetries $> 1 \times 10^3$ are typically sufficient to completely suppress them [40]. These arguments together with the large addition energy found in our sample (large-U regime),

allows us to attribute the excitations to YSR states.

To further qualitatively describe the experimental data, we performed numerical simulations using the single impurity Anderson model [41] with one spin degenerate pair of quasi particles at energy $\Delta = 100$ μeV, derived from a zero-bandwidth approximation (ZBW) fit [42]. The results of this calculation are shown in figure 5.1d as dotted green lines. We find that the model describes the system's behavior with high fidelity and provides a comprehensive explanation for both the ground state and the observed excitations in the stability diagram: On the left side of the CDP, the system is in a doublet ground state, with its first excited state being the YSR singlet. By adding an electron to the molecule, a phase transition from a doublet ground state to a BCS-like singlet is induced (right-hand side of the CDP). Here, the excited states take the form of a doublet. Since the system experiences weak coupling ($k_B T_K < \Delta$) it can be tuned from the YSR to a Kondo-like singlet via a doublet-singlet quantum phase transition by applying an external out-of-plane magnetic field, which predominately suppresses the superconducting gap and the exchange coupling (see figure 5.2a). According to numerical renormalization group theory (NRG) calculations [43] and experimental studies [44, 45] this phase transition happens at $k_B T_K/\Delta \approx 0.3-1$, in agreement with the results presented here.

The quantum phase transition from YSR to Kondo physics has a strong impact on the thermoelectric response of the system. As observed earlier for single-molecule junctions in the Kondo regime [36], there is a correlation between the derivative (with respect to bias voltage) of the differential conductance and the thermocurrent, where sharp conductance features yield high thermoelectric response. Thus, since the sharpness of the conductance resonances depends on the magnetic field and temperature, we observe lower thermocurrent values as these parameters increase (figure 5.2d and figure 5.3). This ultimately results in a two fold increase of the Seebeck coefficient and a five-fold increase of the power factor when going through the quantum phase transition from Kondo to YSR.

5.4. CONCLUSION

In this work we performed thermoelectric transport measurements in an all organic diradical molecule coupled to proximity induced superconducting electrodes. The molecule plays the role of a spin-1/2 system with a high addition energy that, by interacting with the superconducting electrodes, leads to the presence of in-gap Yu-Shiba-Rusinov excitations. By applying a gate voltage, the charge on the molecule can be reproducibly changed from $N-1$ to N, thereby inducing a phase transition from a doublet to singlet ground state. Applying an external magnetic field destroys the induced superconducting gap

and drives a quantum phase transition from the YSR to the Kondo regime. This leads to a drastic decrease in the thermoelectric efficiency of the system. Thus, our work demonstrates that the efficiency of heat-to-energy conversion can be amplified by the presence of YSR states which act as sharp energy filters. While follow-up studies are required to investigate heat flow in such junctions, this work already provides information on how the power factor values can be boosted by in-gap states. By further optimizing parameters like the tunnel coupling strength, such molecular heat engines might posses thermoelectric efficiencies close to the theoretical limit.

5.5. APPENDIX

5.5.1. SAMPLE FABRICATION

The device is assembled on a Si wafer with a 285 nm layer of SiO_2 on top. All lithography steps are performed with electron beam lithography (Raith EBPG 5000+). Before each step, the sample is pretreated with acetone and isopropanol for one min. and spincoated with two layers of resist (8.5 MMA, 11% in Ethyl Lactate; 6000 rpm for 1 min.; baking at 180 °C for 5 min., and PMMA Solid 2% in Anisole, 950.0 molecular weight; 4000 rpm for 1 min.; baking at 180 °CC for 3 min.). After lithography and development in MIBK : IPA = 1 : 3 for 90 s, the metals (Ti, Pd and Au) are deposited onto the structure by means of an e-beam evaporator (high vacuum around 10^{-8} mbar, evaporation rate of 0.5 Å/s) and molybdenum rhenium (MoRe) superconducting contacts are sputtered with an AC450 Allience system (RF generator power 100 W, process pressure 20 mbar pressure, Ar flow 15 sccm).

A schematic design of the sample is depicted in figure 5.1a. It consists of a local gate (purple color) that is made by depositing a 1 nm thick adhesion layer of Ti and a 7 nm thick layer of Pd; two heaters (blue color) that are put together by evaporation 3 nm of Ti and 27 nm of Pd; 13 nm thick Au bridge (yellow color); and contacts (brown color) that are assembled by sputtering 100 nm MoRe. An insulating layer of 10 nm aluminum oxide, Al_2O_3, is deposited by atomic layer deposition in an Oxford Instruments FlexALD system (300 °C) right after the gate and heater deposition steps to form a dielectric for the gate and to prevent leakage from the heaters to the contacts.

5.5.2. ELECTROMIGRATION OF THE JUNCTION AND MOLECULAR DEPOSITION

Electromigration of golden junctions is performed by means of an active breaking scheme [46]. The idea behind the method is to increase the voltage across the junction via an ADwin GOLD box while simultaneously monitoring the resistance in an active feedback loop. The application

of a high current density through the narrowest constriction induces electron momentum, which is sufficient to move the gold atoms, resulting in junction resistance modifications. Once the change of resistance reaches a specific value (cut-off parameter), the voltage is automatically reduced to zero and the ramping process is repeated. In such way the junction resistance is increased to 4 kΩ and then the junction is allowed to undergo self breaking [47] for approximately 10 min with further breaking during the subsequent molecular deposition and vacuum steps.

The molecule is dissolved in Dichloromethane (DCM) with a 0.1 mM concentration and deposited on the chip right after electromigration via the drop-cast method. To avoid self-breaking of the gold junctions to sizes that would exceed the molecular size ($1-2$ nm), the sample is thereafter immediately pumped to a low pressure and cooled down to low temperatures.

5.5.3. SIMULTANEOUS CONDUCTANCE AND THERMOPOWER MEASUREMENTS

The measurements of conductance and thermocurrent are done simultaneously with a lock-in double-modulation technique [33] that is schematically illustrated in figure 5.1c. The differential conductance G, thermal current I_{th} and I_{DC} are measured by adding a small ac component ($V_{\text{AC}} = 5$ μV) at a frequency ω_1 =13 Hz to bias voltage V_B, while an ac current through the heater at a frequency ω_2 =3 Hz is applied that creates an ac temperature bias proportional to Joule heating $\sim I_{\text{H}}^2$. The G is extracted from $\frac{I_{\text{AC}}}{V_{\text{AC}}}$, where the I_{AC} current is measured with a lock-in at ω_1, and the I_{th} is measured at $2\omega_2$. To determine the value of thermocurrent it is important to apply a correction factor of -2$\sqrt{2}$ to Y-component of the lock-in, recording the thermocurrent signal. This adjustment parameter arises from two factors: firstly, $\sqrt{2}$ from the fact that lock-in measures the root-mean-square voltage value and, secondly, -2 is attributed to the physical relationship between measured signal and ΔT that is proportional to $\sim I_{\text{H}}^2$. The AC measurements were conducted with 1 μA current passing through the heater (440 Ω), which was the default setting employed through all stability measurements at 150 mK.

5.5.4. STABILITY DIAGRAM AT 675 MK

Figure 5.4a shows the conductance as a function of gate voltage for the devices discussed in the main text. Within the accessible gate range (-5 V.. 5 V) only one conductance peak (indicating a charge degeneracy point) is observed. The corresponding stability diagram, with a large bias window of 30 mV is shown in figure 5.4b. From the edges of the Coulomb

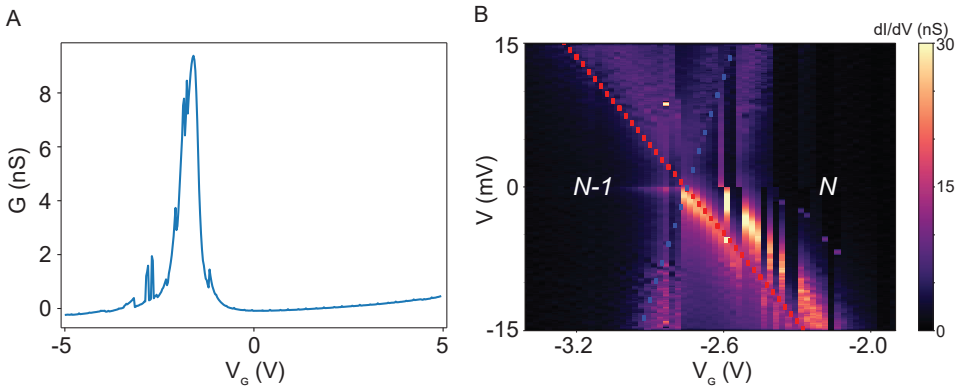

Figure 5.4: a. Conductance as a function of gate at 10 mV bias showing one pronounced peak. b. Stability diagram in the peak vicinity depicted for 30 mV bias window. Blue and red dotted lines highlight the edges of the Coulomb diamond. Switches are present due to changes in the electrostatic environment, most likely due to the motion of trapped charges in the gate oxide. Both figures are recorded at 675 mK.

diamond the slopes, $\frac{C_G}{C_G+C_D} \approx 0.078$ and $\frac{C_G}{C_S} \approx 0.031$ can be determined, where C_G,C_S and C_D are the mutual capacitances between the molecule and the gate, the source and the drain, respectively. In addition, the gate coupling parameter can be estimated as $\alpha = 0.022$, allowing the estimation of the lower limit for the addition energy $E_{add} > 0.18$ eV. Such high E_{add} are typical for single-molecule devices.[48] Gold grains of comparable nanometer sizes typically exhibit higher gate couplings (> 0.2)[49] and lower addition energies.

5.5.5. ESTIMATION OF THE KONDO TEMPERATURE

At magnetic field values higher than 30 mT, the system exhibits a pronounced zero bias peak in the $N-1$ region of the stability diagram, related to the Kondo effect. To estimate the Kondo temperature we recorded bias traces of the differential conductance at a magnetic field of 60 mT, $V_G = -2.85$ V and for different base temperatures (figure 5.5a). The Kondo peak broadens and its amplitude decreases with increasing temperature. The full peak width at half maximum (FWHM) at 100 mK is 0.16±0.01 meV. This value allows to estimate the

Kondo temperature using[50]

$$\mathrm{FWHM} = 2\sqrt{(\pi k_B T)^2 + 2(k_B T_K)^2}, \tag{5.1}$$

which yields $T_K = 0.73 \pm 0.04$ K. Furthermore, a Lorentzian function was used to fit each dI/dV curve, and to extract the amplitude of the conductance peak (figure 5.5b).To extract the Kondo temperature, we fitted the this data using the empirical formula[51]

$$G(T) = G_b + G_l\left(\frac{T^2}{T_K^2}(2^{\frac{1}{s}} + 1)\right)^{-s}, \tag{5.2}$$

where G_b is the background conductance coming from a parallel tunneling pathway between the leads, $G_l = \frac{2e^2}{h}\frac{4\Gamma_s\Gamma_d}{(\Gamma_s+\Gamma_d)^2}$ is the maximum conductance at zero temperature and $s = 0.22$ for a spin-1/2 system. The resulting Kondo temperature is 0.78±0.16 K (figure 5.5b). From G_l we can also confirm that the coupling to the leads is very asymmetric, and that the ratio of the couplings is $\approx 1.2 \times 10^4$.

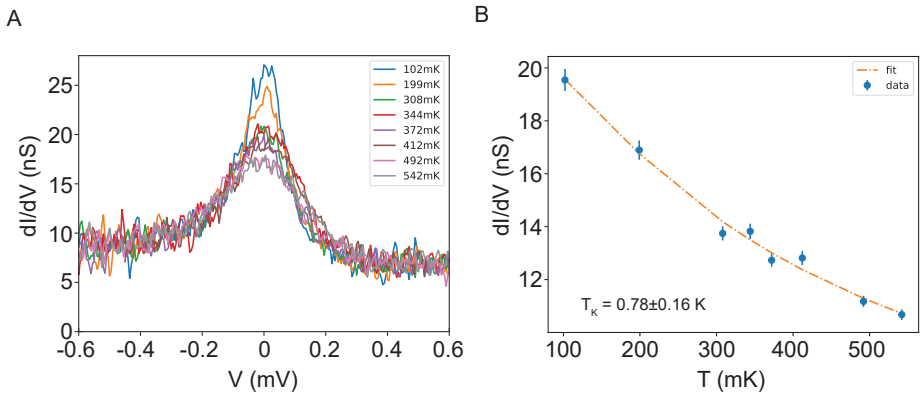

Figure 5.5: a. Differential conductance as a function of bias voltage at a constant gate voltage of $V_G = -2.85$ V, for different base temperatures. b. Maximum of peak conductance as a function of temperature extracted from A (blue dots) and fit to the s = 1/2 Kondo model (equation 5.2 with s = 0.22) with fit parameters $G_b = 8$ nS, and $G_l = 25$ nS. The Kondo temperature is indicated in the figure.

5.5.6. CHARGE DEGENERACY POINT VS. MAGNETIC FIELD

To investigate what the ground state of the system is once the number of electrons on the molecule changes from $N-1$ to N, we recorded zero-bias gate sweeps for different magnetic fields. The measured data indicates that the charge degeneracy point (CDP) is moving towards less negative gate voltages (figure 5.6a). This behavior indicates that the ground-state spin in the N region is lower than that in $N-1$, in line with a doublet singlet transition. To further confirm this, we fitted a Lorentzian function to each dI/dV vs. V_G and extracted the maximum of the peak at different magnetic fields. This maximum corresponds to the position of the CDP and shows nonlinear dependence on the magnetic field (see figure 5.6b). We relate this non-linearity to Kondo correlations that influence the peak position at lower magnetic fields. The data at higher magnetic fields is used to extract $\alpha d\Delta(eV_G)/dB = 1.0 \pm 0.1\ \mu_B$ (green linear dotted line in figure 5.6b), where α is the gate coupling. This coefficient is proportional to the difference of ground-state spins on the $N-1$ and the N side:

$$\alpha\Delta(eV_G) = \mu_B(g^N S^N - g^{N-1}S^{N-1})B, \tag{5.3}$$

where μ_B is the Bohr magneton, S is the total spin, and g is the Lande g-factor. The value of $1\mu_B$ aligns well with expectations for g=2, and $\Delta S = \frac{1}{2}$.

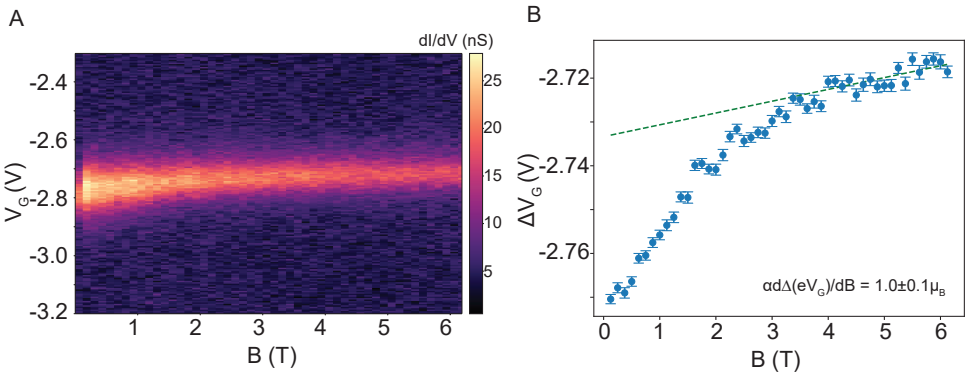

Figure 5.6: A) Differential conductance as a function of gate voltage and magnetic field at 100 mK. B) Charge degeneracy position as a function of applied magnetic field.

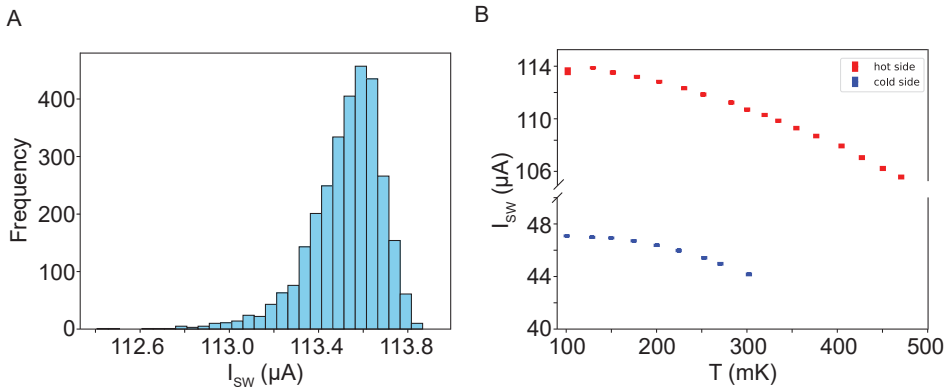

Figure 5.7: a. Histogram of stochastic switching current for one of the thermometers at 150 mK. b. Temperature dependence of averaged switching current, I_{SW}, for the thermometer located close to the heater (red) and for the thermometer on the opposite side (blue).

5.5.7. THERMOMETRY

The temperature difference across the molecule during thermoelectric measurements was determined via the thermometry method that we developed for molecular devices[34] (see also chapter 3). Briefly, MoRe contacts together with the golden bridge form superconductor-normal metal-superconductor junctions, where the critical current depends on the electronic temperature of the gold. We calibrate the thermometers with respect to the base temperature. To achieve this, we bias the current through the junction and read out the voltage, and record the switching current at each temperature. A typical distribution is shown in figure 5.7a. At each temperature, we also apply current through the heater and check how it influences the value of the switching current. Consequently, we get a switching current dependence on the temperature for two thermometers: one located close to the heater (figure 5.7b red symbols), and one on the opposite side (figure 5.7b blue symbols). From the fits, we estimate that at a base temperature of 150 mK (the base temperature used in figure 5.3 in the main text), the temperature drop over the molecule is around 105 mK. It is also worth mentioning that during all thermometry measurements, we keep the magnetic field constant (30 mT) to decrease the value of switching current and avoid overheating during the measurements.

5.5.8. THEORETICAL MODEL FOR SUB-GAP STATES

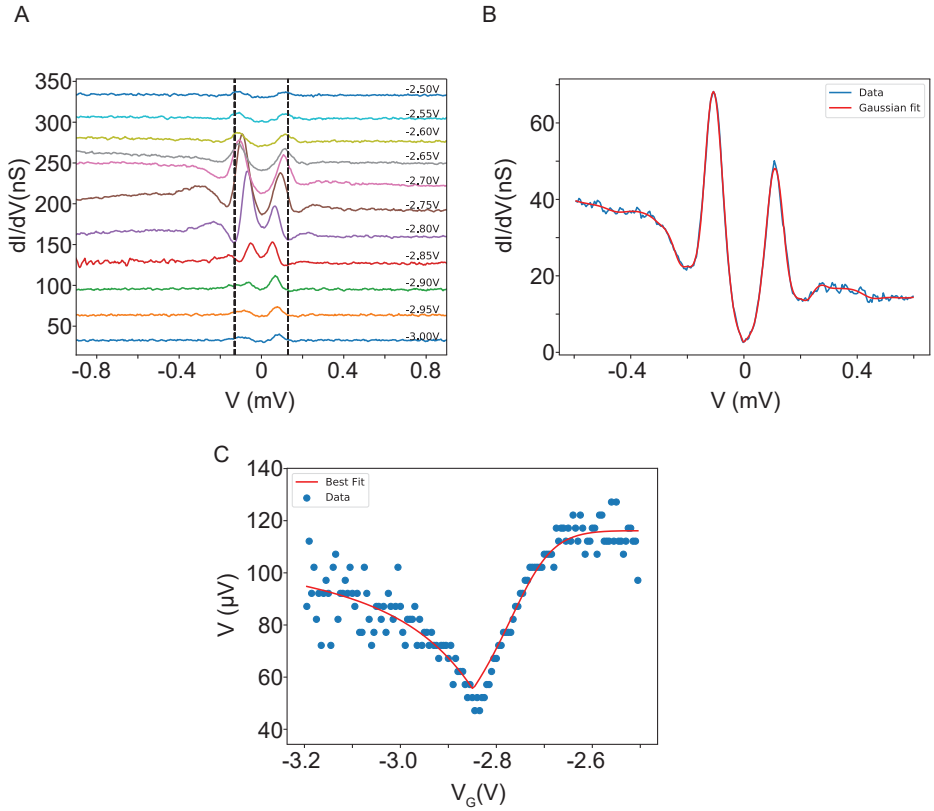

Figure 5.8: a. Differential conductance as a function of bias voltage at different gate voltages. Curves are displaced vertically for clarity, with gate voltage increasing from bottom to top and highlighted with its color. Two dotted black lines indicate the superconducting gap. b. Gate trace at V_G =-2.7 V fitted with two Gaussian functions and a spline (red color). c. Position of the positive in-gap state as a function of gate voltage (blue dots); the red solid line is a fit to the data using the zero-bandwidth approximation.

In order to model the dispersion of the sub-gap peaks in the differential conductance, we model the molecule as an Anderson impurity, a single quantum level with on-site energy ϵ_d and charging energy, U. The gold

electrodes, which exhibit a superconducting energy gap (or minigap) due to the superconducting proximity effect from the MoRe, are modelled as BCS superconductors, with order parameters Δ_1 and Δ_2, respectively. These are considered as electron baths to which the impurity is coupled by tunnel couplings Γ_1 and Γ_2. Considering the electron baths as constant density bands with a bandwidth D_1 and D_2 with N_1 and N_2 states, the Hamiltonian of the Anderson impurity model can be written as:

$$\begin{aligned}\hat{H} &= \epsilon_d \sum_{\sigma\in\{\uparrow,\downarrow\}} \hat{n}_{d,\sigma} + U\hat{n}_{d,\uparrow}\hat{n}_{d,\downarrow} \\ &+ \sum_{k\in\Omega_1\cup\Omega_2,\sigma\in\{\uparrow,\downarrow\}} \epsilon_k \hat{n}_{k,\sigma} \\ &+ \sum_{k\in\Omega_1,\sigma\in\{\uparrow,\downarrow\}} (\Delta_1 \hat{c}^\dagger_{k,\sigma}\hat{c}^\dagger_{-k,-\sigma} + \Delta_1^* \hat{c}_{-k,-\sigma}\hat{c}_{k,\sigma}) + \sum_{k\in\Omega_2,\sigma\in\{\uparrow,\downarrow\}} (\Delta_2 \hat{c}^\dagger_{k,\sigma}\hat{c}^\dagger_{-k,-\sigma} + \Delta_2^* \hat{c}_{-k,-\sigma}\hat{c}_{k,\sigma}) \\ &+ \sqrt{\frac{\Gamma_1 D_1}{\pi N_1}} \sum_{k\in\Omega_1,\sigma\in\{\uparrow,\downarrow\}} (\hat{c}^\dagger_{k,\sigma}\hat{c}_{d,\sigma} + \hat{c}^\dagger_{d,\sigma}\hat{c}_{k,\sigma}) + \sqrt{\frac{\Gamma_2 D_2}{\pi N_2}} \sum_{k\in\Omega_2,\sigma\in\{\uparrow,\downarrow\}} (\hat{c}^\dagger_{k,\sigma}\hat{c}_{d,\sigma} + \hat{c}^\dagger_{d,\sigma}\hat{c}_{k,\sigma}),\end{aligned} \tag{5.4}$$

where $\hat{c}_{d,\sigma}$ is the annihilation operator for electrons with spin σ on the impurity, $\hat{c}_{k,\sigma}$ is the annihilation operator for electrons with index k and spin σ in the electronic bath. Furthermore, $\hat{n}_{d,\sigma} = \hat{c}^\dagger_{d,\sigma}\hat{c}_{d,\sigma}$ is the operator for the occupancy of the impurity with spin σ.

Already without superconductivity, the single impurity Anderson model has not been solved analytically. To find an approximate solution, we solved the single impurity Anderson model by exact diagonalization in the zero bandwidth limit (ZBW). In the ZBW, one takes $D_1, D_2 \to 0$, reducing Ω_1 and Ω_2 to single levels, while keeping the effective tunnel coupling constant. In addition, we consider the limit where $\Gamma_1 \gg \Gamma_2$. The effective hopping integral is $t = \sqrt{\frac{\Gamma_1 D_1}{\pi N_1}}$. In this limit only a single level in Ω_1 with $\epsilon_{k,\sigma} = 0$ needs to be taken into account and the single impurity Anderson model becomes a two-site model. Furthermore, since the experimentally found charging energy is large, we consider the limit where $U \to \infty$.

Solving the model by exact diagonalization results in eigenstates and eigenenergies. These eigenenergies disperse as a function of ϵ_d, which we use to simulate the gate voltage dependency. When $\epsilon_d \gg 0$, the impurity is unfilled and the ground state is a spin singlet. On the other hand, when $\epsilon_d \ll 0$, the impurity is filled with a single electron and the ground state is a spin doublet state. The transition between these two ground states lies around $\epsilon_d = 0$. Around the transition, there is a low energy excitation with $E_{\text{exc}} < |\Delta_1|$ - a sub-gap excitation. The excitation

energy, the energy difference between the ground state and the first excited state, is the minimum energy that is required for electrons to be injected or ejected from the impurity site. In transport, electrons are transferred from the impurity site to a superconductor with minimum excitation energy $|\Delta_2|$ (or vice versa). As a result, in transport the subgap excitation is observed at a voltage $V_{\text{exc}\pm} = \pm(|\Delta_2| + E_{exc})/e$.

Qualitatively, the model describes the physics of an Anderson impurity coupled to a BCS superconductor. In this model, Yu-Shiba-Rusinov (YSR) sub-gap states form due to the pair breaking associated with the non-superconducting impurity. In the model, the excitation energy related to the YSR state depends on the on-site energy of the impurity level. To allow for fitting the model to the experimental data, two Gaussian functions and a spline were fitted to the extracted dI/dV bias traces for different gate voltages from the stability diagram (see figure 5.8b). This procedure allows us to take into account the background and obtain positions of the peaks. The evolution of the in-gap states is depicted in figure 5.8c. Their energy decreases and reaches a minimum at $V_G = -2.83$ V (indicating the value of $|\Delta_2|/e$) near the doublet-singlet transition and then rises and saturates as the energy of the peak reaches the superconducting gap (bias voltage of $e(\Delta_1 + \Delta_2)$). The transition itself happens at around -2.83 V and is on the left side with respect to the CDP. By solving the Hamiltonian of equation 5.4 we extract the energy difference between the excited state and the ground state. We use Δ_1, Δ_2, and t, as fitting parameters. The fitting parameters rely minimally on charging energy (in the range of 0.18 eV .. 10 eV) and thus the last one is fixed to be 1 eV. The fit depicted with the red solid line in figure 5.8c has been obtained with Δ_1 = 62 μeV, Δ_2 = 54 μeV, and t = 110 μeV.

5.5.9. PROXIMITY INDUCED SUPERCONDUCTIVITY IN GOLD BRIDGE

Induced superconductivity in the gold bridge coupled to magnetic moment of the molecule leads to the formation of Yu-Shiba-Rusinov states in the EMBJ junction. In this section a calculation of the density of states of gold is given to justify the experimental findings. The results are summarized in figure 5.9 and briefly discussed below.

To calculate the modified density of states as a function of distance, we consider a gold wire connected to a MoRe superconductor with critical temperature of 8.7 K (Δ = 1.3 meV, see figure 5.9a). The calculation is performed using the Usadel formalism, which works in the quasi-classical diffusive regime. To this end, we adapted the 1D code of Bosboom *et al* [52], which assumes that the inverse proximity effect of the gold on the MoRe is negligible. We have used the interface scattering parameter γ_{BM} as a free parameter in the model. The phase difference between the superconductors is fixed at $\phi = 0$. We estimate

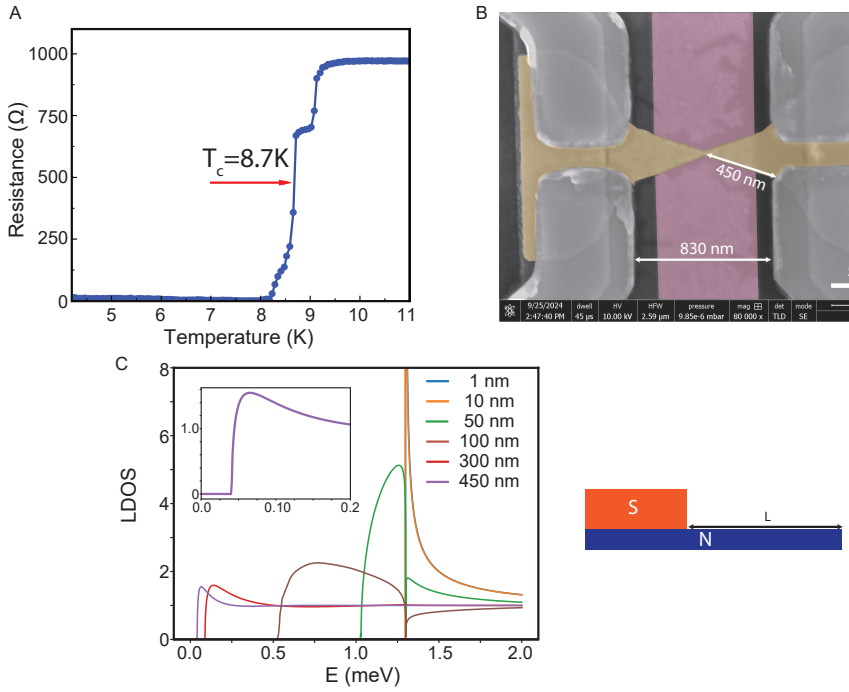

Figure 5.9: a. Temperature dependence of the corrected two-terminal resistance of MoRe. The arrow indicates the 50% resistance drop used to define the critical temperature. b. Scanning electron microscopy of the gold bridge and MoRe contacts with the dimension specifications. Parts of the device are highlighted with colors: pink (gate), yellow (gold bridge), gray (MoRe contacts). c. Simulated local density of states (LDOS) at $L = 1$, 10, 50, 100, 300, 450 nm (highlighted with different colors) with the inset displaying LDOS at $L = 450$ nm. The right panel shows a sketch of the superconductor-normal metal system used for the simulation.

the mean free path and diffusion coefficient using the normal state resistance of our thermometer at $T = 100$ mK, $R = 1.08$ Ω. Using the dimensions $L_t = 250$ nm and $A = 450 \times 13$ nm^2 of the thermometer, we find $\rho = \frac{RA}{L_t} = 2.53 \cdot 10^{-8}$ Ω m. The Fermi velocity of gold is $v_F = 1.4 \cdot 10^6$ m s^{-1} and the electron density is $n = 5.9 \cdot 10^{28}$ m^{-3}. Then, using the Drude formula $\frac{1}{\rho} = \frac{ne^2\tau}{m}$, where τ is the mean scattering time, we find that the mean free path is $l = v_F\tau = \frac{mv_F}{\rho ne^2} = 36$ nm. Here, we have used an effective mass of 1.1 times the electron mass, consistent with

earlier studies by Wolz et al [53]. Then, the diffusion coefficient is $D_N = 0.017$ m^2/s. The effective coherence length in the gold thin film is $\xi_N = \sqrt{\frac{\hbar D_N}{2|\Delta|}} \approx 66$ nm.

Using the diffusion constant found above and $\gamma_{BM} = 0.01$, we calculate the local density of states at the end of a wire of length L. We calculate the local density of states at $L = 1$, 10, 50, 100, 300, 450 nm. The last value is chosen to match the real dimensions of the sample (see SEM picture of the device in figure 5.9b). The results of this calculation are shown in figure 5.9c. As can be seen from these results, the gold bridge contacting the molecule is fully proximitized with $\Delta = 60$ μeV, which is close to the Thouless energy $E_{Th} = \frac{\hbar D_N}{L^2} = 55$ μeV. This value is in a good agreement with experimental observations.

REFERENCES

[1] J. Zhang, A. Tselev, Y. Yang, K. Hatton, P. Barbara, and S. Shafraniuk. “Zero-bias anomaly and possible superconductivity in single-walled carbon nanotubes”. *Phys. Rev. B* 74 (15 Oct. 2006), p. 155414.

[2] A. Kumar, M. Gaim, D. Steininger, A. L. Yeyati, A. Martín-Rodero, A. K. Hüttel, and C. Strunk. “Temperature dependence of Andreev spectra in a superconducting carbon nanotube quantum dot”. *Phys. Rev. B* 89 (7 Feb. 2014), p. 075428.

[3] B. M. Andersen, K. Flensberg, V. Koerting, and J. Paaske. “Nonequilibrium Transport through a Spinful Quantum Dot with Superconducting Leads”. *Phys. Rev. Lett.* 107 (25 Dec. 2011), p. 256802.

[4] E. J. H. Lee, X. Jiang, R. Žitko, R. Aguado, C. M. Lieber, and S. De Franceschi. “Scaling of subgap excitations in a superconductor-semiconductor nanowire quantum dot”. *Phys. Rev. B* 95 (18 May 2017), p. 180502.

[5] T. Sand-Jespersen, J. Paaske, B. M. Andersen, K. Grove-Rasmussen, H. I. Jørgensen, M. Aagesen, C. B. Sørensen, P. E. Lindelof, K. Flensberg, and J. Nygård. “Kondo-Enhanced Andreev Tunneling in InAs Nanowire Quantum Dots”. *Phys. Rev. Lett.* 99 (12 Sept. 2007), p. 126603.

[6] J. C. Estrada Saldaña, A. Vekris, V. Sosnovtseva, T. Kanne, P. Krogstrup, K. Grove-Rasmussen, and J. Nygård. “Temperature induced shifts of Yu–Shiba–Rusinov resonances in nanowire-based hybrid quantum dots”. *Commun. Phys.* 3.1 (July 2020).

[7] K. Grove-Rasmussen, G. Steffensen, A. Jellinggaard, M. H. Madsen, R. Žitko, J. Paaske, and J. Nygård. “Yu–Shiba–Rusinov screening of spins in double quantum dots”. *Nat. Commun.* 9.1 (June 2018).

[8] R. S. Deacon, Y. Tanaka, A. Oiwa, R. Sakano, K. Yoshida, K. Shibata, K. Hirakawa, and S. Tarucha. “Tunneling Spectroscopy of Andreev Energy Levels in a Quantum Dot Coupled to a Superconductor”. *Phys. Rev. Lett.* 104 (7 Feb. 2010), p. 076805.

[9] L. Farinacci, G. Ahmadi, G. Reecht, M. Ruby, N. Bogdanoff, O. Peters, B. W. Heinrich, F. von Oppen, and K. J. Franke. “Tuning the Coupling of an Individual Magnetic Impurity to a Superconductor: Quantum Phase Transition and Transport”. *Phys. Rev. Lett.* 121 (19 Nov. 2018), p. 196803.

[10] S. Kezilebieke, M. Dvorak, T. Ojanen, and P. Liljeroth. “Coupled Yu–Shiba–Rusinov States in Molecular Dimers on NbSe2”. *Nano Letters* 18.4 (2018), pp. 2311–2315.

[11] C. B. Winkelmann, N. Roch, W. Wernsdorfer, V. Bouchiat, and F. Balestro. “Superconductivity in a single-C60 transistor”. *Nat. Phys.* 5.12 (Dec. 2009), pp. 876–879.

[12] J. O. Island, R. Gaudenzi, J. de Bruijckere, E. Burzurí, C. Franco, M. Mas-Torrent, C. Rovira, J. Veciana, T. M. Klapwijk, R. Aguado, and H. S. J. van der Zant. “Proximity-Induced Shiba States in a Molecular Junction”. *Phys. Rev. Lett.* 118 (11 Mar. 2017), p. 117001.

[13] A. Kamlapure, L. Cornils, R. Žitko, M. Valentyuk, R. Mozara, S. Pradhan, J. Fransson, A. I. Lichtenstein, J. Wiebe, and R. Wiesendanger. “Correlation of Yu–Shiba–Rusinov States and Kondo Resonances in Artificial Spin Arrays on an s-Wave Superconductor”. *Nano Letters* 21.16 (2021), pp. 6748–6755.

[14] A. Odobesko, D. Di Sante, A. Kowalski, S. Wilfert, F. Friedrich, R. Thomale, G. Sangiovanni, and M. Bode. “Observation of tunable single-atom Yu-Shiba-Rusinov states”. *Phys. Rev. B* 102 (17 Nov. 2020), p. 174504.

[15] M.-X. Wang, C. Liu, J.-P. Xu, F. Yang, L. Miao, M.-Y. Yao, C. L. Gao, C. Shen, X. Ma, X. Chen, Z.-A. Xu, Y. Liu, S.-C. Zhang, D. Qian, J.-F. Jia, and Q.-K. Xue. “The Coexistence of Superconductivity and Topological Order in the Bi₂Se₃ Thin Films”. *Science* 336.6077 (2012), pp. 52–55.

[16] D. K. Efetov, L. Wang, C. Handschin, K. B. Efetov, J. Shuang, R. Cava, T. Taniguchi, K. Watanabe, J. Hone, C. R. Dean, and P. Kim. “Specular interband Andreev reflections at van der Waals interfaces between graphene and NbSe2”. *Nat. Phys.* 12.4 (Apr. 2016), pp. 328–332.

[17] M. R. Buitelaar, W. Belzig, T. Nussbaumer, B. Babic, C. Bruder, and C. Schönenberger. “Multiple Andreev Reflections in a Carbon Nanotube Quantum Dot”. *Phys. Rev. Lett.* 91 (5 Aug. 2003), p. 057005.

[18] L. Hofstetter, S. Csonka, J. Nygård, and C. Schönenberger. “Cooper pair splitter realized in a two-quantum-dot Y-junction”. *Nature* 461.7266 (Oct. 2009), pp. 960–963.

[19] A. Das, Y. Ronen, M. Heiblum, D. Mahalu, A. V. Kretinin, and H. Shtrikman. “High-efficiency Cooper pair splitting demonstrated by two-particle conductance resonance and positive noise cross-correlation”. *Nature Communications* 3.1 (Nov. 2012).

[20] J. Kondo. “Resistance Minimum in Dilute Magnetic Alloys”. *Progress of Theoretical Physics* 32.1 (July 1964), pp. 37–49.

[21] L. Yu. “BOUND STATE IN SUPERCONDUCTORS WITH PARAMAGNETIC IMPURITIES”. *Wu Li Hsueh Pao (China) Supersedes Chung-Kuo Wu Li Hsueh For English translation see Chin. J. Phys. (Peking) (Engl. Transl.)* 21 (Jan. 1965).

[22] H. Shiba. “Classical Spins in Superconductors”. *Progress of Theoretical Physics* 40.3 (Sept. 1968), pp. 435–451.

[23] A. I. Rusinov. “Superconductivity near a paramagnetic impurity”. *Soviet Journal of Experimental and Theretical Physics letters* 9 (1969), pp. 85–87.

[24] F. Pientka, L. I. Glazman, and F. von Oppen. “Topological superconducting phase in helical Shiba chains”. *Phys. Rev. B* 88 (15 Oct. 2013), p. 155420.

[25] J. Klinovaja, P. Stano, A. Yazdani, and D. Loss. “Topological Superconductivity and Majorana Fermions in RKKY Systems”. *Phys. Rev. Lett.* 111 (18 Nov. 2013), p. 186805.

[26] J. Röntynen and T. Ojanen. “Topological Superconductivity and High Chern Numbers in 2D Ferromagnetic Shiba Lattices”. *Phys. Rev. Lett.* 114 (23 June 2015), p. 236803.

[27] J. Li, T. Neupert, Z. Wang, A. H. MacDonald, A. Yazdani, and B. A. Bernevig. “Two-dimensional chiral topological superconductivity in Shiba lattices”. *Nature Communications* 7.1 (July 2016), p. 12297.

[28] A. Yazdani, B. A. Jones, C. P. Lutz, M. F. Crommie, and D. M. Eigler. “Probing the local effects of magnetic impurities on superconductivity”. *Science* 275.5307 (Mar. 1997), pp. 1767–1770.

[29] M. Ruby, Y. Peng, F. von Oppen, B. W. Heinrich, and K. J. Franke. “Orbital Picture of Yu-Shiba-Rusinov Multiplets”. *Phys. Rev. Lett.* 117 (18 Oct. 2016), p. 186801.

[30] S.-H. Ji, T. Zhang, Y.-S. Fu, X. Chen, X.-C. Ma, J. Li, W.-H. Duan, J.-F. Jia, and Q.-K. Xue. “High-Resolution Scanning Tunneling Spectroscopy of Magnetic Impurity Induced Bound States in the Superconducting Gap of Pb Thin Films”. *Phys. Rev. Lett.* 100 (22 June 2008), p. 226801.

[31] E. Liebhaber, L. M. Rütten, G. Reecht, J. F. Steiner, S. Rohlf, K. Rossnagel, F. von Oppen, and K. J. Franke. “Quantum spins and hybridization in artificially-constructed chains of magnetic adatoms on a superconductor”. *Nat. Commun.* 13.1 (Apr. 2022), p. 2160.

[32] M. Ruby, B. W. Heinrich, Y. Peng, F. von Oppen, and K. J. Franke. “Wave-Function Hybridization in Yu-Shiba-Rusinov Dimers”. *Phys. Rev. Lett.* 120 (15 Apr. 2018), p. 156803.

[33] P. Gehring, J. K. Sowa, C. Hsu, J. de Bruijckere, M. van der Star, J. J. Le Roy, L. Bogani, E. M. Gauger, and H. S. J. van der Zant. “Complete mapping of the thermoelectric properties of a single molecule”. *Nature Nanotechnology* 16.4 (Apr. 2021), pp. 426–430.

[34] S. Volosheniuk, D. Bouwmeester, C. Hsu, H. S. J. van der Zant, and P. Gehring. “Implementation of SNS thermometers into molecular devices for cryogenic thermoelectric experiments”. *Applied Physics Letters* 122.10 (Mar. 2023), p. 103501.

[35] N. Roch, S. Florens, V. Bouchiat, W. Wernsdorfer, and F. Balestro. “Quantum phase transition in a single-molecule quantum dot”. *Nature* 453.7195 (May 2008), pp. 633–637.

[36] C. Hsu, T. A. Costi, D. Vogel, C. Wegeberg, M. Mayor, H. S. J. van der Zant, and P. Gehring. “Magnetic-Field Universality of the Kondo Effect Revealed by Thermocurrent Spectroscopy”. *Phys. Rev. Lett.* 128 (14 Apr. 2022), p. 147701.

[37] I. Martin and D. Mozyrsky. “Nonequilibrium theory of tunneling into a localized state in a superconductor”. *Phys. Rev. B* 90 (10 Sept. 2014), p. 100508.

[38] K. Behnia. “Fundamentals of Thermoelectricity”. *Oxford University Press.* (2015).

[39] P. Gehring, J. M. Thijssen, and H. S. J. van der Zant. “Single-molecule quantum-transport phenomena in break junctions”. *Nature Reviews Physics* 1.6 (June 2019), pp. 381–396.

[40] E. J. H. Lee, X. Jiang, R. Aguado, G. Katsaros, C. M. Lieber, and S. De Franceschi. “Zero-Bias Anomaly in a Nanowire Quantum Dot Coupled to Superconductors”. *Phys. Rev. Lett.* 109 (18 Oct. 2012), p. 186802.

[41] P. W. Anderson. “Localized Magnetic States in Metals”. *Phys. Rev.* 124 (1 Oct. 1961), pp. 41–53.

[42] F. von Oppen and K. J. Franke. “Yu-Shiba-Rusinov states in real metals”. *Phys. Rev. B* 103 (20 May 2021), p. 205424.

[43] O. Sakai, Y. Shimizu, H. Shiba, and K. Satori. “Numerical renormalization group study of magnetic impurities in superconductors. II. Dynamical excitation spectra and spatial variation of the order parameter”. *J. Phys. Soc. Jpn.* 62.9 (Sept. 1993), pp. 3181–3197.

[44] K. J. Franke, G. Schulze, and J. I. Pascual. “Competition of Superconducting Phenomena and Kondo Screening at the Nanoscale”. *Science* 332.6032 (2011), pp. 940–944.

[45] J. O. Island, R. Gaudenzi, J. de Bruijckere, E. Burzurí, C. Franco, M. Mas-Torrent, C. Rovira, J. Veciana, T. M. Klapwijk, R. Aguado, and H. S. J. van der Zant. “Proximity-Induced Shiba States in a Molecular Junction”. *Phys. Rev. Lett.* 118 (11 Mar. 2017), p. 117001.

[46] H. S. J. van der Zant, Y.-V. Kervennic, M. Poot, K. O’Neill, Z. de Groot, J. M. Thijssen, H. B. Heersche, N. Stuhr-Hansen, T. Bjørnholm, D. Vanmaekelbergh, C. A. van Walree, and L. W. Jenneskens. “Molecular three-terminal devices: fabrication and measurements”. *Faraday Discuss.* 131 (0 2006), pp. 347–356.

[47] K. O’Neill, E. A. Osorio, and H. S. J. van der Zant. “Self-breaking in planar few-atom Au constrictions for nanometer-spaced electrodes”. *Applied Physics Letters* 90.13 (Mar. 2007), p. 133109.

[48] J. M. Thijssen and H. S. J. Van der Zant. “Charge transport and single-electron effects in nanoscale systems”. *physica status solidi (b)* 245.8 (2008), pp. 1455–1470.

[49] K. O’Neill, E. A. Osorio, and H. S. J. van der Zant. “Self-breaking in planar few-atom Au constrictions for nanometer-spaced electrodes”. *Applied Physics Letters* 90.13 (Mar. 2007), p. 133109.

[50] K. Nagaoka, T. Jamneala, M. Grobis, and M. F. Crommie. “Temperature Dependence of a Single Kondo Impurity”. *Phys. Rev. Lett.* 88 (7 Feb. 2002), p. 077205.

[51] D. Goldhaber-Gordon, J. Göres, M. A. Kastner, H. Shtrikman, D. Mahalu, and U. Meirav. “From the Kondo Regime to the Mixed-Valence Regime in a Single-Electron Transistor”. *Phys. Rev. Lett.* 81 (23 Dec. 1998), pp. 5225–5228.

[52] V. Bosboom, J. J. W. V. der Vegt, M. Y. Kupriyanov, and A. A. Golubov. “Selfconsistent 3D model of SN-N-NS Josephson junctions”. *Superconductor Science and Technology* 34.11 (Oct. 2021), p. 115022.

[53] M. Wolz, C. Debuschewitz, W. Belzig, and E. Scheer. “Evidence for attractive pair interaction in diffusive gold films deduced from studies of the superconducting proximity effect with aluminum”. *Phys. Rev. B* 84 (10 Sept. 2011), p. 104516.

6

A MONOMOLECULAR HEAT ENGINE

"*I sell here, Sir, what all the world desires to have—POWER.*"

James Watt

In this chapter, we explore the thermoelectric properties of a diradical organic molecule at a few Kelvin temperatures with the double lock-in technique. By subjecting the molecule to a temperature gradient and connecting it in series to a load resistance, we realize a particle exchange heat engine. Such an engine does not have any moving parts and is a few nanometer in size. It emerges as an ideal candidate for low-temperature applications where miniaturization is of paramount importance. We observe a variation of a few orders of magnitude in device performance between two molecular junction configurations, thereby illustrating the importance of precise control over the molecular-lead coupling. Our findings thus highlight the pivotal role of the connection of the molecule to the leads when aiming to harness the potential of single molecular devices for energy harvesting applications.

6.1. INTRODUCTION

Addressing heat waste is of crucial importance, considering the fact that more than 70% of the global energy is wasted as heat [1], contributing to global warming [2] and equipment malfunction. One of the approaches to tackle this problem is to use conventional cyclic heat engines, that use a temperature difference to produce useful work. However, they require moving parts and can not be utilized in small devices, making them impractical for nanoelectronics. The particle exchange (PE) heat engines [3] may serve as a good alternative. PE heat engines utilize particles (electrons, photons, etc.) to transfer heat between the hot (temperature T_H) and cold parts (temperature T_C) of a device. The heat can then perform work against an external electrical field. Also, depending on the architecture, the size of PE heat engines can be as small as tens of nanometers which makes them ideal candidates to be implemented in systems that suffer from local heating.

Recently, different PE engines were proposed theoretically [4–6] and realised [7–9] with various degrees of success in maximizing power output and efficiency. Some of the most efficient solutions include superconducting spin selective tunnel junctions [10], heat engine with ultracold atoms [11] and a realization of an InAs/InP heterostructured nanowire quantum dot (QD) heat engine [12]. In the latter work, the authors reached high efficiency at a finite power that exceeded $0.7\eta_C$, where $\eta_C = 1 - \frac{T_C}{T_H}$ is the Carnot efficiency. The study revealed a high QD potential as a good heat harvester. Follow-up investigations (e.g. [13, 14]) devoted to optimization of power output and efficiency revealed how to reach the optimal load resistance that maximizes the power output [13] and discussed the importance of the lead-dot coupling (Γ) optimization (i.e., creating an optimal energy band filter, Γ/k_BT; here, k_B is Boltzmann constant) to achieve the best performance at a certain temperature T [14].

Another interesting platform to consider for PE heat engine applications is the field of molecular devices. Recently, single molecules have shown to exhibit a potential for future applications, including memory effects [15, 16], negative differential conductance [17], magnetic effects [18–20], spin blockade effects [21], etc. Thermoelectric properties of the single molecules are of interest as well. Thermoresponses of molecular devices were investigated in several studies [22–24] (see also [25] and references within). It is theoretically predicted that they should exhibit a high thermoelectric response [26]. The straightforward construction and further synthesis of molecules enable the utilization of effects such as quantum interference [27–30], the Kondo correlations [31, 32], the Fano resonance [33, 34], leveraging of molecule-lead interaction (i.e., how it is done in Chapter 5) to generate sharp features in the transmission function and boost the system's Seebeck response. This potentially could result in an infinitely high figure of merit, ZT

coefficient, suggesting that such devices might operate as efficient heat energy harvesters near the Carnot efficiency limit, with efficiency, $\eta = \eta_C \frac{\sqrt{1+ZT}-1}{\sqrt{1+ZT}+1}$. This outlook highlights the strong demand for realizing a monomolecular heat engine.

In this work, we investigated a diradical molecule as a potential candidate for heat-energy harvesting purposes. First, its thermal and transport properties were examined in three-terminal electromigrated break junction (EMBJ) devices. Then, different load resistances (R_{load}) were connected in series to the device, and a temperature gradient was applied across the molecule. For each R_{load} we recorded the power output and estimated the engineering efficiency of the device as a function of gate voltage and active load. Our data indicated that Sme-2Os can execute work and act as a monomolecular heat engine.

We organize this report as follows: first, we offer a brief overview of the device architecture and measurement technique. Next, we describe the structure of the molecule and provide a motivation for utilizing the Sme-2Os molecule in this study. Then, we describe the physics behind two stable configurations of the molecule inside the EMBJ and move on to the realization of the molecular heat engine. We focus our attention on the maximum power output of the monomolecular heat engine for different R_{load} and discuss its efficiency.

6.2. DEVICE AND MEASUREMENT PROTOCOL

6.2.1. DEVICE

For this study, we employ a three-terminal EMBJ device with two embedded local heaters near a golden bridge [23]. The schematic representation and scanning microscope photographs of the device are depicted in figures 1.a,c. The main components include the 8 nm Pd gate (pink), 27 nm Pd heaters (blue), 12 nm Al_2O_3 protective layer (not visible), 13 nm Au bridge (yellow), and 50 nm Au contacts (grey). Details on the fabrication process are available in a Ref. [35]. We deposited the Sme-2Os molecule (0.1 mMol solution of the molecule and dichloromethane (DCM)) on the sample (see next paragraph). The gold bridge electromigrated [36] to 4 kΩ and left for self migration (at room temperature, 10^{-2} mbar) for approximately 10 minutes with further cooling down to the base temperature of 1.8 K.

6.2.2. MOLECULE

In this work, we utilized the polycyclic aromatic hydrocarbon (PAH) all-organic diradical Sme-2Os molecule that was synthesized by the group of Diego Peña (see [37] for synthesis details). The molecule consists of two fluorenyl moieties hosting a radical center each and

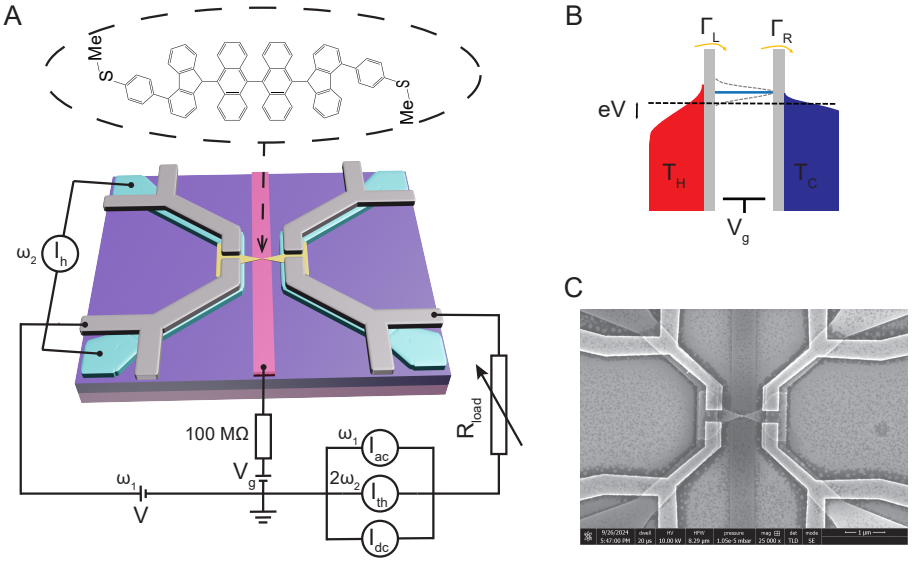

Figure 6.1: a. Sme-2Os molecule captured with the EMBJ device and thermoelectric properties of it are extracted via a double lock-in technique. b. Schematic drawing of the chemical potentials of a molecular quantum dot showing carriers can be moved against an external field once there is a temperature gradient across the junciton. c. Scanning microscope picture of a sample.

is linked together by two anthracene units (see figure 6.1a). The shape of the molecule is highly non-planar, which helps to protect its radical properties and determines the interaction between the radical parts. It also has sulfur stabilizing groups that play the role of anchors to the gold [38] and helps to increase the yield of the junction formation [39]. This molecule was investigated before using mechanical break junctions [39] (MCBJ), scanning tunneling microscope [37] (STM), and demonstrated Kondo resonances and inelastic electron tunneling spectroscopy signatures (singlet-triplet excitation energy $\sim$ 3 meV). These properties were found to be sensitive to molecular configuration within the junctions, with different configurations leading to a different coupling between spins and different observed phenomena.

6.2.3. THERMOELECTRIC MEASUREMENT TECHNIQUE

The measurements were performed with the AC double lock-in technique. The detailed description of the measurement methodology can be found

in chapter 4. Here, we present a schematic representation of the measurement in figure 6.1a and briefly describe it as follows: a small AC component of 50 μV voltage bias (ω_1 =13 Hz) is applied simultaneously with a current through the heater (ω_2 =3 Hz) for different gate and bias voltages. Then, the signal is demodulated with two lock-in amplifiers and a Keithley is used to record the differential conductance G (ω_1), thermocurrent, I_{th} ($2\omega_2$), and current, I (DC). The dilution fridge has a magnet that can apply the magnetic field up to 9 T, and the heater near the cold finger controls the temperature of the sample. Different R_{load} are connected in series, and the thermocurrent is measured as a function of gate voltage and power dissipated in the heater. The temperature gradient over the molecule ($\Delta T = T_{\text{H}} - T_{\text{C}}$) can push carriers against the voltage drop,$eV = \mu_{\text{C}} - \mu_{\text{H}}$, where $\mu_{\text{H}}, \mu_{\text{C}}$ are the electrochemical potentials of the contacts, and perform useful work. This process is controlled by the gate voltage, as the molecular level serves as a bridge and a filter for electric and heat flows (see figure 6.1b). Normally, the charging energy of the molecules is very high [40], and only one level needs to be considered. In case of small molecular-lead coupling Γ, unwanted heat flow is suppressed. If no external voltage is applied, but heater is on the circuit self-consistently satisfies $V = -I_{\text{th}} R_{\text{load}}$. The carriers would then perform work on the load with power $P = I_{\text{th}}^2 R$. The efficiency of the process calculated as $\eta = \frac{P}{J_{\text{Q}}}$, where J_{Q} is a heat flow through the molecule.

6.3. CHARACTERIZATION OF MOLECULAR CONFIGURATION

We investigated the thermoelectric properties of Sme-2Os in two stable configurations (see figures 6.2a,b). In both instances, it was possible to observe one molecular level in the accessible gate voltage range. The second configuration was attained in the same junction after an uncontrolled change in the configuration. Each of the configurations displays similar physical phenomena: a Kondo resonance on the left side from the charge degeneracy point (CDP) and inelastic co-tunneling on the other side. Despite the fact that the molecular level does not move much in energy during the reconfiguration, we witness the change of coupling and as a result an order change in the conductance and thermocurrent response. Also, there is a current-blockaded region at low negative bias on the right side of the configuration 2. Below we describe both configurations in more detail.

The stability diagram in figure 6.2a is recorded in configuration 1 for $V = -7$ to 7 meV and $V_{\text{G}} = -5.5$ to -4.0 V. It shows parts of a Coulomb diamond with a charge degeneracy point located at $V_{\text{G}} = -4.7$ V. The slopes of the edges of the diamonds are 0.004 and 0.012, providing information about the gate coupling of 0.009 and the ratio between

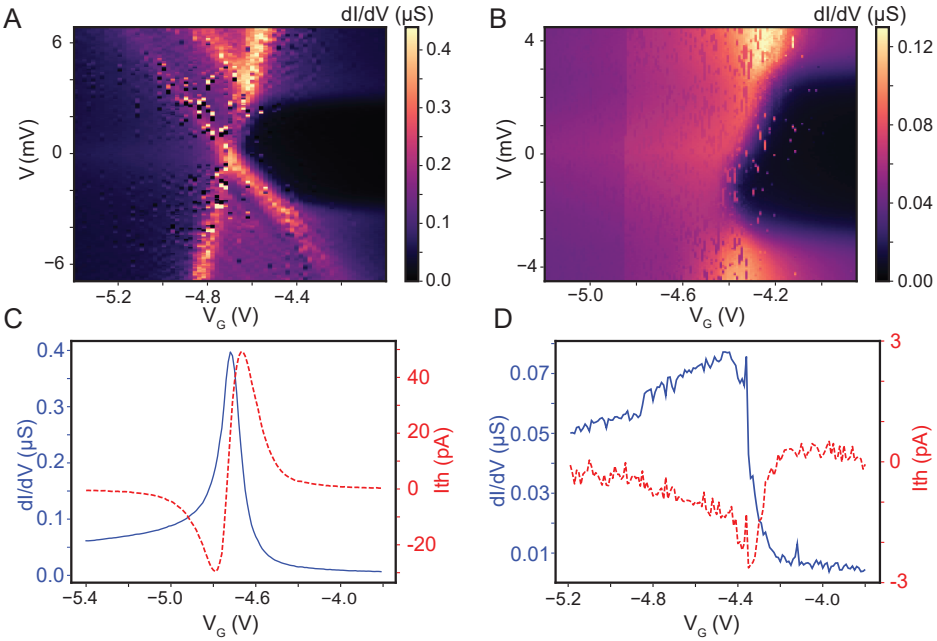

Figure 6.2: a,b. Differential conductance as function of gate and bias voltage for configuration 1 (a) and configuration 2 (b).c,d. Zero-bias gate traces for differential conductance and thermocurrent as a function of gate voltage for configuration 1 (c) and configuration 2 (d).

lead capacitances $\frac{C_S}{C_D} = 3.5$. The conductance of the system increases up to 52 μS at $V_G = -4.48$ V, $V = 7$ mV and is higher for the positive diamond edge. There is a pronounced excitation line at positive bias that runs parallel to the edge of the diamond and intersects the other edge at 3 mV. We do not observe signatures of the same excitation for negative bias, suggesting an asymmetric coupling to the source and drain ($\Gamma_S << \Gamma_D$).

We continue exploring the stability diagram by focusing our attention on the zero-bias peak at the left hand from CDP. This conductance enhancement has a Kondo origin. The full width at half maximum (FWHM) of the peak is around 2 meV that allows us to estimate the Kondo temperature from [41], $FWHM = \frac{2}{e}\sqrt{(\pi k_B T)^2 + 2(k_B T_K)^2}$, where T_K is the Kondo temperature and $T = 1.8$ K. The extracted value of T_K around 7 K is in good agreement with the value obtained from magnetic field measurements (see more details in appendix). Magnetic field sweeps at $V_G = -5.6$ V indicate that the system behaves as a spin-1/2 with a g-factor around 2 and that the zero-bias peak splits at

3 T yielding [42] $T_K = 7$ K.

At the right part of the CDP, $V_G > -4.7$, there are two symmetric horizontal lines that are crossing the Coloumb edges at a bias voltage between 3 and 4 mV. The amplitudes of this signal are asymmetric, and respond to external magnetic field, allowing us to exclude their possible vibration origin, and instead attributing them to a spin excitation origin. The magnetic field unveils that the ground state (GS) is a singlet and the excited state is a triplet. The radical centers thus experience an antiferromagnetic coupling with $J \approx 3$ meV. Also, the CDP is moving to the less negative gate voltages when applying a magnetic field implying that the GS on the left hand side of the CDP has a higher spin than on the right. Thus, we have a doublet to singlet transition once we add an electron to the system.

Stability for the second configuration is depicted in figure 6.2b with the bias window from -5 to 5 mV and V_G ranging from -5.2 to -3.9 V. Here, the conductance is almost 5 times lower and the diamond edges are broader. The signal is very smeared and it is difficult to detect the exact edges of the Coulomb diamonds.Furthermore, the coupling is more symmetric than for the first configuration and we do observe the excitations at the positive and negative bias. There is also a suppressed current region at negative bias for V_G between 0 and -2.5 mV. But overall the system demonstrates the same Kondo peak with $T_K = 7$ K and the same IETS lines with the maximum at 3 mV. The magnetic field does not lift the blockaded region up to 9 T and moves the CDP to the less negative gate voltage values.

In figure 6.2.c,d, we compare the zero-bias gate traces of differential conductance and thermocurrent for both configurations with a heater current of 0.1 mA. In figure 6.2c, the maximum differential conductance reaches 0.4 μS at $V_G = -4.7$ V. The coupling can be estimated from the full width at half maximum of the differential conductance curve and is around 0.5 meV. The thermocurrent changes from a minimum of -29.6 pA at $V_G = -4.79$ V to a maximum of 49.1 pA at $V_G = -4.66$ V, with $\frac{|I_{th+}|}{|I_{th-}|} \approx 1.66$. For the second configuration, G is much lower and attains a maximum of 0.07 μS around $V_G = -4.5$ V. Meanwhile, thermocurrent response changes even more drastically. Its amplitude drops more than 10 times to -2.6 pA at $V_G = -4.35$ V. Also, the asymmetry of the thermocurrent changes and the positive thermocurrent now is much lower than negative. We estimate the ratio of $\frac{|I_{th+}|}{|I_{th-}|}$ to be approximately 0.2. If we consider that the resistor of the ammeter (100 kΩ) plays the role of external load, we can estimate that the maximum power output for the first configuration to be 0.24 fW, while for the second one it is much lower, 0.0007 fW. This highlights the important role of the molecular configuration and coupling inside the junction for heat harvesting purposes.

6.4. HEAT ENGINE

The second configuration remained stable throughout the evaluation of molecular device for heat engine applications. We connected different R_{load} from 100 kΩ to 10 MΩ and investigated how the power output changed in order to determine the optimal resistance for maximum power output. The measurements were performed for different heater currents between 0.05 and 0.2 mA.

6.4.1. MAXIMUM POWER OUTPUT

For each R_{load}, we swept the gate to find the maximum thermocurrent output of the system and estimate the power output. In figure 6.3a we summarize the results of these measurements. The behavior of maximum power output on R_{load} was the same for 3 different current values running through the heater (0.10, 0.15, and 0.20 mA). First, the power output increases as the load increases. Then it reaches the maximum around 2.75 MΩ which is the optimal R_{load} for this configuration. Here, the maximum power output is 0.07 fW for 0.1 mA and 0.45 fW for 0.2 mA heater current. Lastly, the value decreases for higher R_{load} reaching the same values as for low load resistance. We investigated the load resistance only up to 10 MΩ, as at higher values capacitive effects start influencing the measurements and it is impossible to extract reliable values of thermocurrent.

6.4.2. EFFICIENCY

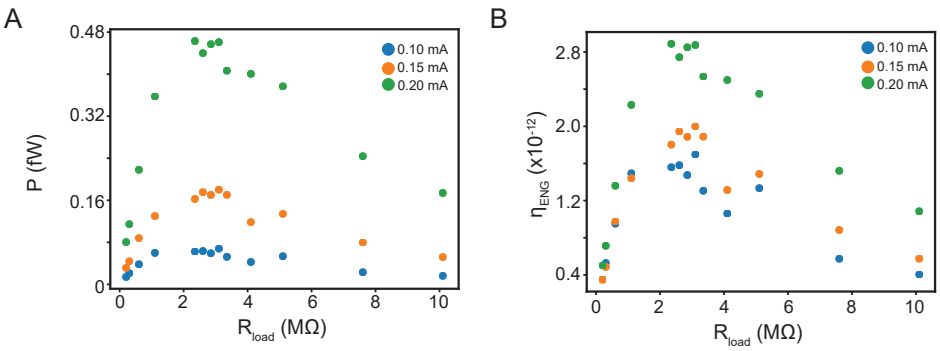

Figure 6.3: a,b. Maximum power output (a) and engineering efficiency (b) of the heat engine under different load resistances is recorded for different heater currents (blue 0.1 mA, orange 0.15 mA, green 0.2 mA).

In order to estimate the efficiency and see how close the molecular

heat engine is to the Carnot limit, the exact heat flow through the system should be determined. However, in this study, it was not possible to measure it directly as it was done in [43]. Also, configuration 2 still needs a reliable theoretical model that explains the transport features. To avoid misinterpretation and speculation we utilize the engineering efficiency, η_{ENG}, defined as $\eta_{\mathrm{ENG}} = P/P_{\mathrm{IN}}$ where $P_{\mathrm{IN}} = I^2_{\mathrm{heater}} R_{\mathrm{heater}}$ is the power dissipated in the heater. This value serves as a good indicator for application objectives but should be used carefully once comparing results from different studies. The exact location of the heater with respect to the "engine" (i.e., molecule) and the parasitic heat flow through the substrate can change the result. Thus values that are recorded with the same sample architecture or the maximum values if two different sample designs are used.

The results of η_{ENG} are illustrated in figure 6.3b. As expected, the curve replicates figure 6.3a with P_{IN} as scaling factor. The maximum engineering efficiency value for the load with the maximum power output is $1.7 * 10^{-12}$. This value is lower than the one that can be estimated from the measurements in configuration 1. The ratio between them, around 32, indicates that the first configuration is preferable for applications and highlights the need to have the right configuration/coupling in the system. Here, we also want to indicate that the ratio we provide is underestimated and in reality is much higher. A load resistance for configuration 1 is 100 kΩ. Similarly to [13] we can estimate the maximum power output would be at 26 kΩ (to obtain this value $R_{\mathrm{optimal}} \approx 1.25 \frac{k_B(T_H+T_C))}{\hbar\Gamma} \frac{h}{e^2}$, and assume that $T_H + T_C \approx 5$ K). Also, as a side remark, we also provide here the highest $\eta_{\mathrm{ENG}} = 12 * 10^{-12}$ obtained in [12]. This value is comparable with the second configuration and lower than the one in configuration 1.

In order to push the system back to the first configuration, we heated up the system several times to 200 K for a few minutes and then rapidly cooled it down. During this process few things can happen. First, the molecule can rearrange its position inside the junction. Second, the distance between the contacts can increase by thermal activation, as for our gold bridge design it is energetically favorable for the system to have a 10-15 nm gap between the leads. Thus, the process should be fast and can be implemented only a few times until the size of the gap is bigger than the length of the single molecule.

After this manipulation, we observed that the molecule was in several quasi-stable configurations and randomly changed between them. Here, by quasi-stable, we mean that the molecule was stable during one full gate sweep or more. We tried to record the maximum power output at different R_{load}. The results are represented in figures 6.4a and 6.4b. We used the same heater power ($I_{\mathrm{heater}} = 0.08$ mA) and recorded the values first changing the load resistance from the minimum to maximum and then back. Their configuration was changing from one to another one

from one resistance to another (see green line in figure 6.4a). The maximum power output was still achieved around 2.75 MΩ.

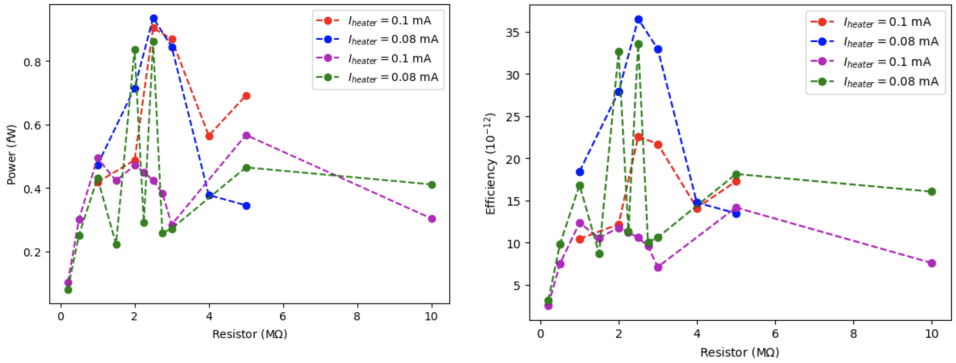

Figure 6.4: a,b. Maximum power output (a) and engineering efficiency (b) of the heat engine under different load resistances is recorded for different heater currents(red and purple for 0.1 mA; blue and green for 0.08 mA).

6

6.5. CONCLUSION

In this work, we investigated the thermoelectric properties of a diradical molecule in two stable configurations. For both formations, we observed oxidation/reduction of the molecule with the application of gate voltage. The system displays a pronounced Kondo peak on the left side of the CDP with a similar T_K for both cases and in-elastic cotunneling excitations at the same bias voltage on the right side. Magnetic field spectroscopy reveals an antiferromagnetic coupling between the radical spins of the molecule. Thermopower response was measured for both configurations and was higher for the first configuration. A monomolecular heat engine was realized by connecting a load resistor to the device. For the second configuration we investigated how the maximum power output and efficiency depend on load resistance. By varying load resistance we determined that the optimal resistance for performance is around 2.75 MΩ. The engineering efficiency in the case of the first configuration is much more efficient for a load resistor of 100 kΩ than for any load resistor at the second configuration. This observation indicates the importance of the control of molecular coupling to the leads.

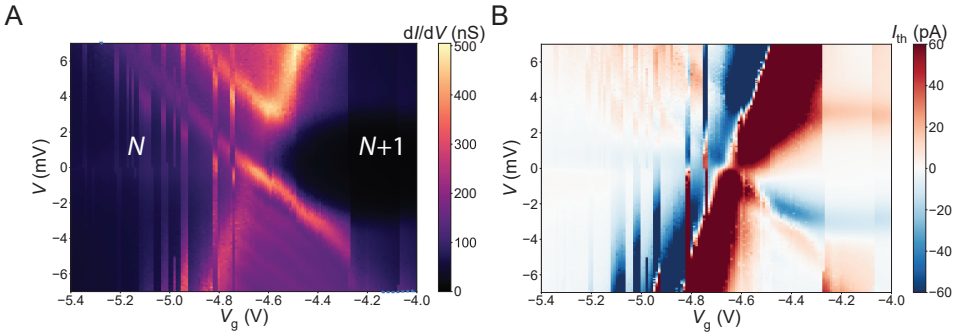

Figure 6.5: a,b. Differential conductance (a) and thermocurrent (b) stability diagrams for configuration 1.

6.6. APPENDIX

6.6.1. CONFIGURATION 1: STABILITY DIAGRAM

In figures 6.5a and 6.5b we display the differential conductance and thermocurrent measured simultaneously with the double lock-in technique for configuration 1. A summary of the measurements : is the following

- CDP is around -4.7 V, there is only one CDP in the accessible gate range (-7.5 .. 7.5 V).
- Negative diamond edge slope 0.04; positive diamond edge slope 0.012; gate coupling 0.009.
- Pronounced excitation parallel to negative slope at positive bias with a high conductance at around 0.5 μS; the same excitation at the negative bias voltages is faintly visible.
- Highly asymmetric molecule-lead coupling; total $\Gamma \approx 0.53$ meV estimated from the Coulomb peak conductance vs. gate voltage at zero bias.
- Thermocurrent signal in the investigated V V_G space ($V = -7..7$ meV, $V_G = -5.5..-4.0$ V) reaches a highest value of 300 pA.
- Thermocurrent changes its sign on the edge of the diamond that corresponds to the lead where we apply the heater.
- I_{th} is positive for IETS $V > 0$ and negative for $V < 0$.

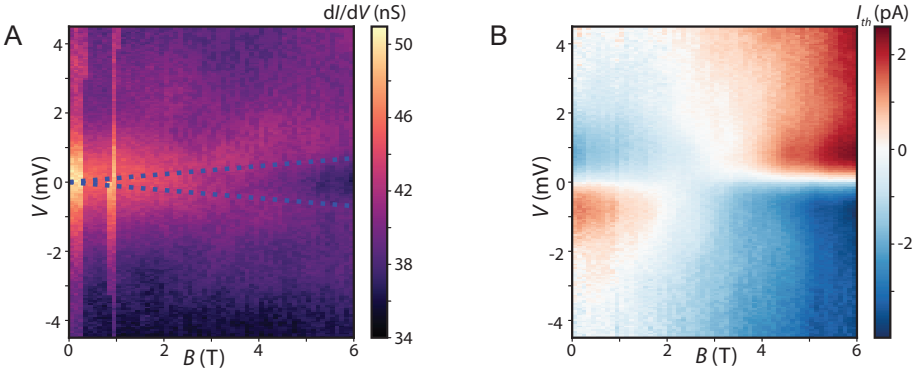

Figure 6.6: a,b. Magnetic dependence of the Kondo peak at $V_G = -5.6$ V shows a Zeeman splitting in differential conductance (a) and change of the sign in thermocurrent (b). From I_{th} measurements the critical Kondo field of 3 T can be extracted. Dashed line in (a) illustrates the Zeeman effect for a spin 1/2 system with $g = 2$ (blue) .

6

6.6.2. CONFIGURATION 1: KONDO

To investigate the zero-bias peak for $V_G < -4.7$ V, we recorded current-voltage characteristics at $V_G = -5.6$ V for different magnetic fields from 0 to 9 T. In figure 6.6a and 6.6b we demonstrate how the signal changes vs. B. Differential conductance decreases and the peak broadens with increasing magnetic field and shows the Zeeman splitting. At the highest magnetic field, the difference in energy between the ground and excited state is proportional to the magnetic field and can be written as $\frac{1}{2} g \mu_B S B$, where g is the g-factor, μ_B is the Bohr magneton, S is the spin, and B is magnetic field.A good agreement with the measured data is found if we use $S = \frac{1}{2}$ and $g \approx 2$ (see dotted lines for $g = 2$, and $g = 4$ in figure 6.6a). From this measurement, it is difficult to estimate at what magnetic field the splitting starts to occur. Meanwhile, thermocurrent allows extraction of this value as the thermocurrent changes its sign at the transition point [42]. This point is approximately at 3 T (i.e., $T_K = 7$ K).

6.6.3. CONFIGURATION 1: IETS

On the right-hand side of the CDP, we observe inelastic cotunneling excitations which in literature is also often referred to as inelastic electron tunneling spectroscopy (IETS). We recorded its behavior as a function of the magnetic field. Differential conductance and thermocurrent are illustrated in figures 6.7a and 6.7b. The IETS signal broadens but we

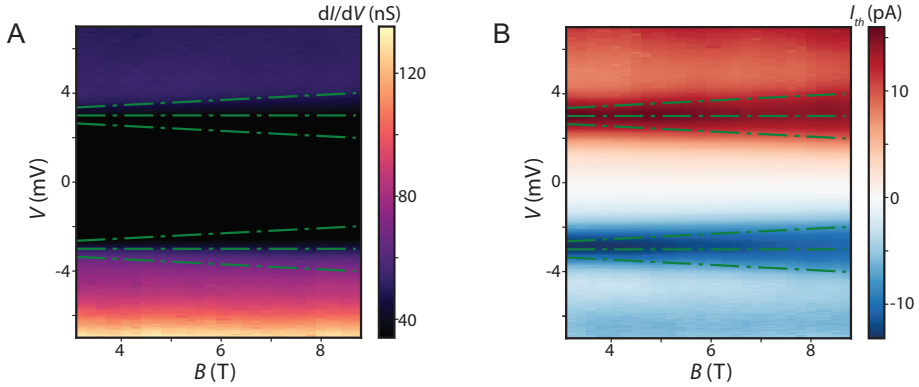

Figure 6.7: a,b. Investigation of IETS signal with magnetic field at $V_G = -4.15$. Differential conductance (a) of the peaks are broadening with the increase of the magnetic field. At the same time the maximum/minimum peak of thermocurrent (b) remains constant. Due to the temperature smearing the transitions from the ground to excited state are not distinguishable. The dotted green lines correspond to the Zeeman shifts (g=2) of the singlet to triplet excitations.

do not see a clear splitting of the excitation. The broadening of the signal reaches 0.9 meV at the highest applied magnetic field of 9 T. At the same time, for the base temperature $3k_BT \approx 0.45$ meV which would give the same broadening of around 0.9 meV. To reveal the transitions a lower base temperature or a higher magnetic field is thus required. However, considering $S = \frac{1}{2}$ on the right part of the CDP, the moving of the charge degeneracy point to the more positive gate voltages indicates that the ground state is singlet and the excited state is triplet (see dotted lines in the corresponding figures).

6.6.4. CONFIGURATION 1: CDP VS. B

We performed zero-bias gate traces for different magnetic fields up to 9 T. Differential conductance and thermocurrent as a function of gate voltage for the different magnetic fields are depicted in figures 6.8a and 6.8b. Here, we indicate the trace at 0 T with blue color and the trace at 8.8 T with yellow. The differential conductance decreases in value with increasing field and moves to less negative gate values. At the same time, the thermocurrent almost does not change with just a small change of amplitude and asymmetry. From this data, taking into account that by adding one electron to the system we change the spin of the ground state by 1/2 and that the CDP vs. B moves to the lower ground state spin, we conclude that on the right side of the CDP, there

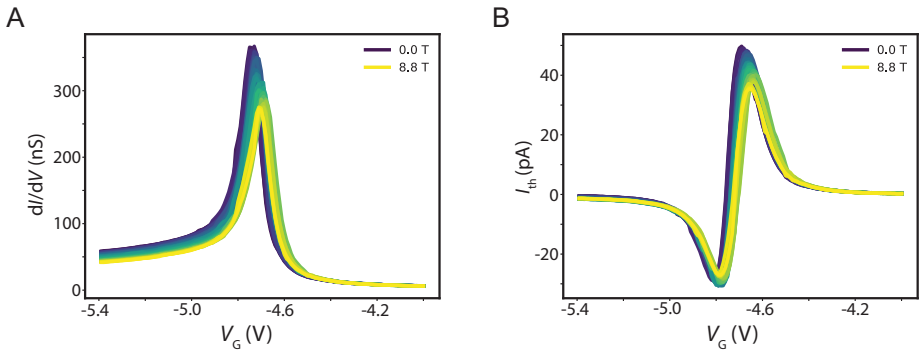

Figure 6.8: a,b. Zero-bias gate trace of differential conductance (a) and thermocurrent (b) for different magnetic fields indicating a shift of the charge degeneracy point to less negative gate voltages. Illustration of different magnetic field strengths, represented by the color of the line: blue indicates 0 T, transitioning to yellow at 8.8 T

is a singlet ground state and the interaction between radical parts is antiferromagnetic with an exchange coupling around 3 meV.

6.6.5. CONFIGURATION 2: STABILITY DIAGRAM

The dIdV and I_{th} for the second configuration are illustrated in figures 6.9a and 6.9b. We also show the response of the signal at 9 T (see figures 6.9c and 6.9d.). The dramatic difference of this configuration with respect to the first one is the much lower differential conductance and thermocurrent response that indicates a decrease of the coupling to the leads. Also, there is a blockaded region at the negative bias voltage near the drain edge of the Coulomb diamond. This blockade is not lifted with the magnetic field. The main observations are indicated as bullet points:

- CDP is around -4.4, there is one CDP in accessible gate range (-7.5 .. 7.5 V).
- It is difficult to draw the exact lines of the edges of Coulomb diamonds because of the large broadening of the signal; it is estimated that the negative diamond edge slope is 0.018, positive diamond edge slope is 0.014; gate coupling is 0.008.
- There is a broad excitation around 2-3 meV in the positive bias; the thermocurrent reveals that there is also an excitation line at negative bias between -3 and -2 meV.

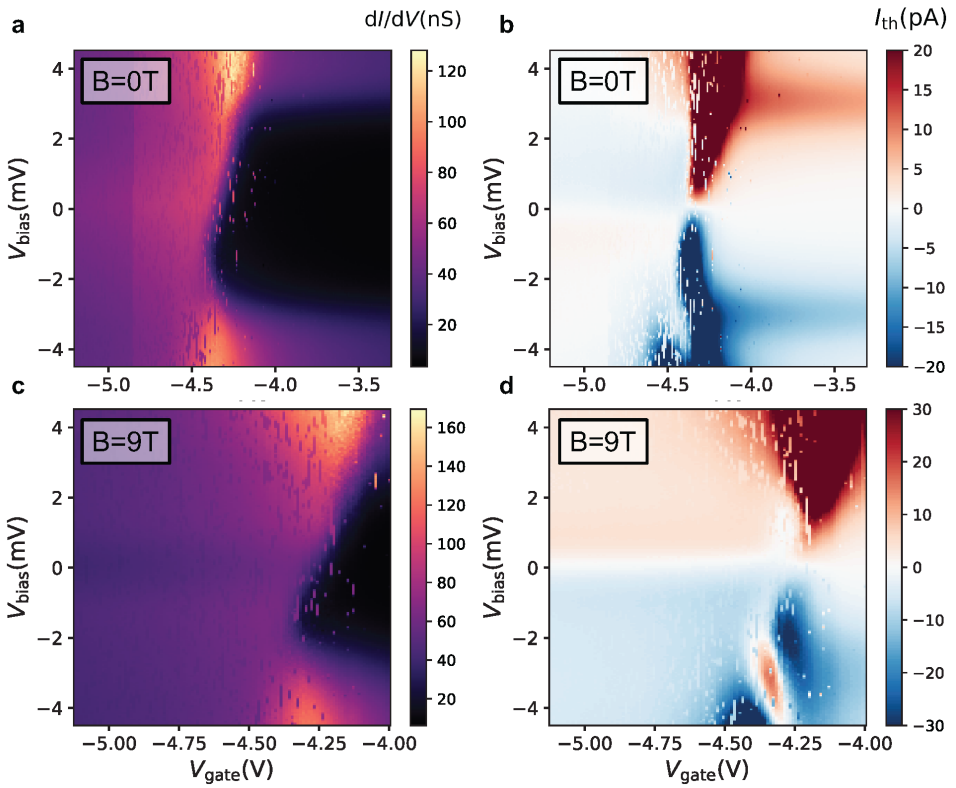

Figure 6.9: a-d.Differential conductance (a,c) and thermocurrent (b,d) measured simultaneously as a function of bias and gate voltage at different magnetic fields: 0 T (a,c), and 9 T (b,d) for configuration 2.

- $\Gamma_2 < \Gamma_1$, where '2' and '1' correspond to different configurations.
- I_{th} is positive for $V > 0$ and is negative for $V < 0$ except for the region where the excitation is present.
- Thermocurrent behaviour for the Kondo and IETS is similar to the one in configuration 1. Strikingly the amplitude of I_{th} in '1' and '2' is similar in this regions.

We would like to emphasize that an exact model is needed to explain the thermocurrent. There are some open questions related to I_{th}:

- Why do we not see any indication of a blockaded region in thermocurrent data?
- Why does the signal does not change sign in the source diamond edge?

- Why does a magnetic field change the symmetry of thermocurrent for positive and negative part?
- What is the mechanism that enhances the thermocurrent response of the excitation in the $V < 0$ part?

6.6.6. CONFIGURATION 2: KONDO AND IETS

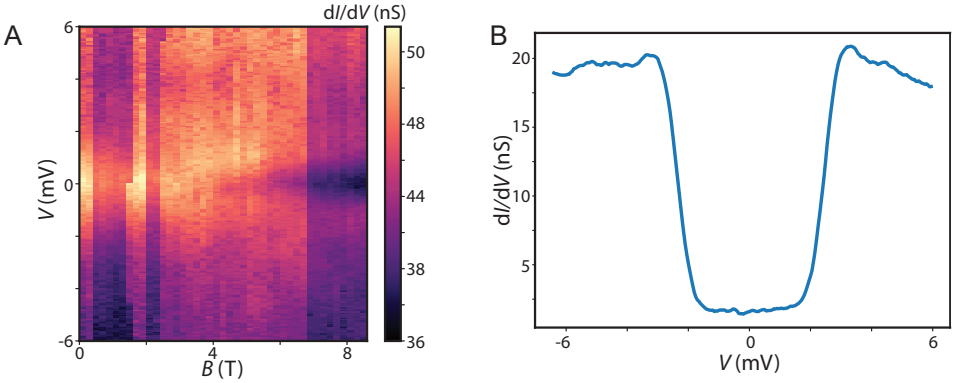

Figure 6.10: a. Differential conductance of Kondo peak as a function of magnetic field and bias voltage for configuration 2 reveals $T_K \approx 7$ K. b. IETS signal at $V_G = 4$ V at 0 T.

In figure 6.10a we present the differential conductance as a function of bias voltage and magnetic field. The data is noisy but looks comparable to figure 6.6a. The FWHM is around 2 mV, allowing us to conclude that the Kondo temperature experienced negligible changes after the molecular "jump" between configurations 1 and 2.

Meanwhile, in figure 6.10b we show the IETS signal for the second configuration. Differential conductance at $V_G = -4$ V shows a clear cotuneling peak at 3 mV with an amplitude of 50 nS (the same value we recorded for configuration 1). At -4 meV the differential conductance is also 20 nS (for configuration 1 it is 70 nS) and grows for higher negative bias voltages. At the same time, the thermocurrent is reaching its maximum of 15 pA at 3 mV and its minimum of -12 pA at -3 mV. These values match the ones recorded in configuration 1 (see figure 6.9b for a comparison of configurations 1 and 2).

6.6.7. CONFIGURATION 2: CDP VS. B

We did not perform a detailed measurement of the CDP vs. B, but from the stability diagrams at 0 and 9 T we can see that the charge degeneracy point is moving to less negative gate voltages. However,

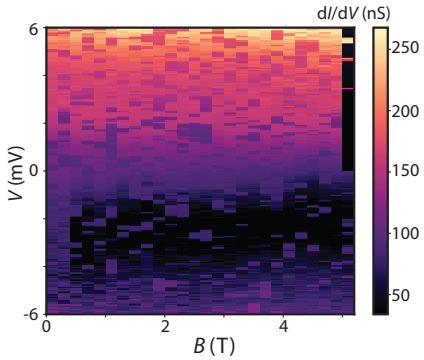

Figure 6.11: Differential conductance as a function of bias voltage and magnetic field for $V_G = -4.2$ V

this observation can not serve as a solid confirmation as from time to time large gate sweeps change the electrical surrounding of the molecule and CDP shifts can be induced. Magnetic field does not change significantly the differential conductance in blockaded region. So, by measuring IVs at constant gate voltage the suppression gap is increasing as we increase B (see figure 6.11), consistent with the movement of the CDP to the left.

6.6.8. TRANSPORT INTERPRETATION

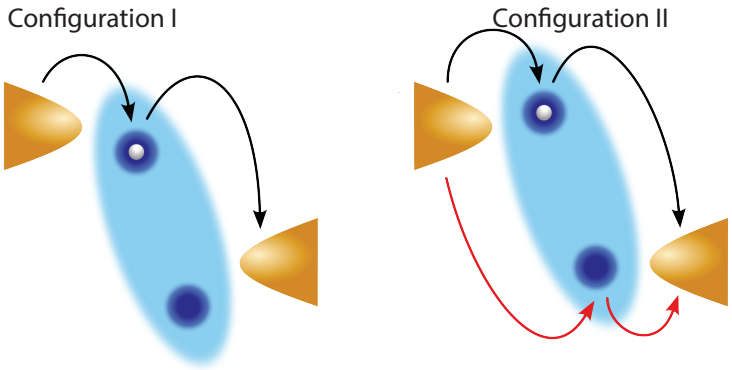

Figure 6.12: Proposed model for explaining the current features in configurations 1 and 2.

Here, we provide a possible explanation for the transport features in the system. The schematic representation of this hypothesis is depicted

in figure 6.12. In configuration 1, the molecule location mainly allows for transport through one radical part. The molecule is asymmetrically coupled to the leads, such that $\Gamma_1 = \Gamma_S + \Gamma_D \approx \Gamma_S$. On the left side of CDP, there is one electron less on the molecule, a doublet. This doublet changes to a singlet once an electron is added to the system by changing the gate voltage. This explanation would be consistent with the $S = 1/2$ Kondo effect on the left and IETS with an antiferromagnetic ground state on the right from CDP.

When the molecule rearranges to configuration 2, the second radical part starts participating in transport. The coupling to the leads of the first radical part becomes weaker and lifts the high asymmetry in a way that $\Gamma_2 < \Gamma_1$, $\Gamma_{2S} \sim \Gamma_{2D}$. Most likely, the electron configuration of the molecule is the same as in configuration 1 (i.e., 1 electron less on the left side, and neutral on the right side of CDP) with the same doublet to singlet transition induced by the gate voltage. However, this time there is also hoping of electrons between the second radical part and the leads and between the radical parts of the molecule. In this picture for a specific range of couplings it is possible to have a current suppressed region in the stability diagram (see [44]). It is not clear how the thermocurrent would be in this case; further theoretical calculations are needed. The possibility of the spin blockade origin (see [45]) should also not be ruled out.

REFERENCES

[1] C. Forman, I. K. Muritala, R. Pardemann, and B. Meyer. “Estimating the global waste heat potential”. *Renewable and Sustainable Energy Reviews* 57 (2016), pp. 1568–1579.

[2] Q. Bian. “Waste heat: the dominating root cause of current global warming”. *Environmental Systems Research* 9.1 (May 2020), p. 8.

[3] T. Humphrey and H. Linke. “Quantum, cyclic, and particle-exchange heat engines”. *Physica E: Low-dimensional Systems and Nanostructures* 29.1 (2005). Frontiers of Quantum, pp. 390–398.

[4] H. E. D. Scovil and E. O. Schulz-DuBois. “Three-Level Masers as Heat Engines”. *Phys. Rev. Lett.* 2 (6 Mar. 1959), pp. 262–263.

[5] T. E. Humphrey and H. Linke. “Reversible Thermoelectric Nanomaterials”. *Phys. Rev. Lett.* 94 (9 Mar. 2005), p. 096601.

[6] P. Li and B. Jia. “Particle-exchange heat engine working between bosonic and fermionic reservoirs”. *Phys. Rev. E* 83 (6 June 2011), p. 062104.

[7] G. Germanese, F. Paolucci, G. Marchegiani, A. Braggio, and F. Giazotto. “Bipolar thermoelectric Josephson engine”. *Nature Nanotechnology* 17.10 (Oct. 2022), pp. 1084–1090.

[8] K. Ono, S. N. Shevchenko, T. Mori, S. Moriyama, and F. Nori. “Analog of a Quantum Heat Engine Using a Single-Spin Qubit”. *Phys. Rev. Lett.* 125 (16 Oct. 2020), p. 166802.

[9] V. Blickle and C. Bechinger. “Realization of a micrometre-sized stochastic heat engine”. *Nature Physics* 8.2 (Feb. 2012), pp. 143–146.

[10] C. I. L. d. Araujo, P. Virtanen, M. Spies, C. González-Orellana, S. Kerschbaumer, M. Ilyn, C. Rogero, T. T. Heikkilä, F. Giazotto, and E. Strambini. “Superconducting spintronic heat engine”. *Nature Communications* 15.1 (June 2024), p. 4823.

[11] J.-P. Brantut, C. Grenier, J. Meineke, D. Stadler, S. Krinner, C. Kollath, T. Esslinger, and A. Georges. “A Thermoelectric Heat Engine with Ultracold Atoms”. *Science* 342.6159 (2013), pp. 713–715.

[12] M. Josefsson, A. Svilans, A. M. Burke, E. A. Hoffmann, S. Fahlvik, C. Thelander, M. Leijnse, and H. Linke. “A quantum-dot heat engine operating close to the thermodynamic efficiency limits”. *Nature Nanotechnology* 13.10 (Oct. 2018), pp. 920–924.

[13] M. Josefsson, A. Svilans, H. Linke, and M. Leijnse. “Optimal power and efficiency of single quantum dot heat engines: Theory and experiment”. *Phys. Rev. B* 99 (23 June 2019), p. 235432.

[14] S. Verma and A. Singh. “A Strongly Correlated Quantum Dot Heat Engine with Optimal Performance: A Nonequilibrium Green’s Function Approach”. *physica status solidi (b)* 260.6 (2023), p. 2200608.

[15] W. Si, J. Li, G. Li, C. Jia, and X. Guo. “Single-molecule non-volatile memories: an overview and future perspectives”. *J. Mater. Chem. C* 12 (3 2024), pp. 751–764.

[16] A. Moneo-Corcuera, D. Nieto-Castro, J. Cirera, V. Gómez, J. Sanjosé-Orduna, C. Casadevall, G. Molnár, A. Bousseksou, T. Parella, J. M. Martínez-Agudo, J. Lloret-Fillol, M. H. Pérez-Temprano, E. Ruiz, and J. R. Galán-Mascarós. “Molecular memory near room temperature in an iron polyanionic complex”. *Chem* 9.2 (Feb. 2023), pp. 377–393.

[17] B. Xu and Y. Dubi. “Negative differential conductance in molecular junctions: an overview of experiment and theory”. *Journal of Physics: Condensed Matter* 27.26 (June 2015), p. 263202.

[18] A. S. Zyazin, J. W. G. van den Berg, E. A. Osorio, H. S. J. van der Zant, N. P. Konstantinidis, M. Leijnse, M. R. Wegewijs, F. May, W. Hofstetter, C. Danieli, and A. Cornia. “Electric Field Controlled Magnetic Anisotropy in a Single Molecule”. *Nano Letters* 10.9 (Sept. 2010), pp. 3307–3311. issn: 1530-6984.

[19] M. Misiorny, E. Burzurí, R. Gaudenzi, K. Park, M. Leijnse, M. R. Wegewijs, J. Paaske, A. Cornia, and H. S. J. van der Zant. “Probing transverse magnetic anisotropy by electronic transport through a single-molecule magnet”. *Phys. Rev. B* 91 (3 Jan. 2015), p. 035442.

[20] H. B. Heersche, Z. de Groot, J. A. Folk, H. S. J. van der Zant, C. Romeike, M. R. Wegewijs, L. Zobbi, D. Barreca, E. Tondello, and A. Cornia. “Electron Transport through Single Mn_{12} Molecular Magnets”. *Phys. Rev. Lett.* 96 (20 May 2006), p. 206801.

[21] J. de Bruijckere, P. Gehring, M. Palacios-Corella, M. Clemente-León, E. Coronado, J. Paaske, P. Hedegård, and H. S. J. van der Zant. “Ground-State Spin Blockade in a Single-Molecule Junction”. *Phys. Rev. Lett.* 122 (19 May 2019), p. 197701.

[22] P. Reddy, S.-Y. Jang, R. A. Segalman, and A. Majumdar. “Thermoelectricity in Molecular Junctions”. *Science* 315.5818 (Mar. 2007), pp. 1568–1571.

[23] P. Gehring, J. K. Sowa, C. Hsu, J. de Bruijckere, M. van der Star, J. J. Le Roy, L. Bogani, E. M. Gauger, and H. S. J. van der Zant. “Complete mapping of the thermoelectric properties of a single molecule”. *Nature Nanotechnology* 16.4 (Apr. 2021), pp. 426–430.

[24] A. Gemma, F. Tabatabaei, U. Drechsler, A. Zulji, H. Dekkiche, N. Mosso, T. Niehaus, M. R. Bryce, S. Merabia, and B. Gotsmann. “Full thermoelectric characterization of a single molecule”. *Nature Communications* 14.1 (June 2023), p. 3868.

[25] L. Cui, R. Miao, C. Jiang, E. Meyhofer, and P. Reddy. “Perspective: Thermal and thermoelectric transport in molecular junctions”. *The Journal of Chemical Physics* 146.9 (Mar. 2017), p. 092201.

[26] P. Murphy, S. Mukerjee, and J. Moore. “Optimal thermoelectric figure of merit of a molecular junction”. *Phys. Rev. B* 78 (16 Oct. 2008), p. 161406.

[27] M. Strange, J. S. Seldenthuis, C. J. O. Verzijl, J. M. Thijssen, and G. C. Solomon. “Interference enhanced thermoelectricity in quinoid type structures”. *The Journal of Chemical Physics* 142.8 (Feb. 2015), p. 084703.

[28] C. J. Lambert, H. Sadeghi, and Q. H. Al-Galiby. “Quantum-interference-enhanced thermoelectricity in single molecules and molecular films”. *Comptes Rendus Physique* 17.10 (2016). Mesoscopic thermoelectric phenomena / Phénomènes thermoélectriques mésoscopiques, pp. 1084–1095.

[29] J. P. Bergfield, M. A. Solis, and C. A. Stafford. “Giant Thermoelectric Effect from Transmission Supernodes”. *ACS Nano* 4.9 (2010), pp. 5314–5320.

[30] R. Miao, H. Xu, M. Skripnik, L. Cui, K. Wang, K. G. L. Pedersen, M. Leijnse, F. Pauly, K. Wärnmark, E. Meyhofer, P. Reddy, and H. Linke. “Influence of Quantum Interference on the Thermoelectric Properties of Molecular Junctions”. *Nano Letters* 18.9 (Sept. 2018), pp. 5666–5672.

[31] A. Manaparambil and I. Weymann. “Nonequilibrium Seebeck effect and thermoelectric efficiency of Kondo-correlated molecular junctions”. *Phys. Rev. B* 107 (8 Feb. 2023), p. 085404.

[32] S. Andergassen, T. A. Costi, and V. Zlati ć. “Mechanism for large thermoelectric power in molecular quantum dots described by the negative-*U* Anderson model”. *Phys. Rev. B* 84 (24 Dec. 2011), p. 241107.

[33] C. M. Finch, V. M. García-Suárez, and C. J. Lambert. “Giant thermopower and figure of merit in single-molecule devices”. *Phys. Rev. B* 79 (3 Jan. 2009), p. 033405.

[34] R. M. Al-Utayjawee and O. A. Al-Owaedi. “Enhancement of Thermoelectric Properties of Porphyrin-based Molecular Junctions by Fano Resonances”. *Journal of Physics: Conference Series* 1818.1 (Mar. 2021), p. 012208.

[35] P. Gehring, M. van der Star, C. Evangeli, J. J. Le Roy, L. Bogani, O. V. Kolosov, and H. S. J. van der Zant. “Efficient heating of single-molecule junctions for thermoelectric studies at cryogenic temperatures”. *Applied Physics Letters* 115.7 (Aug. 2019), p. 073103.

[36] K. O’Neill, E. A. Osorio, and H. S. J. van der Zant. “Self-breaking in planar few-atom Au constrictions for nanometer-spaced electrodes”. *Applied Physics Letters* 90.13 (Mar. 2007), p. 133109.

[37] A. Vegliante, S. Fernandez, R. Ortiz, M. Vilas-Varela, T. Baum, N. Friedrich, F. Romero-Lara, A. Aguirre, K. Vaxevani, D. Wang, C. Garcia, H. S. J. van der Zant, T. Frederiksen, D. Peña, and J. I. Pascual. “Tuning the Spin Interaction in Non-planar Organic Diradicals Through Mechanical Manipulation”. *arXiv* (2024). arXiv: 2402.08641.

[38] R. Frisenda, S. Tarkuç, E. Galán, M. L. Perrin, R. Eelkema, F. C. Grozema, and H. S. J. van der Zant. “Electrical properties and mechanical stability of anchoring groups for single-molecule electronics”. *Beilstein J Nanotechnol* 6 (2015), pp. 1558–1567.

[39] T. Baum. “Electronic transport signatures of two-electron interactions in all-organic single-molecule junctions”. PhD. thesis. Delft, The Netherlands: TU Delft, 2024.

[40] J. M. Thijssen and H. S. J. Van der Zant. “Charge transport and single-electron effects in nanoscale systems”. *physica status solidi (b)* 245.8 (2008), pp. 1455–1470.

[41] G. D. Scott and D. Natelson. “Kondo Resonances in Molecular Devices”. *ACS Nano* 4.7 (July 2010), pp. 3560–3579.

[42] C. Hsu, T. A. Costi, D. Vogel, C. Wegeberg, M. Mayor, H. S. J. van der Zant, and P. Gehring. “Magnetic-Field Universality of the Kondo Effect Revealed by Thermocurrent Spectroscopy”. *Phys. Rev. Lett.* 128 (14 Apr. 2022), p. 147701.

[43] B. Dutta, J. T. Peltonen, D. S. Antonenko, M. Meschke, M. A. Skvortsov, B. Kubala, J. König, C. B. Winkelmann, H. Courtois, and J. P. Pekola. “Thermal Conductance of a Single-Electron Transistor”. *Phys. Rev. Lett.* 119 (7 Aug. 2017), p. 077701.

[44] G. A. Kaat and K. Flensberg. “Rectification in single molecular dimers with strong polaron effect”. *Phys. Rev. B* 71 (15 Apr. 2005), p. 155408.

[45] D. Weinmann, W. Häusler, and B. Kramer. “Spin Blockades in Linear and Nonlinear Transport through Quantum Dots”. *Phys. Rev. Lett.* 74 (6 Feb. 1995), pp. 984–987.

7

IMPACT OF SPIN-ENTROPY ON THE THERMOELECTRIC PROPERTIES OF A 2D MAGNET

Heat-to-charge conversion efficiency of thermoelectric materials is closely linked to the entropy per charge carrier. Thus, magnetic materials are promising building blocks for highly efficient energy harvesters, as their carrier entropy is boosted by a spin degree of freedom. In this work, we investigate how this spin entropy impacts heat-to-charge conversion in A-type antiferromagnet CrSBr. We perform simultaneous measurements of electrical conductance and thermocurrent while changing magnetic order using temperature and magnetic field as tuning parameters. We find a strong enhancement of the thermoelectric power factor around the Nèel temperature. We further reveal that the power factor at low temperature can be increased by up to 600% upon applying a magnetic field. Our results demonstrate that the thermoelectric properties of 2D magnets can be optimized by exploiting the sizeable impact of spin entropy and confirm thermoelectric measurements as a sensitive tool to investigate subtle magnetic phase transitions in low-dimensional magnets.

Parts of this chapter have been published in Nano Letters, **24(22)**, 6513-6520 (2024) [1].

7.1. INTRODUCTION

The Seebeck coefficient (α) quantifies the electromotive force or gradient of the electrochemical potential $\nabla V = \nabla\tilde{\mu}/q$ developing in a material exposed to a temperature gradient ∇T (figure 7.1), and is the central parameter that determines the efficiency of a thermoelectric device [2, 3]. As the electrochemical potential $\tilde{\mu}$ of a population of electrically charged particles consists of the sum of the chemical potential μ and the electrostatic contribution $q\varphi$, the Seebeck coefficient can be written as [4]:

$$\alpha = -\frac{\partial\tilde{\mu}}{q\partial T} = -\frac{\partial\mu}{q\partial T} - \frac{\partial\varphi}{\partial T}, \tag{7.1}$$

where q is the elementary charge. The second term of equation 7.1, often referred to as effective Seebeck coefficient, contains dynamical effects linked to scattering/carrier relaxation processes [4, 5]. In contrast, the first component – known as the Kelvin formula [6, 7] – is purely thermodynamic. On the basis of thermodynamic considerations for an electronic system, this term is directly related to the average entropy transported per charge carrier [2, 8] using the Maxwell equation $\left(\frac{\partial\mu}{\partial T}\right)_N = -\left(\frac{\partial S}{\partial N}\right)_T$, where N is the mean time-averaged population of the system and S is the electronic entropy [8–10]. This implies that mechanisms that increase the entropy per carrier can enhance the Seebeck coefficient. In particular, the spin degrees of freedom of carriers in magnetic materials can lead to such increased entropy [8, 11–13]. Figure 7.1 illustrates this concept by comparing the Seebeck effect of an antiferromagnet in three temperature regimes, linked to different magnetic phases. In all cases, under open-circuit conditions, a thermally driven diffusion current of charge carriers (red arrows) from the heated region (depicted in orange) to the cold one (in blue) is balanced by a drift current generated by an electric field that builds up inside the material. Moreover, the so-called *spin-entropy*, S_m, in magnetic materials can contribute to their Seebeck effect (bottom panels of figure 7.1) [2, 8]. S_m is minimum below the "spin freezing" temperature (figure 7.1a, a special magnetic state in CrSBr, see discussion below). Thermal fluctuations will then increase S_m (figure 7.1b) and it reaches its maximum above the phase transition temperature, as the material enters the paramagnetic state (figure 7.1c) [2].

In this context, thanks to their controllable magnetism [14–17], two-dimensional (2D) magnets provide an ideal platform to test this effect. Among the layered van der Waals (vdW) materials A-type antiferromagnet CrSBr stands out for its good cleavability as well as its Nèel temperature T_N of 132 K, one of the highest reported among vdW antiferromagnets [15, 18]. Compared to ferromagnets, AFM materials offer the possibility to change their spin structure into

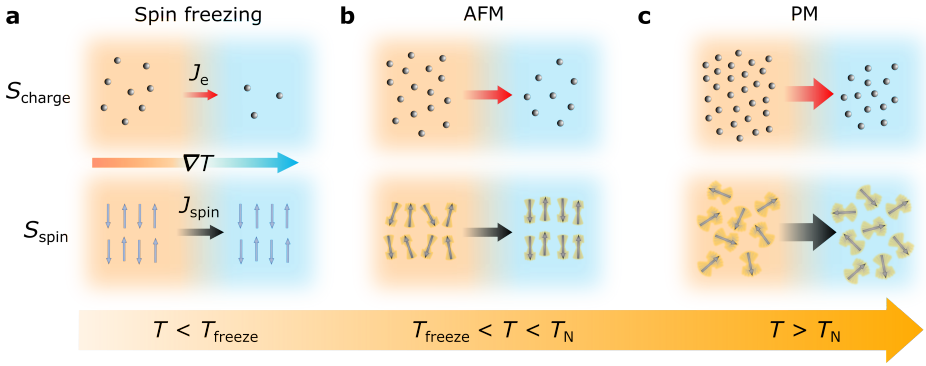

Figure 7.1: Seebeck effect in non-magnetic and magnetic materials. Schematic illustrating the working principle of the Seebeck effect in a material at different magnetic phases. The three images refer to different temperature ranges and consequently magnetic phases: "spin freezing" state (a), antiferromagnetic state (b) and paramagnetic state (c). The top pictures show the thermally-driven diffusion of the charge carriers, of which direction and magnitude are qualitatively indicated by the red arrows. The bottom images show the additional contribution of the spin entropy (S_m) to the Seebeck coefficient. Direction and magnitude of the entropy flow are qualitatively indicated by the black arrows [2, 8]. Temperature ranges are indicated in the large orange arrow at the bottom of the figure, while, in a), the direction of the temperature gradient is illustrated by an orange-to-blue arrow.

a field-induced FM configuration upon the application of an external magnetic field, adding a degree of freedom in tuning the electronic and thermoelectric properties [19, 20]. Each CrSBr van der Waals layer consists of two fused buckled planes of CrS, sandwiched between Br atoms and stacked along the c axis (see figure 7.2a) [15, 18]. CrSBr is an A-type antiferromagnet, with intralayer ferromagnetic (FM) coupling and interlayer antiferromagnetic (AFM) interaction, and with easy/medium/hard axis coinciding with the crystallographic b/a/c axes, respectively [21]. Furthermore, CrSBr shows semiconducting transport properties, with a direct bandgap of E_G = 1.5 eV and finite electrical conductivity at low temperature [19]. In particular, thanks to the strong coupling between magnetic ordering and transport properties in CrSBr, an external magnetic field can be used to alter the electrical resistance, which tends to decrease as the field increases. This comes as a consequence of the reduction of spin fluctuations, and the different

interlayer spin-flip scattering between AFM and FM configurations [18, 19, 21, 22]. While the electrical transport and magnetic properties of this material have been extensively investigated [18, 19, 21–23], the effect of magnetic order on the entropy and thus the thermoelectric properties has not been reported to date.

In this chapter we study the impact of electron and spin entropy on the thermoelectric properties of CrSBr thin flakes. To this end, we change magnetic order by varying the sample temperature or by applying an external magnetic field, while simultaneously measuring the electrical and thermoelectric transport properties. We observe a steep increase of the Seebeck coefficient and the thermoelectric power factor with increasing temperature as electrons and spins mobilize, with a local maximum slightly below T_N which we explain by a competition between electronic band entropy and magnetic entropy in CrSBr. We further reveal that a magnetic field can enhance the power factor by up to 600% at low temperatures. These findings highlight how spin-entropy engineering in 2D magnetic materials could be used to realize thermoelectric heat engines with strongly enhanced performance.

7.2. RESULTS

To measure the electrical and thermoelectric properties of CrSBr thin flakes we employ a device architecture (figure 7.2b-c) that was recently developed for thermoelectric experiments on single molecule junctions [24, 25]. It consists of pre-patterned contacts, thermometers and microheaters on top of which a CrSBr flake has been stamped using a dry transfer method (see appendix). A thin hBN flake is used to encapsulate CrSBr to prevent degradation and contamination. An optical micrograph of the final device is shown in figure 7.2d. For a typical measurement (figure 7.2c), an AC current $\tilde{I}_h$ at frequency ω_1 is applied to the microheater which generates a temperature bias ΔT proportional to $\tilde{I}_h^2$, therefore having frequency $2\omega_1$. Simultaneously, an AC voltage $\tilde{V}_{sd}$ at frequency $\omega_2 \gg \omega_1$ is applied to the drain contact. The current to ground on the source contact is then demodulated at frequencies ω_2 and $2\omega_1$ to extract the differential conductance $G = \tilde{I}_{sd}/\tilde{V}_{sd}$ and the Seebeck coefficient $\alpha = -\frac{\tilde{V}_{th}}{\Delta T} = -\frac{\tilde{I}_{th}}{G\Delta T}$ (see appendix for details on the temperature calibration), respectively. All magnetic fields in this study were applied parallel to the a (medium) axis of CrSBr.

Figure 7.2e illustrates the temperature dependence of G and of $\frac{d^2G}{dT^2}$, respectively. G decreases when lowering T, typical for semiconducting materials and in good agreement with previous studies [18, 19, 22]. Furthermore, we observe a maximum in G and a sharp dip in $\frac{d^2G}{dT^2}$ around 133 ± 1 K. We associate this value with the Nèel temperature T_N, where the transition from the paramagnetic (PM) state (white region) to

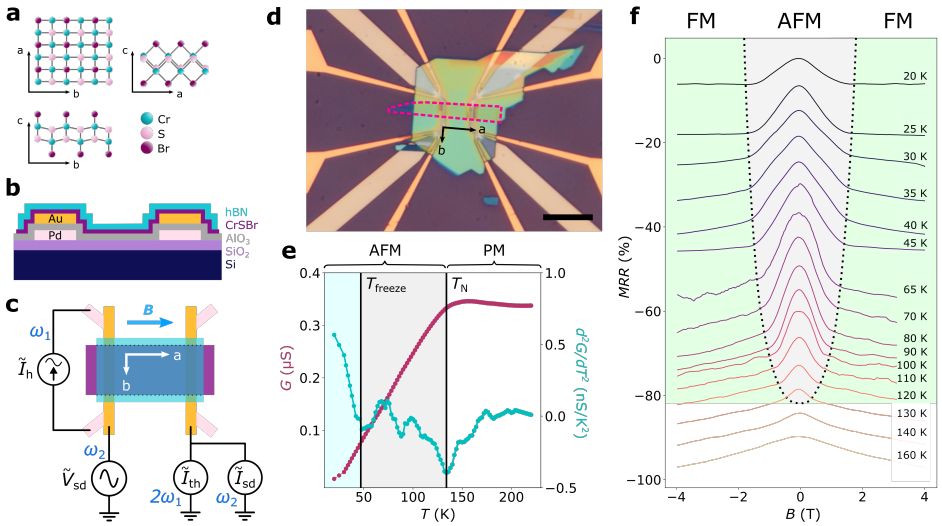

Figure 7.2: Crystal structure, measurement setup, and electrical transport of CrSBr. a. Crystal structure of CrSBr, from the c axis (top left), a axis (top right) and b axis (bottom). Cr, S and Br atoms are represented as cyan, pink and purple spheres, respectively. b. Side view of the schematic of the device. c. Schematic of the setup used for magnetotransport and thermoelectric measurements. d. Optical image of the measured device. The magenta dashed guideline highlights the position of the CrSBr flake, covered by the hBN layer. e. Temperature dependence of the conductance G (purple) and the second derivative of the conductance (cyan). The white region and the light blue/grey region correspond respectively to the paramagnetic (PM) and antiferromagnetic (AFM) phases of CrSBr. f. Magnetoresistance ratio (MRR) versus the applied magnetic field B at different temperatures between 20 and 160 K. An offset of 6% is applied for clarity between each pairs of curves. The AFM and FM magnetic phases are shaded grey and green, respectively. The black dotted line defines the saturation field H_S. Scale bar in (d): 10 μm.

antiferromagnetic (AFM) (grey region) occurs [11, 18, 19, 23, 26]. Upon further lowering T, G drops by one order of magnitude between T_N and 20 K [22]. At temperatures lower than $T_{freeze} = 47 \pm 2\ K$ the appearance of a low-temperature magnetic hidden order has been reported [19,

23, 27]. We do not observe changes in G around T_{freeze}, however, as we will show later, the Seebeck coefficient changes abruptly below this temperature. G values depicted in figure 7.2e are in good agreement with the conductance reported in previous works ([18, 19]).

In figure 7.2f we show the magneto-resistance ratio $MRR = \frac{R(B)-R(B=0)}{R(B=0)} \cdot 100$ at different temperatures between 20 and 160 K (measurements on additional CrSBr devices can be found in the Supplementary Information section S7 in Ref. [1]). Below T_N, for low magnetic fields, spins are coupled antiferromagnetically between layers and aligned along the b (easy) axis (see grey area). As reported previously, this suppresses the interlayer tunneling, and thus leads to an increase in electrical resistance [18, 19]. By raising the applied magnetic field, spins tend to cant: This re-enables interlayer tunneling and therefore lowers the resistance [18, 19, 28]. Saturation of the MRR is visible when ferromagnetic order between the layers is established (see green area) [18].

Figure 7.3a shows the temperature dependence of the Seebeck coefficient simultaneously measured with $G(T)$ (figure 7.2e). The negative sign of α is consistent with the n-type doping typically found in CrSBr, which is attributed to Br vacancies [18, 29]. We observe an overall decrease from -265 μV/K to -9 μV/K when cooling the sample from 200 K to 20 K, which is the base temperature of our experiment. Three areas have been highlighted by means of different colors. In the white region ($T > T_N$), corresponding to the paramagnetic phase, $|\alpha|$ increases as T decreases. $|\alpha|$ reaches its maximum at T_N, stays constant until $T \approx 90$ K, then decreases (overall about 45%) until T_{freeze} (grey region). When cooling below T_{freeze} (light blue area), $|\alpha|$ decreases faster – as can be seen in the first derivative $d\alpha/dT$ (cyan curve) – down to the value of -9 μV/K at 20 K. To explain this behaviour, we performed first principles calculations within the constant relaxation time approximation [30], for a doping of $\sim 8.10^{18}$ electrons per cm^3 (see Supplementary Information Fig. S8 in Ref. [1]). In figure 7.3b we compare the AFM ground state, a collinear PM state (averaging special quasirandom structures [31]), and an interpolation between the two [32]. The calculations are in good quantitative agreement at low and intermediate temperatures, show the same qualitative extremum and upturn around T_N, but underestimate the upward jump of α in the fully PM phase. Calculation of the bands in a collinear paramagnetic state produces a smaller Seebeck amplitude (less negative). Freeing the spins to be non collinear PM should produce even more phase space and entropy for the spins, and therefore a larger jump. It should be noted that this first principle model is not suitable to predict $\alpha(T)$ at $T < 50$ K. In this regime, a strong modulation of the carrier concentration is expected which is not accounted for in the calculations.

To gain further evidence for the impact of magnetic order on the

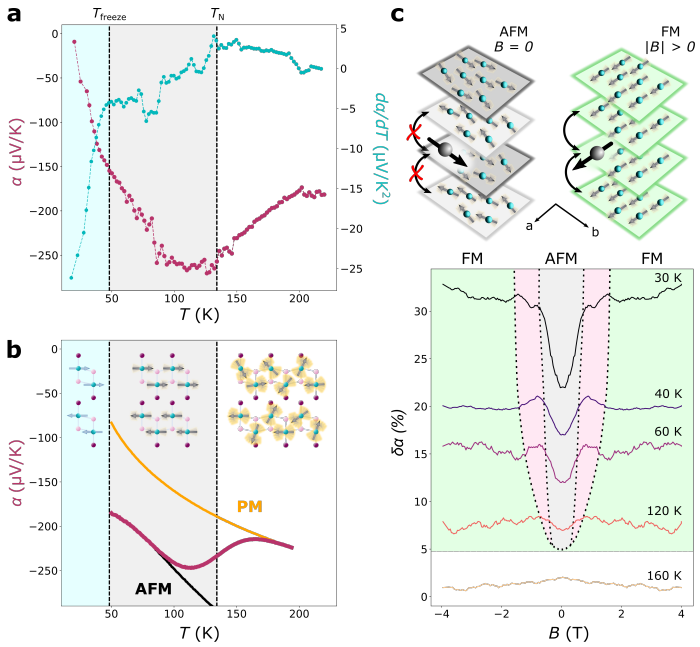

Figure 7.3: Magnetic field and temperature dependence of the Seebeck coefficient of CrSBr. a. Variation of the Seebeck coefficient (purple curve) and its first derivative (cyan curve) at $B = 0T$ as a function of temperature. The temperatures T_N and T_{freeze} separate the graph in three areas, colored respectively in white, grey and light blue. b. First principles Seebeck coefficient as a function of T, for a representative (n-type) doping level, calculated in the AFM (black curve), PM (orange curve), and interpolated magnetic states (purple curve). c. Magneto-Seebeck coefficient as a function of temperature. Each curve is offset by 5% for clarity, and averaged as $\frac{\delta\alpha(B)+\delta\alpha(-B)}{2}$ in order to remove any parasitic effect due to drift in the measurement. The three regions - AFM, transition/canting, FM - are depicted in green, pink and grey, respectively. The field-dependent spin reorientation and interlayer tunneling is illustrated in the top part of the image. The orientation of the crystallographic axes is also reported. An electron residing on one of the layers (dark grey sphere) can tunnel (indicated by the black curved arrows) or not (indicated by the black curved arrows with red X) depending on its spin orientation.

thermoelectric properties of CrSBr, we measured the change in Seebeck coefficient as a function of the applied magnetic field. Figure 7.3c shows this magneto-Seebeck coefficient ratio $\delta\alpha = \frac{\alpha(B)-\alpha(B=0)}{\alpha(B=0)} \cdot 100$ versus magnetic field B at temperatures varying between 20 K and 160 K. At 160 K, the flake is in a paramagnetic state and the curve shows almost no variation with applied B field. Below T_N and for small magnetic fields, CrSBr is AFM ordered (grey area) and $\delta\alpha$ is minimum at $B = 0$ T. As the absolute value of B becomes larger, $\delta\alpha$ increases and reaches a local maximum, then decreases until saturating when FM order is established (green area). The areas including the local maxima of $\delta\alpha$ (in pink) can be identified as transition regions, in which the spins are canting from a to b direction due to the application of external B field [23]. We observe an increase in $\delta\alpha$ of up to 13% at low T when changing from AFM to FM order.

Figure 7.4a displays the temperature-dependent power factor $PF = \alpha^2 \cdot \sigma$, where σ is the electrical conductivity of CrSBr. As part of the figure of merit zT, the power factor helps quantifying the energy harvesting efficiency of the material. As it is also proportional to the maximum achievable output power, it is a useful parameter for quantifying Peltier cooling. At $B = 0$, PF shows a peak of 7 μW m^{-1} K^{-2} around T_N, where also the maxima of G and α simultaneously occur. This peak increases in magnitude and shifts to lower temperatures when a magnetic field of $B = 4$ T is applied. Figure 7.4b shows the Magneto-power factor $\delta PF = \frac{PF(B=4\text{T})-PF(B=0)}{PF(B=0)\cdot 100}$ as a function of temperature. We observe that the relative change δPF increases with decreasing temperature and reaches values up to 600% at 20K (see Supplementary Information Fig. S7 in Ref. [1]). Below we will discuss that these findings can be explained by the intrinsic band structure of AFM CrSBr, taking into account variations in the entropy linked to the magnetic order.

7.3. DISCUSSION

As we described at the beginning of this chapter, the Seebeck coefficient is closely linked to the entropy S of the system (see equation 7.1) [9, 33]. The entropy of a mesoscopic system can be estimated using the Boltzmann formula $S = k_B \ln(\Omega)$, where Ω represents the number of all possible microstates of the system [2, 34]. Here, we assume that Ω contains three main contributions. Ω_p represents the conventional distribution of momenta of the electron gas (electronic band contribution). Then, we take into account a layer degree of freedom Ω_{layer} which quantifies the number of layers a charge carrier can access, as CrSBr is a layered vdW material in which interlayer tunneling is precluded when switching to AFM order [35]. Lastly, we include a term Ω_s representing all possible spin configurations, which

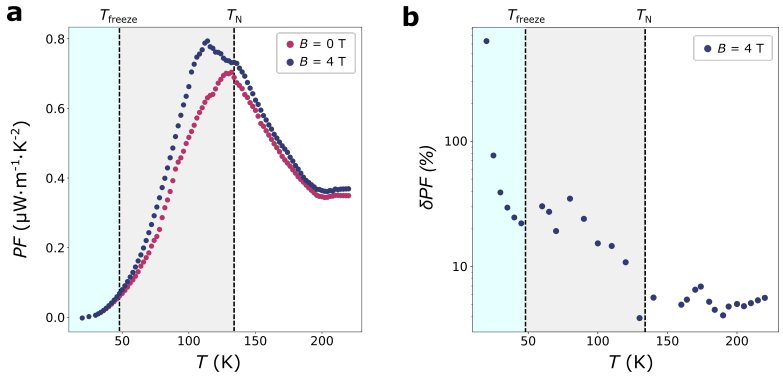

Figure 7.4: Field and temperature dependence of the power factor. a. Temperature dependent power factor, for $B = 0T$ (purple) and $B = 4T$ (blue). b. Magneto-power factor (δPF) as a function of temperature, measured at $B = 4T$.

yields the spin-entropy S_m [36]. The sign of this contribution depends on the nature of the d bands hosting the magnetization, which is positive in CrSBr (hole like, from the d band valence electrons) [2]. Therefore, the electronic and spin entropy contributions have opposite signs. We now turn back to figure 7.3a, that depicts the temperature dependence of α. As $T \geq T_{freeze}$, the growth of the Seebeck coefficient abruptly slows down, which is simultaneous with the appearance of a magnetic hidden order below T_{freeze}. Such hidden order was already observed previously by other groups, who associate its origin either to a magnetic coupling between self-trapped defects [19], the anisotropic structure of CrSBr – which can be seen as weakly and incoherently coupled 1D chains [22], or a spin-dimensionality crossover caused by a slowing down of the magnetic fluctuations (spin freezing) [23, 27]. The consequence of the spin freezing phenomenon is that spin fluctuations are fully suppressed ($\Omega_s = 1$) below T_{freeze}, and therefore cannot contribute to the entropy [23] to counteract the electronic α [2]. Additionally, interlayer tunneling is suppressed ($\Omega_{layer} = 1$) [22, 23, 27]. As the spins mobilize upon heating, their contribution S_m is superimposed on the intrinsic electronic α. Due to the opposite signs of the electronic and spin entropy contributions, their combined action leads to a plateau and turnover when increasing T. At higher temperatures ($T \sim T_N$), two effects cause the reduction in $|\alpha|$ observed in our experiment: Firstly, fluctuations and S_m increase as CrSBr approaches T_N, then saturate in the fully paramagnetic phase [11, 37]; secondly, an increase in carrier concentration decreases the magnitude of α (less negative, see Supplementary Information Fig. S8 in Ref. [1]). The subsequent increase

in $|\alpha|$ beyond temperatures of 200 K, as observed in our experiments and predicted by theory, can be attributed to the dominance of Ω_p over the saturated Ω_s in the fully paramagnetic (PM) state.

Figure 7.3c illustrates how an external magnetic field B affects α. The application of B along the a direction of CrSBr produces a continuous canting of the spins [11]. Such field-induced spin reorientation initially raises Ω_s, which leads to an increase in $|\alpha|$ (pink shaded areas). When further increasing B, the FM order is established and Ω_s is minimized, reducing $|\alpha|$ again [36, 38]. In addition, the transition from AFM to FM order enables interlayer tunneling and thus raises Ω_{layer} (see figure 7.4c). This could explain the higher α in the FM phase compared to the AFM one and has an important consequence: Since both σ and α simultaneously increase with magnetic field, the relative change of the power factor ($\alpha^2\sigma$) between AFM and FM order can reach very high values, up to 600% as observed in our experiment (figure 7.4b).

7.4. CONCLUSIONS

In this work, we investigate the magnetic field and temperature dependent electric and thermoelectric properties of the A-type antiferromagnet CrSBr. We reveal a strong impact of magnetic order on the thermoelectric response of the material, which we attribute to a spin entropy contribution in the total thermopower. In particular, we detect a peak in both the Seebeck coefficient and the power factor around the magnetic transition temperature T_N. These findings present a potential way to overcome the limits of conventional thermoelectric devices, by employing magnetic materials. While devices based on CrSBr show enhanced thermoelectric properties at cryogenic temperatures, future research should investigate 2D magnets with higher transition temperature to enable room temperature operation. Promising materials that deserve attention are the recently investigated 2D compounds $CrTe_2$ and Fe_3GaTe_2 with magnetic ordering temperatures > 300 K [39, 40]. To this end, the use of 2D materials adds further benefits, such as the possibility to tune the transition temperature by varying the flake thickness, composition, electrostatic gating, or by producing heterostructures of different layers, in order to yield optimum performance at room temperature [41–44].

7.5. APPENDIX

7.5.1. DEVICE FABRICATION

The thermopower devices have been fabricated by standard Electron Beam Lithography (EBL) on a Silicon (Si) wafer with a 285 nm top layer of Silicon Oxide (SiO_2). First, the heaters are fabricated by depositing

3 nm of Titanium (Ti) and 27 nm of Palladium (Pd). Afterwards, the sample is covered by 10 nm of Aluminum Oxide (Al_2O_3) via atomic layer deposition, performed in an Oxford Instruments FlexAL system. Then, 3 nm of Ti and 47 nm of Gold (Au) are deposited as top contacts. Crystals of CrSBr were synthesized using a chemical vapor transport method. This synthetic technique involved the transport of material from 950 °C at the source side to 850 °C at the sink side of a slightly off stoichiometric combination of Cr, S, and CrBr3 in an evacuated fused silica ampoule. The detailed synthesis and cleaning procedure can be found elsewhere [45]. CrSBr flakes are mechanically exfoliated using the Scotch tape method [46, 47] and deposited on a PDMS square of approximately 1 mm x 1 mm positioned on a glass slide to facilitate its handling [48, 49], and transferred onto the pre-patterned contacts. Encapsulation with hBN is then performed by means of the dry transfer method using a PDMS-Polypropylene carbonate (PPC) stamp [50, 51]. CrSBr handling is entirely done under inert atmosphere in a N_2 glove box, with <0.5 ppm of O_2 and <0.5 ppm of H_2O content, in order to avoid air degradation and contamination of the sample. More details about the fabrication process can be found in the Supplementary Information in Ref. [1]

7.5.2. THERMOELECTRIC AND ELECTRICAL TRANSPORT MEASUREMENTS

Electrical transport and thermopower measurements were performed in a ^{4}He cryostat using home-built ultra-low noise voltage/current sources and pre-amplifiers. We employed a lock-in double-demodulation technique[25] (see also chapter 4), which allows to decouple the thermocurrent $\tilde{I}_{\text{th}}$ flowing as a response to a thermal bias ΔT from $\tilde{I}_{\text{sd}}$, the response to a voltage bias $\tilde{V}_{\text{sd}}$ [25]. To this end, an AC current $\tilde{I}_{\text{h}}$ = 0.5 mA (power P = 0.12 mW) at frequency ω_1 = 3 Hz is applied to the Pd heater with a Stanford Research SR830 lock-in connected to a current source. Simultaneously, an AC voltage $\tilde{V}_{\text{sd}} = 10$ mV at ω_2 = 13 Hz is applied to the drain contact. The current at the source contact is pre-amplified by a low-noise transimpedance amplifier and demodulated at ω_1 and ω_2 to obtain $\tilde{I}_{\text{th}}$ and $\tilde{I}_{\text{sd}}$, respectively.

7.5.3. CALIBRATION OF ΔT

In order to evaluate the Seebeck coefficient of CrSBr, it is necessary to know the temperature difference ΔT along the flake. Such parameter can be obtained by calibrating the temperature-dependent resistance of the two gold thermometers, defined as R_A and R_B. The setup used to calibrate thermometers A and B is displayed in figure 7.5a and 7.5b respectively. The calibration consists in a resistance measurement with

and without a thermal gradient applied. Such gradient is generated via Joule effect, by feeding the heater on a current I_h. Figures 7.5a-b shows the resistance values R_A and R_B, respectively, in a range between 20 K and 200 K. To perform the resistance measurement, both resistors are biased with a current of 1 μA. Let us consider the formula $R = R_0(1 + TCR(T - T_0))$, where TCR stands for Temperature Coefficient of Resistance. By linearly fitting the two curves, we extract the slopes in figures 7.5a-b, corresponding respectively to the products $TCR_A R_{0_A}$ = 0.045 Ω/K and $TCR_B R_{0_B}$ = 0.290 Ω/K. Figures 7.5c-d report the resistance values on thermometers R_A and R_B, respectively, as a function of the power P produced on the heater. The AC current I_h is swept between 0 and 1.5 mA. The measurement is performed at a constant temperature of 30 K. Resistance values are then converted in temperature jumps δT induced by the thermal gradient on the two thermometers A and B, equal to 1.4 K and 0.1 K at 30 K. By subtracting the two temperature-dependent δT, we obtain the temperature difference ΔT at the extremes of the device at a given temperature. For the used power value of 0.12 mW we extract a ΔT of 1.3 ± 0.1 K at 30 K. By following this procedure, we are able to extract the values of ΔT for the temperatures in range between 20 and 220 K, thereforetaking into account the temperature-dependent variation of ΔT.

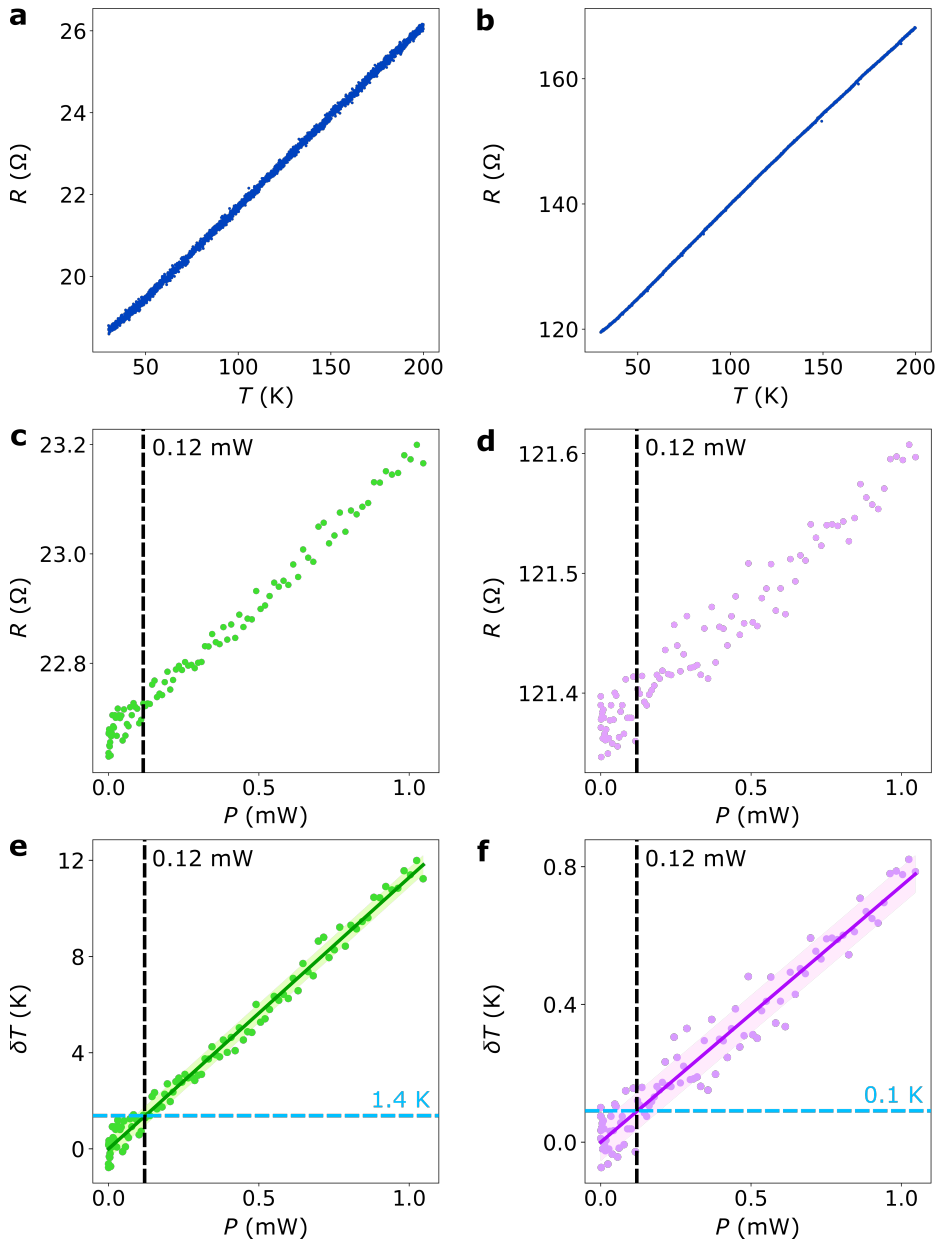

Figure 7.5: Calibration of the thermometers. a,b. Resistance of gold thermometers A (a) and B (b) vs T. c,d. Resistance of gold thermometers A (c) and B (d) vs power applied to the heater P. e,f. Extracted temperature jump δT on thermometers A (e) and B (f) vs P. The black dashed line indicates the power value used in the experiments described in the main text (0.12 mW), while the cyan dashed line indicates the corresponding temperature jump for the two thermometers (1.4 and 0.1 respectively).

REFERENCES

[1] A. Canetta, S. Volosheniuk, S. Satheesh, J. P. Alvarinhas Batista, A. Castellano, R. Conte, D. G. Chica, K. Watanabe, T. Taniguchi, X. Roy, H. S. J. van der Zant, M. Burghard, M. J. Verstraete, and P. Gehring. “Impact of Spin-Entropy on the Thermoelectric Properties of a 2D Magnet”. *Nano Letters* 24.22 (2024), pp. 6513–6520.

[2] P. Sun, K. R. Kumar, M. Lyu, Z. Wang, J. Xiang, and W. Zhang. “Generic Seebeck effect from spin entropy”. *The Innovation* 2.2 (2021), p. 100101.

[3] K. Behnia. “1Basic Concepts”. *Fundamentals of Thermoelectricity*. Oxford University Press, Jan. 2015. isbn: 9780199697663.

[4] Y. Apertet, H. Ouerdane, C. Goupil, and P. Lecoeur. “A note on the electrochemical nature of the thermoelectric power”. *The European Physical Journal Plus* 131.4 (Apr. 2016).

[5] J. Cai and G. D. Mahan. “Effective Seebeck coefficient for semiconductors”. *Phys. Rev. B* 74 (7 Aug. 2006), p. 075201.

[6] P. M. Chaikin and G. Beni. “Thermopower in the correlated hopping regime”. *Phys. Rev. B* 13 (2 Jan. 1976), pp. 647–651.

[7] M. R. Peterson and B. S. Shastry. “Kelvin formula for thermopower”. *Phys. Rev. B* 82 (19 Nov. 2010), p. 195105.

[8] G. Yang, L. Sang, C. Zhang, N. Ye, A. Hamilton, M. S. Fuhrer, and X. Wang. “The role of spin in thermoelectricity”. *Nature Reviews Physics* 5.8 (Aug. 2023), pp. 466–482.

[9] E. Pyurbeeva, J. A. Mol, and P. Gehring. “Electronic measurements of entropy in meso- and nanoscale systems”. *Chemical Physics Reviews* 3.4 (Dec. 2022), p. 041308.

[10] B. S. Shastry. “Thermopower in Correlated Systems”. *New Materials for Thermoelectric Applications: Theory and Experiment*. Ed. by V. Zlatic and A. Hewson. Dordrecht: Springer Netherlands, 2013, pp. 25–29.

[11] N. Tsujii, A. Nishide, J. Hayakawa, and T. Mori. “Observation of enhanced thermopower due to spin fluctuation in weak itinerant ferromagnet”. *Science Advances* 5.2 (2019), p. 5935.

[12] L. Wang, X. Zhang, and L.-D. Zhao. “Evolving Strategies Toward Seebeck Coefficient Enhancement”. *Accounts of Materials Research* 4.5 (2023), pp. 448–456.

[13] A. Portavoce, E. Assaf, M. Bertoglio, D. Narducci, and S. Bertaina. “Magnetic moment impact on spin-dependent Seebeck coefficient of ferromagnetic thin films”. *Scientific Reports* 13 (Jan. 2023).

[14] Y. Yao, X. Zhan, M. G. Sendeku, P. Yu, F. T. Dajan, C. Zhu, N. Li, J. Wang, F. Wang, Z. Wang, and J. He. “Recent progress on emergent two-dimensional magnets and heterostructures”. *Nanotechnology* 32.47 (Sept. 2021), p. 472001.

[15] X. Jiang, Q. Liu, J. Xing, N. Liu, Y. Guo, Z. Liu, and J. Zhao. “Recent progress on 2D magnets: Fundamental mechanism, structural design and modification”. *Applied Physics Reviews* 8.3 (July 2021), p. 031305.

[16] K. Burch, D. Mandrus, and J.-G. Park. “Magnetism in two-dimensional van der Waals materials”. *Nature* 563 (Oct. 2018).

[17] D. L. Cortie, G. L. Causer, K. C. Rule, H. Fritzsche, W. Kreuzpaintner, and F. Klose. “Two-Dimensional Magnets: Forgotten History and Recent Progress towards Spintronic Applications”. *Advanced Functional Materials* 30.18 (2020), p. 1901414.

[18] E. J. Telford, A. H. Dismukes, K. Lee, M. Cheng, A. Wieteska, A. K. Bartholomew, Y.-S. Chen, X. Xu, A. N. Pasupathy, X. Zhu, C. R. Dean, and X. Roy. “Layered Antiferromagnetism Induces Large Negative Magnetoresistance in the van der Waals Semiconductor CrSBr”. *Advanced Materials* 32.37 (2020), p. 2003240.

[19] E. Telford, A. Dismukes, R. Dudley, R. Wiscons, K. Lee, D. Chica, M. Ziebel, M.-G. Han, J. Yu, S. Shabani, A. Scheie, K. Watanabe, T. Taniguchi, D. Xiao, Y. Zhu, A. Pasupathy, C. Nuckolls, X. Zhu, C. Dean, and X. Roy. “Coupling between magnetic order and charge transport in a two-dimensional magnetic semiconductor”. *Nature Materials* 21 (July 2022), pp. 754–760.

[20] G. E. W. Bauer, E. Saitoh, and B. J. van Wees. “Spin caloritronics”. *Nature Materials* 11.5 (May 2012), pp. 391–399.

[21] K. Lee, A. H. Dismukes, E. J. Telford, R. A. Wiscons, J. Wang, X. Xu, C. Nuckolls, C. R. Dean, X. Roy, and X. Zhu. “Magnetic Order and Symmetry in the 2D Semiconductor CrSBr”. *Nano Letters* 21.8 (2021), pp. 3511–3517.

[22] F. Wu, I. Gutiérrez-Lezama, S. A. López-Paz, M. Gibertini, K. Watanabe, T. Taniguchi, F. O. von Rohr, N. Ubrig, and A. F. Morpurgo. “Quasi-1D Electronic Transport in a 2D Magnetic Semiconductor”. *Advanced Materials* 34.16 (2022), p. 2109759.

[23] S. López Paz, Z. Guguchia, V. Pomjakushin, C. Witteveen, A. Cervellino, H. Luetkens, N. Casati, A. Morpurgo, and F. Rohr. “Dynamic magnetic crossover at the origin of the hidden-order in van der Waals antiferromagnet CrSBr”. *Nature Communications* 13 (Aug. 2022).

[24] P. Gehring, M. van der Star, C. Evangeli, J. J. Le Roy, L. Bogani, O. V. Kolosov, and H. S. J. van der Zant. “Efficient heating of single-molecule junctions for thermoelectric studies at cryogenic temperatures”. *Applied Physics Letters* 115.7 (Aug. 2019), p. 073103.

[25] P. Gehring, J. Sowa, C. Hsu, J. Bruijckere, M. Star, J. Le Roy, L. Bogani, E. Gauger, and H. Zant. “Complete mapping of the thermoelectric properties of a single molecule”. *Nature Nanotechnology* 16 (Apr. 2021), pp. 1–5.

[26] W. Liu, X. Guo, J. Schwartz, H. Xie, N. U. Dhale, S. H. Sung, A. L. N. Kondusamy, X. Wang, H. Zhao, D. Berman, R. Hovden, L. Zhao, and B. Lv. “A Three-Stage Magnetic Phase Transition Revealed in Ultrahigh-Quality van der Waals Bulk Magnet CrSBr”. *ACS Nano* 16.10 (2022), pp. 15917–15926.

[27] C. Boix-Constant, S. Mañas-Valero, A. M. Ruiz, A. Rybakov, K. A. Konieczny, S. Pillet, J. J. Baldoví, and E. Coronado. “Probing the Spin Dimensionality in Single-Layer CrSBr Van Der Waals Heterostructures by Magneto-Transport Measurements”. *Advanced Materials* 34.41 (2022), p. 2204940.

[28] C. Ye, C. Wang, Q. Wu, S. Liu, J. Zhou, G. Wang, A. Söll, Z. Sofer, M. Yue, X. Liu, M. Tian, Q. Xiong, W. Ji, and X. Renshaw Wang. “Layer-Dependent Interlayer Antiferromagnetic Spin Reorientation in Air-Stable Semiconductor CrSBr”. *ACS Nano* 16.8 (2022), pp. 11876–11883.

[29] J. Klein, B. Pingault, M. Florian, M.-C. Heißenbüttel, A. Steinhoff, Z. Song, K. Torres, F. Dirnberger, J. B. Curtis, M. Weile, A. Penn, T. Deilmann, R. Dana, R. Bushati, J. Quan, J. Luxa, Z. Sofer, A. Alù, V. M. Menon, U. Wurstbauer, M. Rohlfing, P. Narang, M. Lončar, and F. M. Ross. “The Bulk van der Waals Layered Magnet CrSBr is a Quasi-1D Material”. *ACS Nano* 17.6 (2023), pp. 5316–5328.

[30] G. K. Madsen, J. Carrete, and M. Verstraete. “BoltzTraP2, a program for interpolating band structures and calculating semi-classical transport coefficients”. *Computer Physics Communications* 231 (2018), pp. 140–145.

[31] A. Zunger, S.-H. Wei, L. G. Ferreira, and J. E. Bernard. “Special quasirandom structures”. *Physical Review Letters* 65.3 (July 1990), pp. 353–356.

[32] F. Körmann, B. Grabowski, B. Dutta, T. Hickel, L. Mauger, B. Fultz, and J. Neugebauer. “Temperature Dependent Magnon-Phonon Coupling in bcc Fe from Theory and Experiment”. *Physical Review Letters* 113.16 (Oct. 2014).

[33] Z. Sun, H. Wang, A. Wang, B. Lei, W. Zhuo, F. Yu, X. Zhou, J. Ying, Z. Xiang, T. Wu, and X. Chen. “Large Thermopower Enhanced by Spin Entropy in Antiferromagnet EuMnSb2”. *Advanced Functional Materials* 32.33 (2022), p. 2202188.

[34] Y. Demirel and V. Gerbaud. “Chapter 13 - Organized Structures”. *Nonequilibrium Thermodynamics (Fourth Edition)*. Ed. by Y. Demirel and V. Gerbaud. Fourth Edition. Elsevier, 2019, pp. 603–662.

[35] N. Wilson, K. Lee, J. Cenker, K. Xie, A. Dismukes, E. Telford, J. Fonseca, S. Sivakumar, C. Dean, T. Cao, X. Roy, X. Xu, and X. Zhu. “Interlayer electronic coupling on demand in a 2D magnetic semiconductor”. *Nature Materials* 20 (Dec. 2021), pp. 1–6.

[36] Y. Wang, N. S. Rogado, R. J. Cava, and N. P. Ong. “Spin entropy as the likely source of enhanced thermopower in NaxCo2O4”. *Nature* 423.6938 (May 2003), pp. 425–428.

[37] T. Okabe. “Spin-fluctuation drag thermopower of nearly ferromagnetic metals”. *Journal of Physics: Condensed Matter* 22.11 (Mar. 2010), p. 115604.

[38] J. C. Bonner and M. E. Fisher. “The Entropy of an Antiferromagnet in a Magnetic Field”. *Proceedings of the Physical Society* 80.2 (Aug. 1962), p. 508.

[39] H. Wu, W. Zhang, L. Yang, J. Wang, J. Li, L. Li, Y. Gao, L. Zhang, J. Du, H. Shu, and H. Chang. “Strong intrinsic room-temperature ferromagnetism in freestanding non-van der Waals ultrathin 2D crystals”. *Nature Communications* 12 (Sept. 2021).

[40] X. Zhang, Q. Lu, W. Liu, W. Niu, J. Sun, J. Cook, M. Vaninger, P. Miceli, D. Singh, S.-W. Lian, T.-R. Chang, X. He, J. Du, L. He, G. Bian, and Y. Xu. “Room-temperature intrinsic ferromagnetism in epitaxial CrTe2 ultrathin films”. *Nature Communications* 12 (May 2021), p. 2492.

[41] D. Li, Y. Gong, Y.-X. Chen, J. Lin, Q. Khan, Y. Zhang, Y. Li, and H. Xie. “Recent Progress of Two-Dimensional Thermoelectric Materials”. *Nano-Micro Letters* 12 (Dec. 2020), p. 36.

[42] M. Razeghi, J. Spiece, O. Oğuz, D. Pehlivanoğlu, Y. Huang, A. Sheraz, U. Başçı, P. Dobson, J. Weaver, P. Gehring, and S. Kasirga. “Single-material MoS2 thermoelectric junction enabled by substrate engineering”. *npj 2D Materials and Applications* 7 (May 2023).

[43] S. Tu, T. Ziman, G. Yu, C. Wan, J. Hu, H. Wu, H. Wang, M. Liu, C. Liu, C. Guo, J. Zhang, M. Cabero, Y. Zhang, P. Gao, S. Liu, D. Yu, X. Han, I. Hallsteinsen, D. Gilbert, and H. Yu. “Record thermopower found in an IrMn-based spintronic stack”. *Nature Communications* 11 (Apr. 2020).

[44] J. Oh, Y. Kim, S. Chung, H. Kim, and J. G. Son. “Fabrication of a MoS2/Graphene Nanoribbon Heterojunction Network for Improved Thermoelectric Properties”. *Advanced Materials Interfaces* 6.23 (2019), p. 1901333.

[45] A. Scheie, M. Ziebel, D. G. Chica, Y. J. Bae, X. Wang, A. I. Kolesnikov, X. Zhu, and X. Roy. “Spin Waves and Magnetic Exchange Hamiltonian in CrSBr”. *Advanced Science* 9.25 (2022), p. 2202467.

[46] K. S. Novoselov, A. K. Geim, S. V. Morozov, D. Jiang, Y. Zhang, S. V. Dubonos, I. V. Grigorieva, and A. A. Firsov. “Electric Field Effect in Atomically Thin Carbon Films”. *Science* 306.5696 (2004), pp. 666–669.

[47] K. S. Novoselov, D. Jiang, F. Schedin, T. J. Booth, V. V. Khotkevich, S. V. Morozov, and A. K. Geim. “Two-dimensional atomic crystals”. *Proceedings of the National Academy of Sciences* 102.30 (2005), pp. 10451–10453.

[48] A. Castellanos-Gomez, M. Buscema, H. Zant, and G. Steele. “Deterministic transfer of two-dimensional materials by all-dry viscoelastic stamping”. *2D Materials* 1 (Nov. 2013).

[49] R. Frisenda, E. Navarro-Moratalla, P. Gant, D. Perez de Lara, P. Jarillo-Herrero, R. Gorbachev, and A. Castellanos-Gomez. “Recent progress in the assembly of nanodevices and van der Waals heterostructures by deterministic placement of 2D materials”. *Chemical Society Reviews* 47 (Nov. 2017).

[50] K. Kinoshita, R. Moriya, M. Onodera, Y. Wakafuji, S. Masubuchi, K. Watanabe, T. Taniguchi, and T. Machida. “Dry release transfer of graphene and few-layer h-BN by utilizing thermoplasticity of polypropylene carbonate”. *npj 2D Materials and Applications* 3.1 (May 2019).

[51] L. Wang, I. Meric, P. Y. Huang, Q. Gao, Y. Gao, H. Tran, T. Taniguchi, K. Watanabe, L. M. Campos, D. A. Muller, J. Guo, P. Kim, J. Hone, K. L. Shepard, and C. R. Dean. “One-Dimensional Electrical Contact to a Two-Dimensional Material”. *Science* 342.6158 (2013), pp. 614–617.

8

CONCLUDING REMARKS

"*The time will come when diligent research over long periods will bring to light things which now lie hidden. A single lifetime, even though entirely devoted to the sky, would not be enough for the investigation of so vast a subject... And so this knowledge will be unfolded only through long successive ages. There will come a time when our descendants will be amazed that we did not know things that are so plain to them... Many discoveries are reserved for ages still to come, when memory of us will have been effaced.*"

"Natural Questions, Book VII", Seneca

Every journey eventually comes to an end, marked by lessons learned, work accomplished, and opportunities left behind. Not an exception is this path of "Thermoelectric effects in quantum systems". Under "quantum systems", different molecular devices are considered in this work, except in the last chapter where we discuss the thermoelectric response of a two-dimensional magnet. As a last step, I would like to go through the main conclusions, pinpoint their relevance and remark on the missed opportunities. As such, I would identify some questions/problems that naturally occurred along the way but were not fully addressed or explored and could serve as a basis for the future studies. Then, I finish with an outlook which goes beyond thermoelectricity and questions the role of single molecules in future electronics.

8.1. CONCLUSION

This dissertation started by developing thermometry for three-terminal molecular devices [1] with the local heaters. Among many different approaches (see [2] and references therein) and inspired by [3], we decided to proceed with SNS-thermometry. This allowed us to keep the same number of lithographic steps and did not over-complicate the fabrication process. Instead of golden contacts, we used MoRe superconductors that form Josephson junctions with the golden bridge and provide information about the electronic temperature in the close vicinity of the molecule. This facilitated the experimental extraction of the temperature gradient across the junction, previously unattainable for molecular EMBJ devices in the low-T (< 10 K) range. It paved the way to accurately determine the Seebeck coefficient. It also made the future heat flow-related experiments possible (for example, investigation on gate control of heat flow, similar to [3], can be done in molecular devices). Optimal selection of parameters provided a sensitive thermometer in the range from 100 mK and up to 5 K. However, there were some limitations. First of all, for low temperatures, MoRe completely proximitizes a part of the gold bridge. It means that we effectively probe the molecule via a metal with a gap in its density of states spectrum. Interesting physical phenomena can originate from this, e.g. formation of in-gap bound states, but on the other hand, for certain measurements this effect could be undesired. There are two ways to avoid the presence of subgap states: either apply a small magnetic field (greater than 100 mT) to mitigate the proximity effect or extend the golden bridge length and position the superconducting contacts further from the molecule. The latter approach could impact the accuracy of the measured temperature gradient compared to the actual gradient, as the thermometer would be far away from the molecule.

Another problem is that the resistivity of MoRe is higher than that of Au and the contact resistance in our design is around 1 MΩ which is not desirable for electromigration. We are avoiding this problem by connecting all four contacts on each side of the golden bridge in parallel, but then the device cannot be used if one of the contacts do not work. Also, each thermometer requires four contacts for the thermometry measurements which reduces the amount of different devices that could be bonded on one chip carrier (two instead of six). We found a solution to this by adapting the design in such a way that there is a possibility of having more devices connected to the chip, but this new generation of samples never reached the dilution refrigerator and were not tested in real measurements.

In the next chapter, we discussed the measurement technique. The double lock-in technique was employed and many important physical discoveries were obtained with it [4–6]. It allows to measure the thermocurrent and differential conductance simultaneously, which is of crucial importance for 'jumpy' molecular devices. However, in previous studies, there were issues with the post-processing of raw data, and the method itself was poorly documented. Although using raw readings from the lock-in did not affect the conclusions in these experiments, accurate analysis is important to extract the right thermovoltage values, essential for precise estimation of power factors and ZT figures of merit. In this chapter, we found that a prefactor of $-2\sqrt{2}$ should be applied to match the thermocurrent signal measured with DC and AC double lock-in technique. Both the sign and the coefficient matter: the '-' sign contains information about the carriers, while the coefficient influences the absolute value of the real thermovoltage in the device. We organized the chapter in a way that it serves both as a manual for the thermoelectric measurement setup and as a guide on physical information that could be extracted from the data in different temperature and bias-voltage regimes. We discuss the necessity to check the origin of the signal to avoid misinterpretation of thermocurrent in case of a temperature difference much larger than the base temperature or in the situation where the conductance is highly dependent on the temperature and mixes up with the measured signal. We hope that the gathered information will be sufficient for the reader to perform measurements and fully leverage the potential of the described technique.

The double lock-in method has a great promise to become the standard approach for molecular investigation. It gives all the information that conventional transport measurement can give and contains invaluable information that thermocurrent can reveal. However, it also has limitations. For example, one of the primary issues, unfortunately not addressed in this thesis, is the slow rate of data accumulation. With the current frequencies, it takes 3-5 seconds to acquire a single data point.

It is important to consider higher frequencies for future measurements.

The culmination experiment of this dissertation is described in chapter 5. Using the double lock-in technique, we investigated the thermoelectric response of a stable all-organic diradical nitronyl nitroxide compound molecule inside an EMBJ device. The presence of superconductors used for thermometry fully proximitized the gold bridge. As a result, the molecule was effectively coupled to superconducting electrodes. The interaction between quasiparticles on the bridge and spin on the molecule gave rise to so-called Yu-Shiba-Rusinov in-gap bound states [7–9]. We investigated their thermoresponse once the system experienced a temperature gradient.

The data revealed that the thermoelectric efficiency of a nanoscale device, consisting of a single molecule only, can be drastically increased by YSR. We demonstrated this by performing thermocurrent experiments at mK temperatures and at different external magnetic fields. By driving the system through a quantum phase transition from the Kondo into the Yu-Shiba-Rusinov regime by changing the magnetic field, i.e., by controlling the proximity effect, we showed that the superconducting bound states act as ultra sharp energy filters, boosting the thermoelectric response. These findings are relevant for heat energy harvesting applications, i.e, for the implementation of a molecular heat engine design by engineering spin-full single molecules and coupling them to superconducting leads that could reach the thermodynamic conversion limit.

The presented data still lacks theoretical support, and further experimental/theoretical work is needed. It would be interesting to explain the data in greater detail and see how the experimental results depend on the temperature, on the coupling to the leads, and on the amplitude of Kondo correlations, to find an optimal point for the maximum output of the system. Besides, inspired by [10] it would be interesting to investigate whether thermocurrent provides information on the spin of the impurity and number of Kondo channels. We believe that addressing these questions within both the STM and EMBJ techniques is essential for gaining a comprehensive understanding.

In chapter 6, we continued with the fundamental study of a nanoscale heat-energy harvester based on a single molecule. This time, we investigated the thermoelectric properties of an all-organic, diradical molecule in an EMBJ device without SNS thermometers. By applying a gate voltage, we controlled the molecule's charge state, leading to a Kondo resonance in one charge state and inelastic cotunneling excitations in the other. Data is consistent with previous STM [11] and MCBJ [12] results on the same molecule. We also determined that for the investigated configurations, antiferromagnetic coupling between the spins on the radical parts of the molecule was present. By applying a temperature gradient over the junction and connecting a load resistor,

we utilized the molecule as a quantum heat engine and measured the dependence of the maximum power output as a function of active load. This represents the first realization of a molecular particle exchange heat engine. Our findings suggest that molecular devices offer a compelling alternative to conventional cyclic heat engines, as they operate without moving components, exchanging particles between two heat reservoirs through a narrow molecular energy band. We also observed that the engineering efficiency of the device was very sensitive to the configuration of the molecule inside the junctions. Two distinct stable configurations of the molecule yielded power outputs that differed by two orders of magnitude under the same load conditions. This finding underscores the critical importance of precise molecular control within the junction for optimizing performance in practical applications.

Despite these insights, several key aspects of this work remain unexplored and need to be investigated further. First, it is essential to calculate the exact heat flow in the system to see how close to the Carnot limit the molecular engine operates. Second, the thermotransport response of the molecule displayed a blockade region in conductance, while at the same time, it did not show it in thermocurrent. Also, the thermocurrent did not change sign on the edges of the Coulomb diamonds and stayed positive at the positive side and negative at the negative bias voltage. We do not have an explanation for these observations and follow-up theoretical work would be helpful.

Finally, we finished this dissertation with an investigation of the thermopower response of a 2D magnet. Here, we implemented the double lock-in technique to study an A-type ferromagnet CrSBr flake. We recorded the change of conductance and thermocurrent as a function of temperature and applied magnetic field (field oriented in parallel to the medium a-axis). Both of these parameters changed the magnetic order of the material and led to changes in the Seebeck coefficient and power factor coefficient. At low temperatures, below 50 K, we observed hidden magnetic order characterized by a rapid decrease of the Seebeck coefficient, similarly to prior studies [13, 14]. With increasing temperature, we detected an enhancement of the power factor and S coefficient, with an amplitude maximum around Néel temperature. Our data also indicated that for temperatures where CrSBr is in the antiferromagnetic phase, we could boost the power factor by changing the system to a ferromagnetic phase with the means of an external magnetic field. For the lowest temperatures, we observed around a 600% increase of the PF at the AFM-FM phase transition point with respect to the PF at 0 magnetic field. We showed that we can explain all these findings by taking into account variations in the entropy linked to the magnetic order. Particularly, we demonstrated that spin-entropy plays a significant role in the thermopower response.

Our observations paved the way to use 2D magnets as energy

harvesting devices with controlled efficiency. Further studies are needed to investigate these effects in 2D magnets with T_N close to room temperature and to collect results in ambient conditions. For example, $CrTe_2$ and Fe_3GaTe_2 deserve extra attention. Also, the thermoresponse exploration of CrSBr is not complete. In follow-up studies, it would be interesting to check for the Nerst effect [15] and compare the thermocurrent of the system along a and b axes for different number of layers. We already know that there is a high anisotropy in conductance along different directions [16], and it would be interesting to see what the difference is in I_{th}, and whether we can conclude anything about the transport mechanism along the b-axis.

8.2. OUTLOOK

In the previous section, we already highlighted a few follow-up projects that could be carried out in future experiments. Here, we expand on that by offering a broader perspective on potential areas of molecular research beyond thermoelectricity. During this PhD journey, the author was oscillating between two states: "molecules are good candidates for future electronics ", and "molecules are only useful for fundamental studies, not practical applications". The true answer can be revealed only during the measurement, so we would keep it open and concentrate on possibilities for future experiments.

Recent realization of microelectromechanical systems (MEMs) architecture for molecular devices [17] opens a new space for further research. The next goal would be to implement a local gate, heaters and thermometry in the same device and then one would have every tool to fully characterize the molecule. This method would combine benefits from EMBJ and MCBJ, and it would be possible to use only one device in order to catch the molecule and have access to the different coupling regimes. We believe that once developed, this platform would be standard for molecular studies. Among different molecules and questions that could be probed by this technique magnetic molecules are of special interest. Recent studies [18–22] already demonstrated interesting physical phenomena such as negative differential conductance [18] (NDC), cotunneling-assisted single-electron tunneling [20] (COSET), spin blockade [21], etc. It would be interesting to investigate the spin properties and understand the exact spin-relaxation mechanisms presented in the system. By harvesting the correct molecule, it would be possible to probe the interaction of the spins inside the molecule (like investigating RKKY interactions [23]) and tackle fundamental questions related to Kondo physics. We would like to highlight here that the same physics can be measured in quantum dots but molecular devices offer the accessibility to higher T_K than their GaAs QD counterparts (for example, for C_{60} molecule [24] T_K exceeded 50 K). Another big area

of research with these molecules could be related to thermoelectric measurements on them. Their magnetic properties can boost their ZT value and make them good candidates for heat-to-energy harvesting. Besides that thermocurrent itself could be a tool that provides more light on understanding of COSET, NDC, etc.

REFERENCES

[1] P. Gehring, J. K. Sowa, C. Hsu, J. de Bruijckere, M. van der Star, J. J. Le Roy, L. Bogani, E. M. Gauger, and H. S. J. van der Zant. “Complete mapping of the thermoelectric properties of a single molecule”. *Nature Nanotechnology* 16.4 (Apr. 2021), pp. 426–430.

[2] J. Pekola. “Trends in Thermometry”. *Journal of Low Temperature Physics* 135.5 (June 2004), pp. 723–744.

[3] B. Dutta, D. Majidi, N. W. Talarico, N. Lo Gullo, H. Courtois, and C. B. Winkelmann. “Single-Quantum-Dot Heat Valve”. *Phys. Rev. Lett.* 125 (23 Dec. 2020), p. 237701.

[4] C. Hsu, T. A. Costi, D. Vogel, C. Wegeberg, M. Mayor, H. S. J. van der Zant, and P. Gehring. “Magnetic-Field Universality of the Kondo Effect Revealed by Thermocurrent Spectroscopy”. *Phys. Rev. Lett.* 128 (14 Apr. 2022), p. 147701.

[5] E. Pyurbeeva, C. Hsu, D. Vogel, C. Wegeberg, M. Mayor, H. van der Zant, J. A. Mol, and P. Gehring. “Controlling the Entropy of a Single-Molecule Junction”. *Nano Letters* 21.22 (Nov. 2021), pp. 9715–9719.

[6] A. Canetta, S. Volosheniuk, S. Satheesh, J. P. Alvarinhas Batista, A. Castellano, R. Conte, D. G. Chica, K. Watanabe, T. Taniguchi, X. Roy, H. S. J. van der Zant, M. Burghard, M. J. Verstraete, and P. Gehring. “Impact of Spin-Entropy on the Thermoelectric Properties of a 2D Magnet”. *Nano Letters* 24.22 (June 2024), pp. 6513–6520.

[7] L. Yu. “BOUND STATE IN SUPERCONDUCTORS WITH PARAMAGNETIC IMPURITIES”. *Wu Li Hsueh Pao (China) Supersedes Chung-Kuo Wu Li Hsueh For English translation see Chin. J. Phys. (Peking) (Engl. Transl.)* 21 (Jan. 1965).

[8] H. Shiba. “Classical Spins in Superconductors”. *Progress of Theoretical Physics* 40.3 (Sept. 1968), pp. 435–451.

[9] A. I. Rusinov. “Superconductivity near a paramagnetic impurity”. *Soviet Journal of Experimental and Theretical Physics letters* 9 (1969), pp. 85–87.

[10] F. von Oppen and K. J. Franke. “Yu-Shiba-Rusinov states in real metals”. *Phys. Rev. B* 103 (20 May 2021), p. 205424.

[11] A. Vegliante, S. Fernandez, R. Ortiz, M. Vilas-Varela, T. Baum, N. Friedrich, F. Romero-Lara, A. Aguirre, K. Vaxevani, D. Wang, C. Garcia, H. S. J. van der Zant, T. Frederiksen, D. Peña, and J. I. Pascual. “Tuning the Spin Interaction in Non-planar Organic Diradicals Through Mechanical Manipulation”. *arXiv* (2024). arXiv: 2402.08641.

[12] T. Baum. “Electronic transport signatures of two-electron interactions in all-organic single-molecule junctions”. PhD. thesis. Delft, The Netherlands: TU Delft, 2024.

[13] S. A. López-Paz, Z. Guguchia, V. Y. Pomjakushin, C. Witteveen, A. Cervellino, H. Luetkens, N. Casati, A. F. Morpurgo, and F. O. von Rohr. “Dynamic magnetic crossover at the origin of the hidden-order in van der Waals antiferromagnet CrSBr”. *Nat Commun* 13.1 (Aug. 2022), p. 4745.

[14] C. Boix-Constant, S. Mañas-Valero, A. M. Ruiz, A. Rybakov, K. A. Konieczny, S. Pillet, J. J. Baldoví, and E. Coronado. “Probing the Spin Dimensionality in Single-Layer CrSBr Van Der Waals Heterostructures by Magneto-Transport Measurements”. *Advanced Materials* 34.41 (2022), p. 2204940.

[15] J. Xu, W. A. Phelan, and C.-L. Chien. “Large Anomalous Nernst Effect in a van der Waals Ferromagnet Fe3GeTe2”. *Nano Letters* 19.11 (Nov. 2019), pp. 8250–8254.

[16] F. Wu, I. Gutiérrez-Lezama, S. A. López-Paz, M. Gibertini, K. Watanabe, T. Taniguchi, F. O. von Rohr, N. Ubrig, and A. F. Morpurgo. “Quasi-1D Electronic Transport in a 2D Magnetic Semiconductor”. *Advanced Materials* 34.16 (2022), p. 2109759.

[17] H. Jeong, H. B. Li, L. Domulevicz, and J. Hihath. “An On-Chip Break Junction System for Combined Single-Molecule Conductance and Raman Spectroscopies”. *Advanced Functional Materials* 30.28 (2020), p. 2000615.

[18] H. B. Heersche, Z. de Groot, J. A. Folk, H. S. J. van der Zant, C. Romeike, M. R. Wegewijs, L. Zobbi, D. Barreca, E. Tondello, and A. Cornia. “Electron Transport through Single Mn_{12} Molecular Magnets”. *Phys. Rev. Lett.* 96 (20 May 2006), p. 206801.

[19] A. Cornia, A. C. Fabretti, M. Pacchioni, L. Zobbi, D. Bonacchi, A. Caneschi, D. Gatteschi, R. Biagi, U. Del Pennino, V. De Renzi, L. Gurevich, and H. S. J. Van der Zant. “Direct Observation of Single-Molecule Magnets Organized on Gold Surfaces”. *Angewandte Chemie International Edition* 42.14 (2003), pp. 1645–1648.

[20] R. Gaudenzi, M. Misiorny, E. Burzurí, M. R. Wegewijs, and H. S. J. van der Zant. “Transport mirages in single-molecule devices”. *The Journal of Chemical Physics* 146.9 (Feb. 2017), p. 092330.

8

[21] M. Misiorny, I. Weymann, and J. Barnaś. “Spin diode behavior in transport through single-molecule magnets”. *Europhysics Letters* 89.1 (Jan. 2010), p. 18003.

[22] A. S. Zyazin, J. W. G. van den Berg, E. A. Osorio, H. S. J. van der Zant, N. P. Konstantinidis, M. Leijnse, M. R. Wegewijs, F. May, W. Hofstetter, C. Danieli, and A. Cornia. “Electric Field Controlled Magnetic Anisotropy in a Single Molecule”. *Nano Letters* 10.9 (Sept. 2010), pp. 3307–3311.

[23] N. Nan, W. Li, P.-C. Wang, Y.-J. Hu, G.-L. Tan, and Y.-C. Xiong. “Kondo effect and RKKY interaction assisted by magnetic anisotropy in a frustrated magnetic molecular device at zero and finite temperature”. *Phys. Chem. Chem. Phys.* 23" (10 2021), pp. 5878–5887.

[24] L. H. Yu and D. Natelson. “The Kondo Effect in C60 Single-Molecule Transistors”. *Nano Letters* 4.1 (Jan. 2004), pp. 79–83.

ACKNOWLEDGEMENTS

To begin with, I would like to thank my committee members for dedicating time to reading my thesis. It is a privilege to defend the thesis in the presence of **Prof. Dr. Ir. H.S.J. van der Zant, Prof. Dr. P. Gehring, Dr. M. Blaauboer, Prof. Dr. Y.M. Blanter, Dr. B. Gotsmann, Dr. E. Greplova, Dr. C.B. Winkelmann, and Prof. Dr. Y.V. Nazarov**. Thanks to **Prof. Dr. C. R. Kleijn** for chairing the PhD defense. I am looking forward to interesting opposition and will be glad to defend the work accomplished during these four nice years in Delft.

First of all, I would like to thank **Herre** for allowing me to become a part of the great van der Zant team! It was a fantastic journey through which we accomplished several important milestones. I hope that we pushed the science forward, even if it is a small ϵ_0. You made it possible for me to touch the beauty of the quantum word and to make it my daily work. From the moment I came across your profile, I wanted to be in this group. I was amazed by the way you think and express your thoughts. Further on, during the PhD, I always had the impression that you read all the articles on molecular electronics, and I still do not understand how it is possible. However, the greatest thing that I admire in you is not intelligence or knowledge but your kindness; the first two things can be mastered and are commonly seen among top scientists, but the last one is a scarce and, in my opinion, distinguishes a scientist from The Scientist. And you are the latter!

I like the way you manage the team. You always give great freedom on the topics and the experiments one could perform, and sharpen raw ideas to entertaining stories that the scientific community would enjoy. Scientists working for you are captains of our ships, and van der Zant lab is an excellent fleet where you determine the course and help with the navigation. During my PhD, there always was a feeling of a massive space to maneuver, with a 100% certainty that in case of a storm, Herre will be there and one will be saved from sinking and helped to move on. I am grateful for your understanding and support during the first days of the war; this situation knocked me out for quite a long time. During my first few years in a group that was a constant green light on the experimental road with many results and ambitions. Then the war happened... A year of unproductiveness, doubts, and anxiety. You always could find the right words, closed eyes on my constant redefining of the deadlines, and pushed me when it was necessary to make a step forward. Thank you for that! Because of you, I have a clear plan on what should

be done/written/measured in the nearest time and an understanding of a strong desire to stay in the race. It always matters how the race will finish, but it is more important to enjoy it along the way, and you are an example of how it should be done. Thank you, Herre!

Pascal, ... sorry, Prof. Dr. Pascal Gehring! It was an honor to be your first unofficial PhD student; it was an honor to have all these conversations, "thermoelectric" meetings and chats. You are a maestro of thermopower, and your papers served me as a manual to dive into the topic. You were always there to help with advice or a hint on what to measure or how to solve some measurement-related problem. At any moment when I was going to dive into a new system for exploration, you were the person to ask what gas mixture to use to avoid nitrogen narcosis or oxygen toxicity. It was a pleasure to watch how quickly Gehring's lab grew from one person to many PhDs and postdocs; it was a pleasure to note all the details of the process and observe the growth. Life is an interesting thing; who knows, maybe one day exactly these things will be very relevant and essential to me. I am sure we would interact a lot after the defense!

I can not imagine this thesis without the enormous hard work of the people inside the Quantum Nanoscience department, the Kavli clean room, and the DEMO. You are the inertial forces that keep the system moving in the correct direction. Thank you. The spotlight often hides your work, but the users always know that the calibration of the measurement module is accurate, and EBPG beams are readjusted so we can "plug and play". Many thanks to **Tino** for fixing the pumps and helping to keep the equipment in good order. I think I know so much about the pumps now :). Much appreciation to people who run the machines in the clean room, especially to **Bas, Marinus, Eugene, Lodi, Arnold, Charles, Mark, Anja, Brian, Roald**. Kavli clean room is a Camp Nou, and Delft scientists can do cutting-edge science there. I want to thank **DEMO** for making the best IVVI-rack, which makes the life of an experimentalist easy; it is a piece of art that gives the advantage to Delft research when competing in this Glass Bead Game.

Endless thanks to the people who synthesized and characterized the molecules: **Prof. Marcel Mayor, David Vogel, Christina Wegeberg, Prof. Diego Peña, Manuel Vilas-Varela, Saleta Fernández, Abhisheck Mondal, Sakshi Mehta**. Although the yield of my successful tries was not very high, I had an excellent opportunity to study your creations under low temperatures, sometimes blowing them up with high-temperature gradients or voltages. Also, I would like to specially thank the people who were involved in the CrSBr project. Starting as a person who prepared the prepatterned contacts, I had a great opportunity to measure our best sample in low temperatures. I opened a world of 2D magnets for myself and significantly broadened my sphere of knowledge. I know this project would not be possible without **Sayooj Satheesh,**

José Pedro Alvarinhas Batista, Aloïs Castellano, Daniel G. Chica, Xavier Roy. And, of course, I want to highlight **Alessandra**, who pushed this project to the level of a strong paper. It was nice meeting you, and we had fun in the Netherlands when you came to pick up the samples for your experiments. You are a good scientist. It is very sad that you will leave academia, but at the same time, your art is magnificent, and I believe you will succeed in this field! I am waiting for your new science comic book. Thank you very much for the cover of my thesis. It was precisely the thing I wanted!

The chapters of this thesis would not be complete without the support of my dear friends, who assisted me in conducting measurements or fabricating samples. **Chunwei**, you were my mentor at the beginning of my PhD, and you were the first to show me how to dissolve molecules and to guide me through the first experiments. You are a very kind and thoughtful person. It was a pleasure to have all the conversations with you. I know how difficult and stressful PhD was for you, but, in the end, you published impactful papers and defended your thesis a few months before the end your contract; it is very rare in Delft. I am pleased that you now have a job you love and finally found a balance between work and personal life. Congratulations on your first child! I know how much you wanted to have a bigger family!

Damian, my dear friend Damian, the one who introduced me to the dilution fridge and measurements. You were the person who always doubted everything we measured and was always very pedantic. I miss all of our talks near the blackboard, where we mainly discussed the questions related to superconductivity. It is funny as you were primarily focused on GNRs, and I was on molecules, but all conversations lead to superconductivity. The moment you defended was when I started to use my blackboard less. Science is one of many things you are mastering. It was nice to play board games, cycle, and discuss politics with you. I wish you all the best in your journey. I know you do not want to return to academia, and you believe that most of the academic works are not practically applicable, but the scientific community lost a valuable, reliable unit...

Thomas, a French guy always busy with his molecules, always enthusiastic about his results. I thoroughly enjoyed working with you on measuring the Sme-2Os system. I learned a lot from you. You always knew what to measure, where to dig, and could easily give advice. I loved your optimism; whatever life put on the table, you always had a vision of overcoming obstacles. Enjoy your new career, but do not forget that we still need to write some things up; expect the draft of the heat engine story soon so we can claim the first single molecule engine, a.k.a. a "Moltronic heat engine"! Also, I have many questions on blockchain and crypto, and you are my only friend with a deep understanding of these things. And let’s play football again.

Riccardo and Arnaud, it was a pleasure to mentor both of you during your Master theses; you were definitely in the top of distribution of MSc students in our group, and I was lucky to have you. I learned a lot once I was trying to transfer my knowledge and help you to become independent. The results we measured together will soon be published, and you both know you played an enormous role in these projects. You are both innovative and fast learners; this is what you have in common, and simultaneously, you are so different. I regret that I did not work with both of you at the same time, as we could potentially be the most incredible dream team inside the van der Zant lab. I know Herre's way is to make each researcher independent and self-sufficient, a researcher that can fabricate the samples, perform the experiments, interpret and model the data by themselves, but I think that if we could reverse the time and do it together with the 3 of us, we could solve any problem, including a realization of a new platform for molecular measurements. **Riccardo**, you always wanted to find the root of the problem and asked right, deep questions. At the same time, you are a shiny person with a lot of love for life who can ease any inconvenient situation with a nice joke. Thank you for agreeing to be my paranymph. I am delighted that you have grown to the level where everyone canrely on your measurements without any doubt, and I wish you luck on your PhD trajectory in the van der Zant lab. **Arnaud**, you are a person with tremendous fabrication intuition, who feels the parameters and can give the breath to the most complicated structures with a few magic tricks in the clean room. I appreciated our time together in the lab and at the gym. I promise to return to the gym regularly once I defend my thesis, so we'll chat more. All the best with your new job!

I also want to express my gratitude to people who may not have been directly involved in this thesis but with whom we had a nice time in the lab and who contributed to this work . **Luca**, thank you very much for sharing an office with me and always being ready for an engaging discussion; thank you for checking my figures and giving advice on my code. You were always very kind and knew everything about how different molecular anchoring groups change the physics of the devices. Playing ping-pong after work and consulting on life-related questions was also fun! Our time in the US during the APS meeting was cool; I am very happy that we explored Minneapolis together. I hope you can make it to my defense and we play one more game (spoiler alert: the students damaged the table considerably, so we should look for another place to play). **Jacqueline**, it was a pleasure to work with you; I am very sad that, in the end, we never proved that our measurements were made on ferittin. Sometimes, it is difficult to say whether it is a particle or a golden grain that is being measured. Anyway, interacting with you was always exciting, and I was very happy that you shared the most important moment with me and witnessed my wedding. When I think of you,

I always see your smile. You were always someone who could almost immediately change your serious expression to a calming smile. I hope you are happy with your new job and enjoy life and its miracles.

Tristan, we started almost at the same time and somehow never interacted much in the beginning, but started chatting closer to the end of the PhD track. I found you to be a very reliable person with a kind heart who is always ready to help. I look forward to reading your thesis to learn something new about nanoparticles and to attend your defense. All the best! **Sebastiaan**, somehow, our situation was similar; I do not know why we interacted so little initially. But I am happy we chatted a lot last year about lab, life, etc. I am very happy that you want to stay in academia, and I wish you all the best in picking up the next place where you will continue to use your potential to the fullest. I want to add one thing that I always admired about you. You were always focused on what you wanted to achieve and moved without any chaotic scattering. I wish you the further ballistic way to however you would define success for yourself.

I also want to thank my friend **Josep**. Working and interacting with you during my PhD was great. I learned a lot from you: measurement tricks, a lot about spintronics and 2D materials in general. Because of you, I know the best recipe for BLG samples and have experience measuring QPCs. But what is more important is that even though we do not chat often, I always know that somewhere at MIT, I have an authentic person whom I can call a friend, with whom I can chat at any moment and ask for advice. I keep my fingers crossed that you find a good academic position. Because of people like you, the system (aka the scientific community) becomes more valuable and more trustworthy. All the best, Pep! **Talieh**, thank you for the PMMA transfer method; in the end, I have never used it, but I keep this knowledge with me and await the opportunity. You are a smart, ambitious scientist; I am very happy you will start your group in Delft this summer. I wish you all the best and hope our paths will eventually intersect. We did not chat much during your post-dock here, so let's change it! **Jasper**, we fixed Cactus together! Congratulations on your defense, and good luck with your new job! **Maurits**, it was nice to meet you and see how a person who worked in theory before successfully performed outstanding experiments. Good luck in Germany!

Additionally, I want to thank the younger generation of PhD students in our lab, who are bright minds with bright futures. Enjoy the journey! **Yongqing**, I am super happy that I met you. You are a very hardworking, insightful person. It is a pleasure to work on the GNR project together. I hope we will touch on beautiful physics as soon as possible. I am looking forward to cooling down to mK together and giving you the privilege of being responsible for our Leiden beauty that eats around 120 l of liquid Helium per week :) Thank you very much for the chats and nice dinners together. You and your wife are always welcome in our house!

Cosimo, you are a very structured person who likes to keep everything in order. I am thrilled you have nice results with cable bacteria, and I greatly enjoyed the transport model you proposed. That's the magic of physics, where a simple, intuitive framework can explain complicated things. **Alvaro**, always smiling, joking, and simultaneously the one who accomplished the tasks one by one without any hesitation. I wish you luck with the drum business, "drum baby drum" :).

Linde, I often see how you work at night and scan your samples to find the best flakes for a long time. I wish you a successful PhD and interesting experiments ahead. Thank you very much for being a valuable member of the van der Zant team! **Raul**, we have known each other for a very short time, and I was swamped with writing my thesis when you joined the group, but I see how much progress you made during this time. Well done! I wish you all the best and hope we can cook up some nice experiments together one day. I also want to thank all our Master students! **Alessandro, Joerin, Danyil, Dan, Lucas, Sebastian, Benedict, Abel, Davit**, I am sure your life paths will be full of nice moments and joy! Hope to see you around! And of course, **Loïc**, no, man, I will not forget about you. I remember all your crazy ideas, and you kept inventing new and new. That's how things are done! You are a good person, and you are much more special then you think you are. Looking at you, I understand that the enormous force you apply beats not the most convenient boundary conditions. I am sure you can do more; believe and keep going.

I also thank everyone from the QN department with whom I interacted. **Ulderico**, thank you very much for helping me a lot, for killing my paranoid attitude to setups, and for grounding me once it should have been done. It is always a pleasure to discuss Josephson junctions and the reasons behind diode effects in them. You have a correct, healthy attitude to the work, and I wish you a successful defense! **Martin, Makar**, it is so sad we overlapped only for a short period; I am happy you are both staying in academia. **Thierry**, you were a good office mate, and your knowledge always amazed me. I am happy that you are successful in your work. We should watch football one day together, discuss life, and have a pleasant conversation like we used to have three years ago. **Fabian**, it was a pleasure to be in the room with you; you have a nice taste in music. I love the idea of making a PI-like office; maybe we exaggerated it a bit with four screens per person as too many people believe we are security guys now :) All the best with your PhD. **Samuel**, an expert on CrSBr, each time I needed a correct reference and struggled with literature, you were always ready to help with good advice. Thank you very much. It is nice to see someone still in the lab at 10 p.m. I hope your hard work will award you with lovely fruits. **Gesa**, I was lucky to meet you at the Veldhoven conference, and then I figured out you had moved to Delft. It is always lovely to catch up with you and talk about

life. You are a great scientist. I am looking forward to finding out which German university you chose for your PI position. All the best!

I also had the pleasure of meeting some extraordinary compatriots (I hope this is the most correct English word). **Tess**, it was great to meet you at the summer school in Copenhagen; I am very happy we had a lot of conversations, mainly about the quantum world but not limited by it. I am so glad you found a nice postdoc position and are trying to make Qutech great again :) I know how it hurts and how frustrating this world can be, but keep going and do what you are very good at. **Artem**, you are such a kind and nice person; I am happy that Yaroslaw hired you. I know our conversations are mostly about politics, traitors, and war, but I hope once the world becomes a better place, we will have more time to speak about physics. I hope you find the next position to your liking! **Dima**, I have known you for quite a long time; we first met at the olympiads at school. It is so great that our paths crossed again in a completely different country; it is nice that we both do what we like. Thank you for all the help, especially for fighting with my code; I know how exhausting this can be. I wish you good luck, and may all these random walks always lead you to the desired outcomes. Do not forget that the way itself should be joy, especially if you are not living in a 1D world where the movement is complex and, as a rule, collective.

Alina, you are fearless; thank you for doing the things that most of us did not do. Putting on hold your career for the people you love and risking your life to help them is the most honorable thing I have ever seen. **Sergiy**, thanks for cheering-up conversations and all the help you give everyone. **Ivan**, I know that it is not objective reality to put you in this paragraph, but my brain and heart still both do it. I thank you for everything you did for my country. I hope you enjoy your work at ASML, and I look forward to meeting you again. Folks, I know how painful it is; I know what you are all going through and what levels of stress you are all dealing with. The greatest creature in the world, the human body, must not sink in blood, violence, and desire to submit or erase someone. But we live in a different reality, and the world stopped being a stable place. I believe it never was; we closed our eyes and ignored the conflicts in Africa, Syria and elsewhere on the globe. It was the education system that made many enjoy the history of empires and their glory, and, unfortunately, there are a lot of fools who believe that they know who should live and who should be erased. What is worse are the people who keep silent because it is unpleasant to talk about things, and it is easier to ride pink ponies. I do not know how it will end. I do know we all will die in the end :) This is the script, but let’s try to feel a life a little bit, love, catch a few interesting things, explore, push the boundaries of human knowledge, and make the lives of others more enjoyable.

I went far off track in my previous paragraph, so I would like to stabilize the situation. It would be better to anchor my gratitude to the people I

met outside of Delft University, who were especially influential on the way. First of all, I would like to thank my parents. My childhood was happy, without worries, surrounded by love. You always supported me with all the choices that I made in life and never doubted my decisions. **Dad**, thank you very much for all the books that you always gave me as presents; thank you for all the walks in the forests and all our trips. Thank you very much for renovating my whole house. The best thing we did together was playing football in one team for a whole summer. You did great and were much better than all the younger players. I am looking forward to spend more free time with you. You do not have excuses anymore to play beach volleyball together, so let's schedule something for this summer. **Mom**, thank you very much for all your efforts to organize a nice holiday for me; thank you for assistance in drawing classes and for spending so much time with me on learning foreign languages. You were always a person who could help me with a kind word in difficult life situations. You are a role model of a hardworking person who dedicated almost all her young age to her studies. It could be that you were the reason I opened the books, as these objects did not want to leave your hands. I hope you enjoy this thesis; I'll be happy to explain. We should meet more often!

Mira, my lovely little sister. We spent all our childhood together, cycling a lot. You played football with us and scored that final penalty when we played against a different street :) I always could rely on you, and you always were there with good suggestions on what to read, listen or watch. Now you are a pretty, smart, grown woman who has her own way of dealing with things in life and does not need my advice anymore. I wish you luck with your life in Canada, I hope "Arimka" will grow up one day so I can buy some of your stocks, or maybe you'll gift me some? :) I'm super happy that you'll be here during my defense together with your husband **Alex**, who already become a valuable, beloved member of our big family! **Pavlo**, my little brother, I am happy that we live closer now. I hope you will study well and figure out who you want to be once you are older. **Grandpa Boris**, thank you very much for everything you have done for me. I really enjoy our fishing trips and chats near the fire. Once you visit me, I will take care of getting a fishing permit. **Godmother Natalia**, thank you very much for always being there for me, for suggesting the best books and for all the warmth and care.

Grandpa Dmytro, I do not remember you very well, but I know you spent a lot of time with me when I was a child. Thank you for everything. I am also very lucky to have had wonderful **grandmothers Valentina and Marusia**. It is so sad we will never celebrate this thesis together. You were great, caring people. Thank you for your love and time during my childhood. And many thanks for my **greatgrandgranny Galyna**! You were the whole world to me. All the good I have is because of you. Thank you for your life stories and for all the time and love. You are

always in my heart.

I want to mention all the **teachers at the Sytkivtsi school** who made the classes interesting, challenging, and valuable. They say the level of education in small villages is much worse than in big cities, but this statement is not valid for our school. I thank **Sergij Mukolayovich, Michaylo Borisovych, Natalia Anatoliyivna, Galyna Volodymyrivna** and many others for giving their best to give us the knowledge and to spark curiosity.

One of the best decisions in my life was to enter the **UPML** in Kyiv. It is the best lyceum in Ukraine. There, I understood what I wanted to do in life, and there, for the first time, I had a impression that everything is possible. UPML gave a strong belief that all things can be learned and mastered, and the question is always just about the amount of time invested. I want to give a special thanks to my mathematics teacher, **Inna Yakivna**, informatics teacher **Iryna Viliyivna** and physics teacher **Gerogiy Ivanovich**, as well as our counsellor **Galina Oleksiyivna**. Many thanks to all my classmates **Oleksandr, Volodymyr, Slava, Mykyta, Dima, Ivan, Viktor, Leonid, Oleksiy, Maks, Misha, Sergij, Oleksandr, Liza, Maria, Liliya, Valeria, and Ania** for being there and enjoying that journey together. It is nice to know that you have good friends all around the globe.

In UPML, I met three people who dramatically influenced my life. This thesis is dedicated to one of them who, unfortunately, will never read this acknowledgment. **Oleksandr** was a good friend, always ready to help, calm and peaceful. We spent a lot of evenings together drinking tea, discussing poetry, and doing robotic car competitions. These were conversations full of high hopes for a bright future. I was introduced to the unofficial rules and traditions. It was nice to go to "gitarka" together. I remember that in one of such conversations, I said that I wanted to try to participate in physics olympiads, and Oleksandr was the person who connected me with the right people who later became my best friends. I will always be grateful for that. Oleksandr was also always the first to congratulate me on victories in competitions. Time moved on, we grew up, and our life paths diverged. Later on, the war started, first with the annexation of Crimea and the East. Oleksandr dropped out of the university and joined the army... From that moment, we chatted occasionally; it was not about war but more about love and plans for the future. I often regret that I did not return to Ukraine then; that’s something that I have to live with... Once we touched that topic Oleksandr always cheered me up, but... And then the full-scale war began in 2022... Rest in peace, brother...

I was lucky to meet **Roman** and **Vova**, who first became my mentors in physics and mathematics and then best friends. I am very grateful that you provided me with a clear plan and strategy on what to learn. **Roma**, we walked around UPML each evening and talked about everything. The

same thing as we did at university later on. Thank you for always being there, ready to listen, understand, and give the best advice. You are a kind, great person with an open heart. I am constantly thinking about everything you'll go through now, and I want the war to end so you can think about something more prominent, as before. It is painful to hear that your biggest dream now is to survive. I can not understand it entirely, but I firmly believe no one should go through such hell. All the best, friend. I look forward to our meeting after the war! **Vova**, somehow it happened that it was always about physics, girls, and more physics for us. You were always a close friend, and we went through a lot together. I firmly believe that Google hired a great scientist, so the future of quantum computing is in good hands. I remember our last in-person chat during the APS meeting. You are often correct in your statements, but there were two that I really wish were utterly wrong. First, I believe you are underestimating Europe as a player, and I hope we will soon figure that out. Secondly, I do not think that you have already written your best work; it is still yet to come.

I am also grateful to the good people whore were there during my Bachelor's and Master's studies at MIPT. I thank the Chernogolovka team for being good friends. **Kolya**, I think that dropping out from your PhD in a third year moving to Europe and starting everything from scratch was the difficult but correct decision. I wish you all the best. Thanks for introducing me to nice music and art. **Aleksey**, you were always a good reliable friend. We often talked about some analytical tricks to solve different problems. During our last year of Masters, we frequently drank tea, listened to music, and worked till late at night in the lab. You are intelligent and hardworking, which are great ingredients to success. I wish you luck in your research and very happy that you have a big family now! **Sergey**, congratulations on your thesis, and good luck with your postdoc. It was nice to see you in the US; even though I missed your talk, we had a long chat to discuss your research and life. Stay positive as always, and keep sending pictures from your trips all around Asia. **Evgenij**, thank you for sharing the room in dorm with me and for your constant optimism and love for life. All the best!

In general, my undergraduate life was good, and I met many good people, for which I am very grateful. It was a privilege to have lectures from world-known professors and attend seminars led by young, successful researchers. I am grateful for everything to **Prof. Markeev, Prof. Andreev, Prof. Skvotsov, Prof. Kiselev, Prof. Ryazanov, Prof. Pudalov, Prof. Tsirlina, Prof. Kukushkin** and many others. Thanks to **A.Yu. Kuntsevich** for being my first supervisor and helping me with my first steps in experimental physics. MIPT was considered to be the best place for physicists in post-Soviet Union countries; most likely, that's true. In another reality, it could serve me as a reserve base in a case of life turbulence, but that is not the case for me anymore.

The moment they supported the war was the moment when they were forever destroyed by a rocket in my heart...

After my Master's, I went to Germany and worked in the group of **Prof. Dr. Alexey Ustinov**. I am very grateful for this opportunity and happy that, at a certain point, I was a part of one of the leading quantum computing group in the world. Dr. Ustinov, thank you for the opportunity and advice, especially when discussing future life paths. In the end, your high esteem towards Herre was one of the markers for me to dive into the unknown and enjoy the molecular world under van der Zant's team wings. That year in Karlsruhe was the best of my life so far. The science went very fast, and the ideas on what to do and how to improve the recipes appeared one by one.

Of course, that would not be possible without two great people who are so deep in my heart and whom I own so much, **Alex and Jürgen**. Working and spending free time with you was such a pleasure. The time ran out so fast :(... **Alex**, thank you for being my mentor in the clean room and teaching me all the tricks. You are the best fabrication person I know, I met many great people who can do magic in a CR, but no one was close to being as good as you. I like our Zoom chats and all the discussions on how to fix the setups, arrange some measurements, or conversations on how to find yourself in this world and what "I" really means :) I am happy you are in Google now and have more capabilities for experiments then usual universities do, but I still hope that one day you will go back to academia, to teach a lot of young students like me on how to make the best Transmon qubits. **Jürgen**, my dear Jürgen, the best of the best. Our interaction was a melody; you knew everything about TLS, and I hope if someone would put a full stop to this topic one day, then it would be you! Thank you very much for all our lunches, all the drawings on the blackboard, and cheat notes on measuring qubits. I have kept that book with me, and I hope we can do some experiments together one day. What do you think about molecules for QC? Of course, no GHz anymore, 10s of THz in the best case, but why not? Jurgen, you are a super kind and super shiny person. I love how you deal with pressure; you are a role model of how an honest researcher should behave. Good luck with everything you are doing!

Along the way, I met the most important person in my life – someone with whom I share everything and plan to spend the rest of my days. I love you so much, my lovely wife **Olga**. Thank you very much for everything! You were why I agreed to start searching for a position in the Netherlands. You are incredibly smart, bright, beautiful, magnificent, inspiring, compassionate, talented, and truly one of a kind. I love how you think, speak, express yourself, smile, and fly. I love your explanations of biology, cancer, viruses, and bacteria and your introduction to the history of humankind. I love your care, and time with you is gold. I know we have already been through so much together... losing someone we

loved... holding on through the chaos of war, and the constant feeling of being emigrants. But together we were always able to find the strength to smile even when all we wanted to do was scream... To "hold on when there is nothing in you except the Will which says: ‘Hold on!’". I know that I can always rely on you, I know you will fight for us and I promise to do the same. I really appreciate that you understand that sometimes I need to stay longer in a clean room or near the fridge. Sometimes, once I come back from work when you are already sleeping, I just stay near you to realize how blessed I am. Thank you very much for our trips and for our cycling, and thank you for educating me in art and cinema. Thank you for everything you did for me, my family, and my people. I’m sure the best is still ahead – there should always be a sunrise to look forward to, right?

I also want to thank the small creatures that are occupying all floors of my house, who are constantly chewing something and give a meaning to this life: **Hidde, Agatha, Rosa, Fedya, Tasia, Pet’ka, Alaya, Taras, Gertrusha, and Quentin**.

Finally, and most importantly, I want to express my deepest gratitude to those who put their lives on hold to take on the most difficult and dangerous work. To those who traded offices and warm homes for trenches, where death looms constantly. There is no greater honor than defending the ones you love – fighting for the right to exist; to feel the warmth of the sun; to gaze at the blue sky in freedom; to be able to choose the future and build it on your own.

It is madness that, in the 21st century, there are still those who deny the existence of an entire nation, dehumanize its people, and believe borders can be redrawn by force, disregarding the lives of those who live there. Some say the situation is not black and white, but they are wrong! This is a clear and undeniable fight between right and wrong! I wish us all the strength. The nearest future of the word depends on **Armed Forces of Ukraine**. **Vovchik, Zhenia, Sasha**, stay safe, see you in the nearest feature! Slava Ukraine!

CURRICULUM VITæ

Serhii Volosheniuk

14-05-1995 Born in Sytkivtsi, Ukraine.

EDUCATION

2010–2013 **High School**
Ukrainian Physics and Mathematics Lyceum
Kyiv, Ukraine

2013–2017 **Bachelor of Science in Applied Mathematics and Physics**
Moscow Institute of Physics and Technology (MIPT)
Moscow, Russia
Thesis: Equipment development and sample preparation for investigation of topological transition in HgTe quantum well under uniaxial compression
Supervisor: Dr. A.Yu. Kuntsevich

2017–2019 **Master of Science in Applied Mathematics and Physics (cum laude)**
Joint degree:
Moscow Institute of Physics and Technology (MIPT)
Moscow, Russia
Skolkovo Institute of Science and Technology (Skoltech)
Moscow, Russia
Thesis: Structural and transport properties of Bi_2Se_3 thin films doped with Sr
Supervisors: Dr. A.Yu. Kuntsevich
Prof. Dr. M. Skvortsov

2019–2020 **Visiting researcher**
Karlsruhe Institute of Technology (KIT)
Karlsruhe, Germany

Project: Two-level-systems spectroscopy in Transmon qubits
Supervisors: Dr. J. Lisenfeld
Prof. Dr. A. G. Ustinov

2020-2024 **PhD. in Applied Physics**
Delft University of Technology
Delft, The Netherlands
Thesis: Thermoelectric effects in quantum systems
Promotors: Prof. Dr. Ir. H.S.J. van der Zant
Prof. Dr. P. Gehring

LIST OF PUBLICATIONS

12. **S. Volosheniuk**, R. Conte, A. Iwens, P. Gehring, and H. S. J. van der Zant. “Thermopower measurements in nanoscale devices with double lock-in technique”. In preparation [Chapter 4]

11. J. Ingla-Aynés, **S. Volosheniuk**, T. S. Ghiasi, A. Knothe, K. Watanabe, T. Taniguchi, V. I. Fal’ko, and H. S. J. van der Zant. “Kondo effect in a bilayer graphene gate-defined quantum point contact”. In preparation

10. **S. Volosheniuk**, R. Conte, T. Baum, S. Fernández, D. Peña, P. Gehring, and H. S. J. van der Zant. “A Moltronic heat engine”. In preparation, also Bulletin of the American Physical Society, (2024), [Chapter 6]

9. **S. Volosheniuk**, D. Bouwmeester, D. Vogel, C. Wegeberg, C. Hsu, M. Mayor, H. S. J. van der Zant, and P. Gehring. “Enhancing Thermoelectric Output in a Molecular Heat Engine Utilizing Yu-Shiba-Rusinov Bound States”. Under revision in *Nature Communications*, [Chapter 5]

8. A. Canetta, **S. Volosheniuk**, S. Satheesh, J. P. Alvarinhas Batista, A. Castellano, R. Conte, D. G. Chica, K. Watanabe, T. Taniguchi, X. Roy, H. S. J. van der Zant, M. Burghard, M. J. Verstraete, and P. Gehring. “Impact of Spin-Entropy on the Thermoelectric Properties of a 2D Magnet”. *Nano Letters* 24.22 (June 2024). [Chapter 7], pp. 6513–6520

7. J. Ingla-Aynés, A. L. R. Manesco, T. S. Ghiasi, **S. Volosheniuk**, K. Watanabe, T. Taniguchi, and H. S. J. van der Zant. “Specular Electron Focusing between Gate-Defined Quantum Point Contacts in Bilayer Graphene”. *Nano Letters* 23.12 (2023), pp. 5453–5459

6. **S. Volosheniuk**, D. Bouwmeester, C. Hsu, H. S. J. van der Zant, and P. Gehring. “Implementation of SNS thermometers into molecular devices for cryogenic thermoelectric experiments”. *Applied Physics Letters* 122.10 (Mar. 2023). [Chapter 3], p. 103501

5. A. Bilmes, **S. Volosheniuk**, A. V. Ustinov, and J. Lisenfeld. “Probing defect densities at the edges and inside Josephson junctions of superconducting qubits”. *npj Quantum Information* 8.1 (Mar. 2022), p. 24

4. A. Bilmes, A. K. Händel, **S. Volosheniuk**, A. V. Ustinov, and J. Lisenfeld. “In-situ bandaged Josephson junctions for superconducting quantum processors”. *Superconductor Science and Technology* 34.12 (Oct. 2021), p. 125011

3. A. Bilmes, **S. Volosheniuk**, J. D. Brehm, A. V. Ustinov, and J. Lisenfeld. “Quantum sensors for microscopic tunneling systems”. *npj Quantum Information* 7.1 (Feb. 2021), p. 27

2. A. B. Van'kov, B. D. Kaysin, **S. Volosheniuk**, and I. V. Kukushkin. "Exchange energy renormalization in quantum Hall ferromagnets with strong Coulomb interaction". *Phys. Rev. B* 100 (4 July 2019), p. 041407

1. **S. O. Volosheniuk**, Y. G. Selivanov, M. A. Bryzgalov, V. P. Martovitskii, and A. Y. Kuntsevich. "Effect of Sr doping on structure, morphology, and transport properties of Bi_2Se_3 epitaxial thin films". *Journal of Applied Physics* 125.9 (Mar. 2019), p. 095103